New features and enhancements in Community Land Model (CLM5) snow albedo modeling: description, sensitivity, and evaluation

Cenlin He[1], Mark Flanner[2], David M Lawrence[3], and Yu Gu[4]

[1]National Center for Atmospheric Research
[2]University of Michigan-Ann Arbor
[3]National Center for Atmospheric Research (UCAR)
[4]Joint Institute for Regional Earth System Science and Engineering

June 8, 2023

Abstract

We enhance the Community Land Model (CLM) snow albedo modeling by implementing several new features with more realistic and physical representations of snow-aerosol-radiation interactions. Specifically, we incorporate the following model enhancements: (1) updating ice and aerosol optical properties with more realistic and accurate datasets, (2) adding multiple dust types, (3) adding multiple surface downward solar spectra to account for different atmospheric conditions, (4) incorporating a more accurate adding-doubling radiative transfer solver, (5) adding nonspherical snow grain representation, (6) adding black carbon-snow and dust-snow internal mixing representations, and (7) adding a hyperspectral (480-band versus the default 5-band) modeling capability. These model features/enhancements are included as new CLM physics/namelist options, which allows for quantification of model sensitivity to snow albedo processes and for multi-physics model ensemble analyses for uncertainty assessment. The model updates will be included in the next CLM version release. Sensitivity analyses reveal stronger impacts of using the new adding-doubling solver, nonspherical snow grains, and aerosol-snow internal mixing than the other new features/enhancements. These enhanced snow albedo representations improve the CLM simulated global snowpack evolution and land surface conditions, with reduced biases in simulated snow surface albedo, snow cover, snow water equivalent, snow depth, and surface temperature, particularly over northern mid-latitude mountainous regions and polar regions.

New features and enhancements in Community Land Model (CLM5) snow albedo modeling: description, sensitivity, and evaluation

Cenlin He[1], Mark Flanner[2], David M. Lawrence[1], Yu Gu[3]

1. National Center for Atmospheric Research (NCAR), Boulder, CO, USA
2. University of Michigan Ann Arbor, MI, USA
3. University of California Los Angeles (UCLA), Los Angeles, CA, USA

Correspondence to: Cenlin He (cenlinhe@ucar.edu)

Key points

- We enhance CLM5 snow albedo modeling by including more realistic and physical representations of snow-aerosol-radiation interactions
- The new adding-doubling solver, nonspherical snow grains, and aerosol-snow internal mixing show stronger impacts than other new features
- The enhanced snow albedo representation improves the CLM simulated global snowpack evolution and land surface conditions

Abstract

We enhance the Community Land Model (CLM) snow albedo modeling by implementing several new features with more realistic and physical representations of snow-aerosol-radiation interactions. Specifically, we incorporate the following model enhancements: (1) updating ice and aerosol optical properties with more realistic and accurate datasets, (2) adding multiple dust types, (3) adding multiple surface downward solar spectra to account for different atmospheric conditions, (4) incorporating a more accurate adding-doubling radiative transfer solver, (5) adding nonspherical snow grain representation, (6) adding black carbon-snow and dust-snow internal mixing representations, and (7) adding a hyperspectral (480-band versus the default 5-band) modeling capability. These model features/enhancements are included as new CLM physics/namelist options, which allows for quantification of model sensitivity to snow albedo

processes and for multi-physics model ensemble analyses for uncertainty assessment. The model updates will be included in the next CLM version release. Sensitivity analyses reveal stronger impacts of using the new adding-doubling solver, nonspherical snow grains, and aerosol-snow internal mixing than the other new features/enhancements. These enhanced snow albedo representations improve the CLM simulated global snowpack evolution and land surface conditions, with reduced biases in simulated snow surface albedo, snow cover, snow water equivalent, snow depth, and surface temperature, particularly over northern mid-latitude mountainous regions and polar regions.

Plain Language Summary

Snow albedo plays a critical role in the Earth system, affecting land surface energy and water balance and related hydrological processes and also serving as an important land process that feeds back to the atmosphere. Several recent studies have identified new or improved physical representations of snow-aerosol-radiation interactions that show promise to improve snow albedo modeling. In this study, we leverage those recent advances in snow albedo modeling to implement a number of relevant new features into the widely-used Community Land Model (CLM), which is the land component of the Community Earth System Model (CESM). Specifically, we improve the ice and aerosol optical properties, the treatment of dust types and downward solar spectra, the albedo computation algorithm, the representation of snow grain shape and aerosol-snow mixing state, and the spectral calculation capability. These model updates will be included in the next CLM version release. Overall, the enhanced snow albedo representations improve the simulated global snowpack evolution and related land surface conditions.

1. Introduction

Snow albedo plays a key role in altering surface energy and water balance in the Earth system. It affects not only the evolution of snowpack states (e.g., snow depth, snow water equivalent (SWE), and snow cover) and hydrology (e.g., runoff/streamflow, reservoir storage, and flooding/drought) but also the atmosphere (e.g., surface temperature, humidity, local/regional boundary layer height, and clouds) through positive snow albedo feedback and land-atmosphere interactions (Bales et al., 2006; Painter et al., 2010; Flanner et al., 2011; Qian et al., 2015; Lee et

al., 2017; Skiles et al., 2018; Gleason et al., 2019; Yi et al., 2019; Dumont et al., 2020; Gul et al., 2021; Huang et al., 2022). Snow albedo represents an important source of uncertainty in regional and global weather, climate, and hydrological modeling (Essery et al. 2009; Chen et al., 2014; Oaida et al., 2015; Thackeray and Fletcher, 2016; Räisänen et al., 2017; He et al., 2019a, 2021). Snow albedo is affected by many factors, including snow grain size and shape, snow depth, snow density, snow microstructure, light-absorbing particles (LAPs) present in the snowpack, the solar zenith angle, and the downward solar spectrum (Wiscombe and Warren, 1980; Kokhanovsky and Zege, 2004; Flanner et al., 2007, 2021; He et al., 2014, 2017a; Liou et al. 2014; Dang et al., 2015; Gelman Constantin et al., 2020; He and Flanner, 2020; Picard et al., 2020; Dumont et al., 2021). Accurate simulation of snow albedo requires realistic characterization and physical representation of those key factors in land, weather, and climate models.

In the past decades, many empirical or semi-physical parameterizations have been developed to statistically link snow albedo with snowpack properties and environment conditions for application in weather and climate models (Verseghy, 1991; Yang et al., 1997; Roeckner et al., 2003; Gardner and Sharp, 2010; Vionnet et al., 2012; Abolafia-Rosenzweig et al., 2022), which however have their own limitations and uncertainties (He and Flanner, 2020). To achieve higher accuracy of snow albedo, several physics-based snowpack radiative transfer models have been developed, such as those based on the two-stream radiative transfer (Flanner et al., 2007; Libois et al., 2013; Tuzet et al. 2017), the Discrete-Ordinate-Method Radiative Transfer (DISORT) (Stamnes et al., 1988), the adding-doubling radiative transfer (Briegleb and Light, 2007; Dang et al., 2019), the Approximate Asymptotic Radiative Transfer (AART) Theory (Kokhanovsky and Zege, 2004; Libois et al., 2013), and the Monte Carlo Photon Tracing method (Kaempfer et al., 2007). Among them, the Snow, Ice, and Aerosol Radiative (SNICAR) model (Flanner et al, 2007, 2021) stands as one of the most widely used snowpack radiative transfer models, which has been implemented in several land and climate models including the Community Earth System Model (CESM)/Community Land Model (CLM; Lawrence et al., 2019) and the DOE's Energy Exascale Earth System Model (E3SM) Land Model (ELM; Golaz et al., 2019).

In previous snow radiative transfer models, it was a common practice to treat snow grains as spheres, externally mixed with LAPs such as black carbon (BC) and dust (Warren and Wiscombe, 1980; Flanner et al., 2007; Dang et al., 2015; Tuzet et al. 2017). However, in reality, snow grains are predominantly nonspherical, particularly for fresh snow (Erbe et al., 2003; Dominé

et al., 2003). Additionally, BC and dust can be mixed within snow grains (i.e., internal mixing) rather than the common assumption that BC and dust only exist outside snow grains (i.e., external mixing) (Flanner et al., 2012; He et al., 2019b). To accurately compute snow albedo with more realistic representations of snow grain shape and its interaction with LAPs, physics-based parameterizations have been developed that account for snow nonsphericity and snow-LAP internal mixing for applications in weather and climate models (e.g., Dang et al., 2016; Räisänen et al., 2017; He et al., 2017b, 2019b; Saito et al., 2019), revealing important impacts of these two factors (He, 2022). In addition, the size, shape, and composition of LAPs play a nontrivial role in snow-LAP-radiation interactions (Liou et al., 2014; He et al., 2018b, 2019b; Flanner et al., 2021; Pu et al., 2021; Shi et al. 2022). Moreover, in addition to the traditionally modeled LAPs, such as BC and dust, there is increasing attention on other types of LAPs including brown carbon (Yan et al., 2019; Liu et al., 2020; Li et al., 2021), snow algae (Cook et al., 2017; Williamson et al., 2020), and volcanic ash (Young et al., 2014; Flanner et al., 2014; Gelman Constantin et al., 2020).

The standalone version of SNICAR has been updated to include these more realistic and physical treatments of snow-LAP-radiation interactions (updated version is SNICAR-ADv3; Flanner et al., 2021), including updated ice and aerosol optics as well as downward solar spectra, incorporation of multiple dust types and nonspherical snow grains, and the use of a more accurate adding-doubling (AD) two-stream radiative transfer solver. The standalone SNICAR-ADv3 model does not include BC/dust-snow internal mixing but uses a coated BC particle treatment instead, which shows similar effects as with explicit BC-snow internal mixing (Flanner et al., 2021). Leveraging the SNICAR-ADv3 updates and other aforementioned new LAP-snow parameterizations, the E3SM/ELM model with SNICAR as its embedded snow albedo scheme has been updated to include snow nonsphericity, BC/dust-snow internal mixing, and the adding-doubling radiative transfer solver, which leads to improved simulations of snow surface energy and water balances (Hao et al., 2023).

In view of the scientific and modeling advances, it is imperative to enhance the CESM/CLM-SNICAR snow albedo modeling with more realistic and physical representations of snow-LAP-radiation interactions, considering the broad use of CESM/CLM (Lawrence et al., 2019). The default CLM uses the original SNICAR model developed 16 years ago (Flanner et al., 2007), which assumes spherical snow grains externally mixed with LAPs via a less accurate two-stream solver and outdated input databases for ice and aerosol optics and downward solar spectra.

These inadequate snow albedo treatments in CLM-SNICAR have been identified as a contributing factor to model biases in simulating surface albedo and snowpack evolution (e.g., Chen et al., 2014; Toure et al., 2018; Thackeray et al., 2019). Therefore, this study aims to improve the CLM-SNICAR snow albedo scheme by incorporating more realistic and physically-based representations of snow-LAP-radiation interactions.

This paper is organized as follows. Section 2 provides descriptions of model enhancements and simulations as well as observational datasets used for model evaluation. Section 3 investigates model sensitivities to each of the new features and enhancements implemented in this study. Section 4 presents evaluations of the updated model for key snow and surface fields. Section 5 concludes the study.

2. Model and data

2.1 CLM5 snow albedo scheme

We use the CLM version 5.0 (CLM5) in this study, which is the land component of CESM2. CLM5 represents a full suite of terrestrial biogeophysical and biogeochemical processes, including carbon and nitrogen cycles, vegetation dynamics for ecosystems, and land surface and subsurface energy and water processes. More details about CLM5 are provided in Lawrence et al. (2019). Since this study specifically focuses on snow albedo, we briefly summarize the key elements of the CLM5 snow albedo scheme below.

CLM5 includes the SNICAR model (Flanner et al., 2007) to compute snow albedo for the multi-layer (up to 12 layers) snowpack. It accounts for the effects of snow grain size (and hence snow aging) and LAP contamination on snow albedo. The original version of SNICAR leverages a multi-layer two-stream radiative transfer scheme based on Wiscombe and Warren (1980) and Toon et al. (1989). The required input variables for SNICAR include direct/diffuse radiation, surface downward solar spectrum, solar zenith angle (under direct radiation), ground albedo underlying snowpack, vertical distributions of snow grain size, snow layer thickness, snow density, and aerosol concentration, and optical properties of ice and aerosols. The ice and aerosol optical properties (single-scattering albedo, mass extinction cross-section, and asymmetry factor) are computed offline by Mie theory using particle refractive indices and size distributions, and are archived as look-up tables. The CLM5-SNICAR assumes snow spheres externally mixed with aerosols. The surface downward solar spectrum used in CLM5-SNICAR represents clear- or

cloudy-sky atmospheric conditions typical of mid-latitude winter. The CLM5-SNICAR computes snow albedo at 5 spectral bands (300-700 nm, 700-1000 nm, 1000-1200 nm, 1200-1500 nm, and 1500-5000 nm), which are then averaged to values at two broadbands (visible: 300-700 nm; near-infrared (NIR): 700-5000 nm) weighted by the downward solar spectrum. More detailed descriptions of CLM-SNICAR can be found in Flanner et al. (2007). Figure 1 summarizes the general workflow for the key elements in CLM5-SNICAR snow albedo calculations.

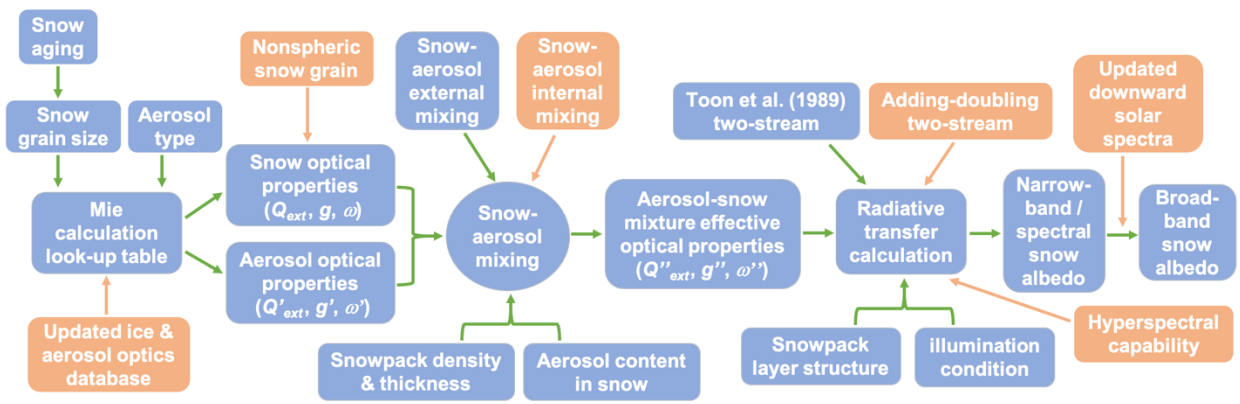

Figure 1. Workflow for key elements in CLM5-SNICAR snow albedo modeling. Blue boxes indicate the default model processes/capabilities. Orange boxes indicate the new model capabilities/enhancements implemented in this study. Q_{ext} is the mass extinction cross section, g is the asymmetry factor, and ω is the single-scattering albedo.

2.2 New features and enhancements in CLM5 snow albedo scheme

The standalone version of SNICAR has been recently updated to SNICAR-ADv3 by Flanner et al. (2021) with several new features as mentioned in Section 1. In addition, new parameterizations that account for BC-snow and dust-snow internal mixing have been recently developed. Thus, we combine all these recent updates that more physically and realistically represent snowpack characteristics in snow albedo computation, and implement them into CLM5-SNICAR (Table 1 and Figure 1). Particularly, we include these new features/enhancements as additional CLM5-SNICAR physics/namelist options, which offers an effective way to quantify model sensitivity to snow albedo processes and allows for relevant multi-physics model ensemble analyses for uncertainty evaluation.

Table 1. List of new features and enhancements in CLM-SNICAR snow albedo scheme implemented in this study

Features/enhancements	New schemes & namelist options (* for new baseline)	Original scheme
Ice optical properties: updates from Flanner et al. (2021), with multiple options for ice refractive indices	snicar_snw_optics = 1 (Warren, 1984) 2 (Warren and Brandt, 2008) 3* (Picard et al., 2016)	Warren (1984)
BC and OC optical properties: updates from Flanner et al. (2021)	Flanner et al. (2021)	Flanner et al. (2007)
Dust optical properties: updates from Flanner et al. (2021) with multiple dust types	snicar_dust_optics = 1* (Saharan dust) 2 (Colorado dust) 3 (Greenland dust)	Saharan dust (Flanner et al., 2007)
Downward solar spectra: updates from Flanner et al. (2021) for multiple atmospheric conditions	snicar_solarspec = 1* (mid-latitude winter) 2 (mid-latitude summer) 3 (sub-Arctic winter) 4 (sub-Arctic summer) 5 (Summit, Greenland) 6 (high mountain)	mid-latitude winter (Flanner et al., 2007)
Radiative transfer solver: new adding-doubling solver from Dang et al. (2019)	snicar_rt_solver = 1 (Toon et al. 1989) 2* (Adding-Doubling)	Toon et al. (1989)
Snow grain shape: nonspherical snow grains from He et al. (2017b)	snicar_snw_shape = 1 (sphere) 2 (spheroid) 3* (hexagonal) 4 (snowflake)	sphere
BC-snow mixing: internal mixing from He et al. (2017b)	snicar_snobc_intmix = true (internal mixing) false* (external mixing)	external mixing
Dust-snow mixing: internal mixing from He et al. (2019b)	snicar_snodst_intmix = true (internal mixing) false* (external mixing)	external mixing
Wavelength band: new hyperspectral (480-band, 10-nm spectral resolution) capability from Flanner et al. (2021)	snicar_numrad_snw = 5* (5-band) 480 (480-band)	5-band
New namelist controls for aerosol & OC	snicar_use_aerosol = true*, false DO_SNO_OC = true, false*	No namelist controls on using aerosol and OC (hard-coded)

2.2.1 Updated ice optical properties

The original CLM5-SNICAR uses the Warren (1984) compilation of ice refractive indices (RI) across the solar spectrum. Later, Warren and Brandt (2008) further updated the ice refractive indices data with much weaker absorption at wavelengths below 600 nm. However, more recent measurements by Picard et al. (2016) showed a larger ice absorption (i.e., the imaginary part of refractive indices) at 320-600 nm wavelengths than the Warren and Brandt (2008) data but smaller than the Warren (1984) data. This is consistent with the systematic snow albedo overestimate at wavelengths below 500 nm in SNICAR simulations using the Warren and Brandt (2008) data (He et al., 2018c). Thus, Flanner et al. (2021) updated the imaginary part of ice refractive indices by replacing the Warren and Brandt (2008) data with the Picard et al. (2016) data at wavelengths shorter than 600 nm. Flanner et al. (2021) also compiled another dataset for the imaginary part of ice refractive indices by merging the Warren (1984) and Perovich and Govoni (1991) datasets. These three datasets use the same Warren and Brandt (2008) compilation of the real part of refractive indices, and only differ in the imaginary part at wavelengths less than 600 nm, which is extremely challenging to measure accurately. Including all these three datasets in CLM5-SNICAR (i.e., ice optics namelist option "snicar_snw_optics" in Table 1) will allow uncertainty quantification. Following Flanner et al. (2021), we use the merged Picard et al. (2016) dataset as the new baseline model option in the updated CLM5-SNICAR.

Using the ice refractive indices, ice optical properties (i.e., single-scattering albedo, mass extinction cross-section, and asymmetry factor) are then computed by Mie theory based on various ice grain effective radii ranging from 30 to 1500 μm with lognormal size distributions (Flanner et al., 2021), and are archived as an input look-up table. The look-up table of ice optical properties created by Flanner et al. (2021) is for 480-band at 10-nm spectral (i.e., hyperspectral) resolution across the solar spectrum (200-5000 nm). To work with the 5 spectral bands in CLM5-SNICAR, we further use the spectral weighted averaging technique to convert the hyperspectral ice optical properties to the 5-band values following Flanner et al. (2007). For the new hyperspectral computation option added to CLM5-SNICAR (see Section 2.2.9), we directly use the 480-band ice optics dataset produced by Flanner et al. (2021).

2.2.2 Updated aerosol optical properties

The original CLM5-SNICAR accounts for three types of LAPs, including BC, OC (i.e., brown carbon), and dust (Saharan type), using the aerosol optics dataset developed by Flanner et al. (2007). Flanner et al. (2021) updated the optical properties for all three aerosol types using updated particle density, size distribution, and refractive indices via Mie theory calculations. Overall, the updated aerosol optical properties lead to a stronger light absorption for OC and Saharan dust but a weaker light absorption for BC. We implement the Flanner et al. (2021) dataset into CLM5-SNICAR and conduct the spectral weighted averaging to convert the hyperspectral (480-band) aerosol optical properties to the 5-band values following Flanner et al. (2007). For the new hyperspectral computation option (see Section 2.2.9), we directly use the 480-band aerosol optics dataset (Flanner et al., 2021). Given the substantial uncertainty in OC modeling due to a lack of observational constraints (Liu et al., 2020), we turn off the OC effect on snow albedo (namelist option "DO_SNO_OC" in Table 1) in our proposed new baseline model configuration, but we activate it in sensitivity simulations to test its impact (Section 3).

2.2.3 Updated dust types

The original CLM5-SNICAR only accounts for one dust type (i.e., Saharan dust; Flanner et al., 2007), while previous studies showed substantial differences in dust optical properties due to different particle size and composition for dust that originates from different regions (Scanza et al., 2015; Polashenski et al., 2015; Skiles et al., 2017). Thus, in addition to the Saharan dust (Scanza et al., 2015), Flanner et al. (2021) included two more dust types, Colorado dust (Skiles et al., 2017) and Greenland dust (Polashenski et al., 2015), which are added to the updated CLM5-SNICAR in this study. Overall, Greenland dust shows the strongest light absorbing ability, followed by Saharan dust, while Colorado dust has the weakest light absorbing capacity among the three (Flanner et al., 2021). Including different dust types in CLM5-SNICAR (i.e., dust optics namelist option "snicar_dust_optics" in Table 1) offers a way for uncertainty analysis. Following Flanner et al. (2021), we use the Saharan dust as the new baseline model option in the updated CLM5-SNICAR. We note that the updated model does not have the capability of simultaneously using multiple dust types over different regions in one single simulation. Ideally, the CLM5-SNICAR should be able to take the spatiotemporally varying aerosol optical properties (dust, BC, and OC) directly from the coupled atmospheric model component for consistent simulations, which will be improved in the future.

2.2.4 Updated surface downward solar spectra

The original CLM5-SNICAR uses the surface downward solar spectrum for clear-sky or cloudy-sky atmospheric conditions typical of mid-latitude winter (Flanner et al., 2007). In the model, the downward solar spectrum is used uniformly across the simulation domain to compute the spectrally-integrated broadband snow albedo from the spectral albedo derived from the radiative transfer solver. However, atmospheric conditions significantly affect the downward solar spectrum at the surface and therefore using only one downward solar spectrum may lead to nontrivial errors in simulated broadband snow albedo. Thus, Flanner et al. (2021) developed 5 additional downward solar spectra to represent clear-sky and cloudy-sky atmospheric conditions typical of mid-latitude summer, sub-Arctic winter, sub-Arctic summer, Summit Greenland, and high mountain environments. We implement these new downward solar spectra (i.e., solar spectrum namelist option "snicar_solarspec" in Table 1) into CLM5-SNICAR to offer more accurate albedo calculations for applications in those specific regions. Following Flanner et al. (2021), we use the mid-latitude winter spectrum as the new baseline model option in the updated CLM5-SNICAR. We note that the updated model does not have the capability of simultaneously using multiple solar spectra over different regions in one single simulation. Ideally, the CLM5-SNICAR should be able to take the spatiotemporally varying downward solar spectrum directly from the coupled atmospheric model component for consistent simulations. This is an important opportunity for further future improvement.

2.2.5 Updated radiative transfer solver

The original CLM5-SNICAR adopts the tri-diagonal matrix two-stream solver (Toon et al., 1989), which shows larger snow albedo biases (i.e., overestimates) particularly under diffuse conditions than an adding-doubling two-stream solution (Dang et al., 2019). Moreover, the adding-doubling solution has a stronger computational stability under different solar zenith angles and a higher computational efficiency than the tri-diagonal matrix solution. The adding-doubling solver also allows accounting for internal Fresnel layers in snow-ice interface, providing the potential for a unified snow-ice radiative transfer treatment. Because of these advantages, the adding-doubling solution has been implemented in the standalone SNICAR-ADv3 (Flanner et al., 2021) and the E3SM/ELM model (Hao et al., 2023). Following these recent studies, we implement the adding-

doubling solution into CLM5-SNICAR (i.e., radiative transfer namelist option "snicar_rt_solver" in Table 1), and use it as the new baseline model option in the updated CLM5-SNICAR, considering its higher computational accuracy, efficiency, and stability. Detailed descriptions of the adding-doubling formulation can be found in Dang et al. (2019).

2.2.6 Representation of snow nonsphericity

The original CLM5-SNICAR assumes spherical snow grains (Flanner et al., 2007), which however may not be a realistic representation since nonspherical snow grains are ubiquitous in reality (Erbe et al., 2003; Dominé et al., 2003). To quantify the impact of snow nonsphericity, He et al. (2017b) developed a set of snow optical parameterizations based on sophisticated geometric-optics ray-tracing calculations (Liou et al., 2014) for four typical snow grain shapes representative of real-world observations, including sphere, spheroid, hexagonal plate/column, and fractal snowflake (Figure 2). Snow grain shape mainly affects the snow asymmetry factor with very limited impact on extinction cross section and single-scattering albedo (Dang et al., 2016; He and Flanner, 2020). Thus, the He et al. (2017b) parameterizations make corrections to the asymmetry factor of snow spheres to account for nonsphericity effects based on grain shape, aspect ratio, effective radius, and wavelength. The parameterizations have been implemented into the standalone SNICAR-ADv3 (Flanner et al., 2021) and the E3SM/ELM model (Hao et al., 2023), which provide detailed descriptions of the associated formulation and implementation. Following these recent studies, we implement the same parameterizations for the four grain shapes into CLM5-SNICAR (i.e., snow shape namelist option "snicar_snw_shape" in Table 1). We set the hexagonal shape (one of the most common shapes for ice crystal) as the new baseline model option in the updated CLM5-SNICAR following Flanner et al. (2021).

We note that there are other parameterizations that account for nonspherical snow grains in albedo calculations, which have been used in other land/climate models (e.g., Libois et al., 2013; Räisänen et al., 2017; Saito et al., 2019). These studies all find that accounting for snow nonsphericity provides a more realistic representation of snow characteristics in albedo calculations. All of these models are limited by a lack of dynamic evolution of snow grain shapes, which is another opportunity for future model development. We note that in this study, the snow aging scheme that simulates the dynamic evolution of specific surface area (Flanner et al., 2007)

is the same as that in the default CLM-SNICAR. Thus, the snow nonsphericity effect analyzed here quantifies the impact of different grain shapes with equal specific surface area.

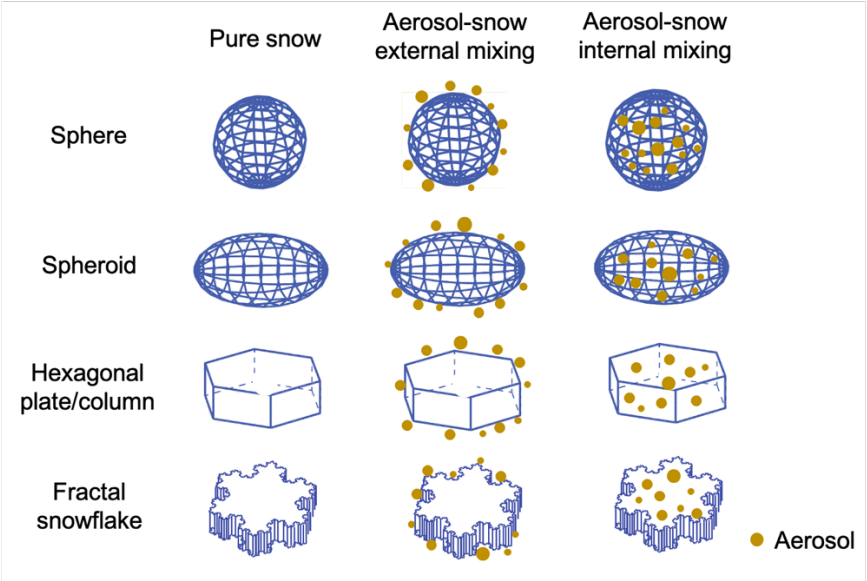

Figure 2. Demonstration of snow grains with four different shapes as well as aerosol-snow external and internal mixing states that are implemented in this study.

2.2.7 Representation of BC-snow internal mixing

The original CLM5-SNICAR assumes BC-snow external mixing, whereas previous studies pointed out that BC can also be internally mixed with snow grains (Figure 2), through a number of BC-cloud-precipitation interaction processes, which strongly enhances BC-induced snow albedo reduction (Flanner et al., 2012; Liou et al., 2014; He et al., 2017b). He et al. (2017b) developed a parameterization to account for BC-snow internal mixing in snow albedo calculations, where the internal mixing mainly affects the single-scattering albedo of BC-snow mixtures with negligible impacts on snow asymmetry factor and extinction cross section. This parameterization was developed based on sophisticated geometric-optics ray-tracing calculations and computes the change of snow single-scattering albedo caused by BC-snow internal mixing as a function of BC particle effective radius and concentration in snow. This parameterization was implemented into an earlier version of SNICARv2 (He et al., 2018c), which describes the formulation and implementation in detail. Following this study, we implement the BC-snow internal mixing parameterization into CLM5-SNICAR (i.e., BC-snow mixing namelist option

"snicar_snobc_intmix" in Table 1). We note that there is a lack of observational constraints for BC-snow mixing state (internal versus external) and there is also substantial uncertainty in modeling the evolution of BC-snow mixing state, therefore we maintain the BC-snow external mixing as the new baseline model option in the updated CLM5-SNICAR, but we activate the internal mixing in sensitivity simulations to test its impact (Section 3).

There are other methods developed to account for the effect of BC-snow internal mixing, such as the look-up table method developed based on a dynamic effective medium approximation in Flanner et al. (2012), which has been adopted by E3SM/ELM-SNICAR (Hao et al., 2023). He et al. (2018c) showed that the He et al. (2017b) parameterization of BC-snow internal mixing leads to consistent snow albedo reductions with the results computed from the Flanner et al. (2012) look-up tables. More observations of BC-snow mixing state are needed to constrain models to achieve more accurate estimates of BC-induced snow albedo changes.

2.2.8 Representation of dust-snow internal mixing

Similar to the BC-snow mixing treatment, the original CLM5-SNICAR assumes dust-snow external mixing. However, previous studies found that dust can also be mixed internally with snow grains (Figure 2) via dust-cloud-precipitation interactions, which enhances dust-induced snow albedo reduction (He et al., 2019b; Shi et al., 2021). To quantify the impact of dust-snow internal mixing, He et al. (2019b) developed a parameterization that nonlinearly connects internal mixing-induced changes of snow single-scattering albedo to dust concentration in snow based on sophisticated geometric-optics ray-tracing calculations. The dust-snow internal mixing has negligible effects on the snow asymmetry factor and extinction cross section. The He et al. (2019b) parameterization was implemented into E3SM/ELM-SNICAR (Hao et al., 2023). In the present study, we implement the dust-snow internal mixing parameterization into CLM5-SNICAR (i.e., dust-snow mixing namelist option "snicar_snodst_intmix" in Table 1). Similar to BC-snow mixing, there is also a lack of observational constraints for dust-snow mixing state and large model uncertainty for the mixing state evolution. Thus, we maintain the dust-snow external mixing as the new baseline model option in the updated CLM5-SNICAR, but we activate the internal mixing in sensitivity simulations to test its impact (Section 3). We note that the He et al. (2019b) parameterization of dust-snow internal mixing was developed without the presence of internally

mixed BC, so we suggest not activating BC-snow and dust-snow internal mixing simultaneously in CLM5-SNICAR.

Recently, Shi et al. (2021) used another method (i.e., the effective medium approximation) to account for dust-snow internal mixing in snow albedo modeling, which shows generally consistent results with those derived from the He et al. (2019b) parameterization. In the future, more observations of dust-snow mixing state are needed to better constrain modeled dust impacts on snow albedo.

2.2.9 New hyperspectral computation capability

The original CLM5-SNICAR uses 5 spectral bands (300-700 nm, 700-1000 nm, 1000-1200 nm, 1200-1500 nm, and 1500-5000 nm) in radiative transfer calculations to increase computational efficiency. Accordingly, the ice and aerosol optical properties and downward solar spectra in input datasets are all spectrally averaged into the 5 bands. However, a recent study (Wang et al., 2022) found that because of the nonlinearity of radiative transfer computation, using the 5 spectral bands in SNICAR leads to a nontrivial snow albedo bias (up to 0.05) compared to hyperspectral (10-nm spectral resolution) calculations. Thus, we implement a hyperspectral (10-nm spectral resolution with 480 bands) computation capability into CLM5-SNICAR in this study, similar to that used by the standalone SNICAR-ADv3 model. The hyperspectral modeling capability includes all the new features and enhancements mentioned in Sections 2.2.1-2.2.8. The addition of this hyperspectral capability particularly targets on local/regional process-level investigations that require higher snow albedo accuracy, because it is much more computationally expensive than the 5-band calculations (e.g., 8 times slower for global 1-deg 10-year simulations in this study using the configuration described in Section 2.3). However, as computational power increases, the use of this hyperspectral capability in global or high-resolution modeling will become more feasible.

2.3 Model simulations

To assess the model sensitivities and performance with the aforementioned new features and enhancements, we conduct a series of global 1-deg land-only CLM5-SNICAR simulations driven by the atmospheric forcing from the 3-hourly 0.5° Global Soil Wetness Project Phase 3 dataset (GSWP3; Dirmeyer et al., 2006), which has been widely used and evaluated by previous studies (e.g., Lawrence et al., 2019; Hao et al., 2023). All model simulations use the prescribed

monthly climatological MODIS satellite phenology mode (i.e., CLM configuration/compset: I2000Clm51Sp) (Lawrence et al., 2019), and the prescribed monthly aerosol (BC, dust, OC) wet and dry deposition flux from the CESM2-WACCM simulations participated in CMIP6 experiments (Danabasoglu et al., 2020).

Model experiments include a default baseline simulation using the original CLM5-SNICAR (hereinafter "default baseline"), a new baseline simulation using the enhanced CLM5-SNICAR (hereinafter "new baseline") with the new baseline physics option identified above and in Table 1, and a set of twin sensitivity simulations by turning on and off each new feature/enhancement (Table 1) at a time with the same baseline setup for other snow physics options in order to quantify the impact of the targeted feature/enhancement. The aerosol-induced snow albedo radiative forcing analyzed in this study is based on the instantaneous ground net radiative flux difference through double calls of SNICAR with and without specific aerosol species. We spin up the model simulations for the years 2000-2005 and use the 2006-2010 period for analysis. For seasonal analysis, we define each season as winter (December-January-February), spring (March-April-May), summer (June-July-August), and fall (September-October-November).

2.4 Data for model evaluation

To evaluate the default and new baseline model simulations of snow albedo and other snowpack properties, global spatiotemporally continuous observation-based datasets are preferred. Thus, we use the daily 0.05° MODIS data for snow cover fraction (MOD10C1 and MYD10C1) and surface albedo (MCD43C3) as well as the monthly 0.1° ERA-5 land reanalysis data for snow water equivalent (SWE), snow depth, and surface 2-m temperature. The MODIS MCD43C3 product is an Aqua-Terra merged surface albedo dataset and we use the data with quality flag of 0-2 (i.e., "ok", "good", and "best") to achieve a balance between enough samples and data quality, following He et al. (2019a). We use the MODIS snow cover data with quality flag of 0 and 1 (i.e., "good" and "best") and cloud fraction of <20% (more clouds lead to degraded data accuracy) to achieve a balance between enough samples and data quality, following He et al. (2019a). We further merge the Aqua (MYD10C1) and Terra (MOD10C1) MODIS snow cover data to obtain more complete global maps by replacing the data gaps in MOD10C1 with valid values (if existing) from MYD10C1 or averaging the pixel values if both MOD10C1 and MYD10C1 have valid data. To compare with model simulations at consistent spatial grids, we re-map the MODIS and ERA-

5 data to the model grids by averaging the values across the MODIS 0.05° pixels and ERA-5 0.1° pixels that are within each of the model 1° grids, respectively.

3. Model sensitivities to new features/enhancements

3.1 Effects of updated ice optics

Figure 3 shows the all-sky annual mean effects of updated ice optical properties on global snow albedo by using the Picard et al. (2016) versus Warren and Brandt (2008) ice refractive indices. Because the two datasets mainly differ at the visible band, there are negligible impacts on the NIR albedo. For the visible snow albedo, the differences are also small (<0.003) with slightly lower albedo using the Picard et al. (2016) data mainly over two polar regions under diffuse radiation (Figures 3 and S1). This is because the Picard et al. (2016) data leads to a stronger visible ice absorption (Flanner et al., 2021). Although the impact of using the Picard et al. (2016) data is small, it appears to more accurately capture the ice absorption in the visible band (He et al., 2018c; Flanner et al., 2021) and hence is recommended to use in future studies.

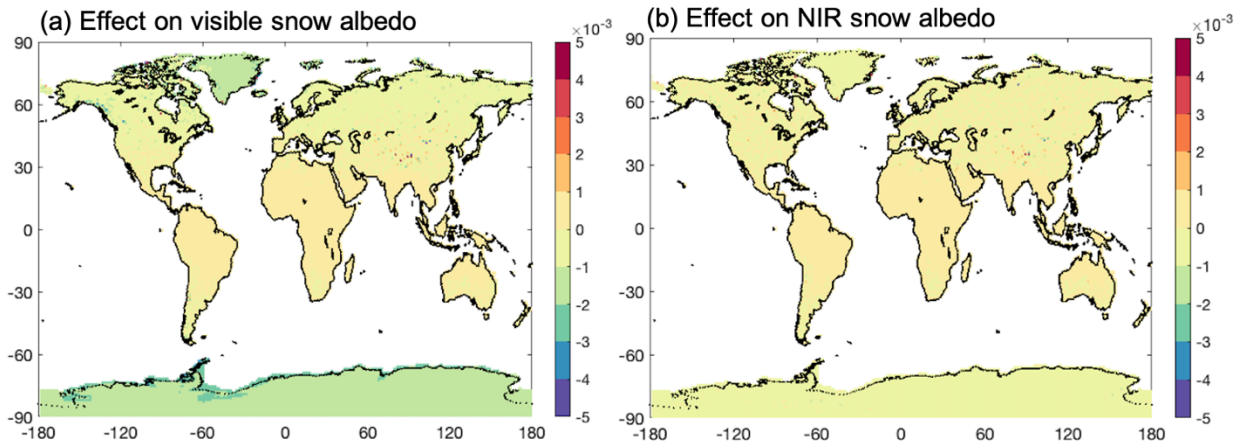

Figure 3. 5-year (2006-2010) all-sky annual mean effects of updated ice optical properties (i.e., differences between simulations using the Picard et al. (2016) and Warren and Brandt (2008) ice refractive indices): (a) difference for visible snow albedo, (b) difference for NIR snow albedo.

3.2 Effects of updated aerosol optics

Figure 4 shows the all-sky annual mean effects of updated aerosol (BC, OC, and Saharan dust) optical properties from the Flanner et al. (2021) data versus the Flanner et al. (2007) data on

snow-covered ground albedo and corresponding aerosol-induced snow albedo radiative forcing. Compared to using the Flanner et al. (2007) aerosol optics, the total aerosol-induced snow-covered ground albedo reduction using the Flanner et al. (2021) data is enhanced by up to 0.02 mainly over northern mid-latitudes (Figure 4a). This is primarily driven by stronger dust and OC light absorption using the Flanner et al. (2021) data relative to the Flanner et al. (2007) data, which further leads to stronger induced snow albedo forcing (Figures 4c, d) by up to >2.0 W m^{-2} (dust and OC combined) over heavily polluted hotspots, by ~0.17 W m^{-2} averaged over Northern Hemisphere, and by ~0.09 W m^{-2} globally. We note that the largely enhanced OC albedo forcing is due to the use of relatively strong-absorbing brown carbon optics in Flanner et al. (2021), which may not be representative of all OC or brown carbon. The enhanced snow albedo forcing caused by dust and OC is partially offset by the weaker BC light absorption with the BC forcing reduced by about 0.03 W m^{-2} averaged over Northern Hemisphere and 0.01 W m^{-2} globally (Figure 4b). The differences caused by updated aerosol optics mainly occur over northern mid-latitudes during winter and spring, and northern high-latitudes during spring and summer (Figure S2).

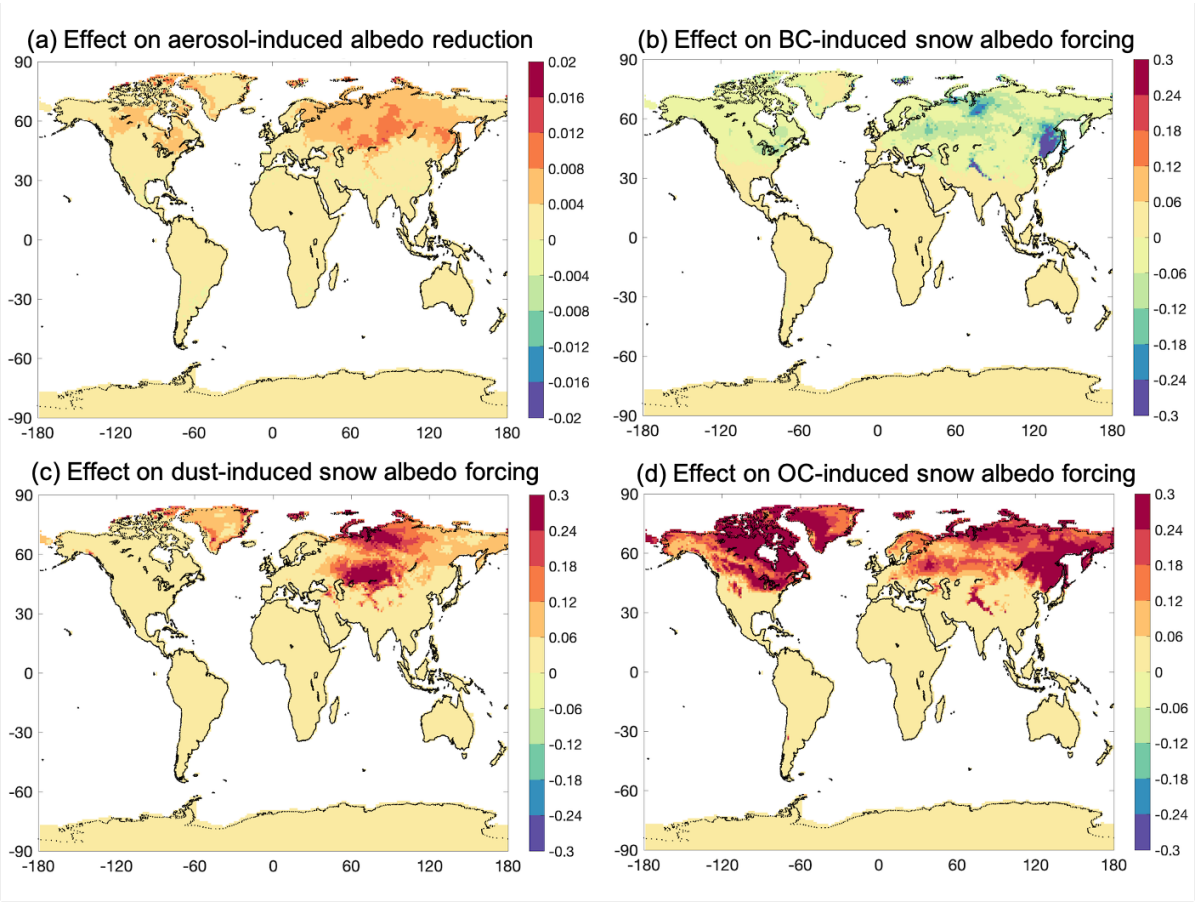

Figure 4. 5-year (2006-2010) all-sky annual mean effects of updated aerosol optical properties (i.e., differences between simulations using the Flanner et al. (2021) and Flanner et al. (2007) data): (a) difference for snow-covered ground albedo reduction caused by all aerosols, (b) difference for BC-induced snow albedo forcing (W m^{-2}), (c) difference for dust-induced snow albedo forcing (W m^{-2}), (d) difference for OC-induced snow albedo forcing (W m^{-2}).

3.3 Effects of different dust types

Figure 5 shows the all-sky annual mean differences between simulations using Greenland dust and Colorado dust in snow-covered ground albedo reduction and snow albedo forcing caused by dust. These two types of dust show the largest difference in light absorption capabilities among all the three dust types in the model (Section 2.2.3), which demonstrates the upper limit of model sensitivity to dust types in CLM5. Overall, using Greenland dust shows stronger albedo reduction by up to 0.02 mainly over northern Eurasia during winter and spring (Figures 5a and S3), compared to using Colorado dust. The corresponding annual difference in dust-induced snow albedo forcing reaches more than 3 W m^{-2} over polluted hotspots, with ~0.1 W m^{-2} averaged over Northern Hemisphere and ~0.05 W m^{-2} globally. Seasonally, the differences in snow albedo forcing mainly locate in northern mid-latitudes during winter and spring, and northern high-latitudes during spring and summer (Figure S5).

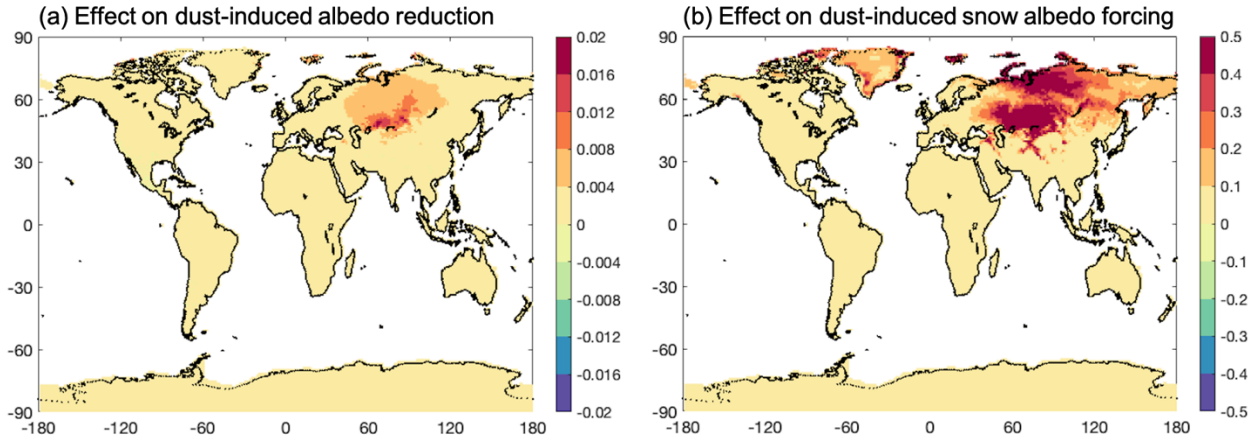

Figure 5. 5-year (2006-2010) all-sky annual mean effects of different dust types (i.e., differences between simulations using Greenland dust and Colorado dust): (a) difference for snow-covered

ground albedo reduction caused by dust, (b) difference for dust-induced snow albedo forcing (W m^{-2}).

3.4 Effects of updated downward solar spectra

Figure 6 shows the 5-year annual mean effects of downward solar spectra on snow albedo by using the high mountain spectrum versus the mid-latitude summer spectrum. These two spectra have the largest difference in energy distribution in the CLM5 spectral bands particularly for direct radiation (Figure S5), which demonstrates the upper limit of model sensitivity to downward solar spectra. Specifically, the snow albedo difference (by up to -0.04) between using the two spectra primarily occurs in the NIR band under direct radiation (Figure 5c), particularly over high latitudes with a mean difference of -0.02. The impact is minimal in the visible band or diffuse NIR band (Figures 5a, b, d).

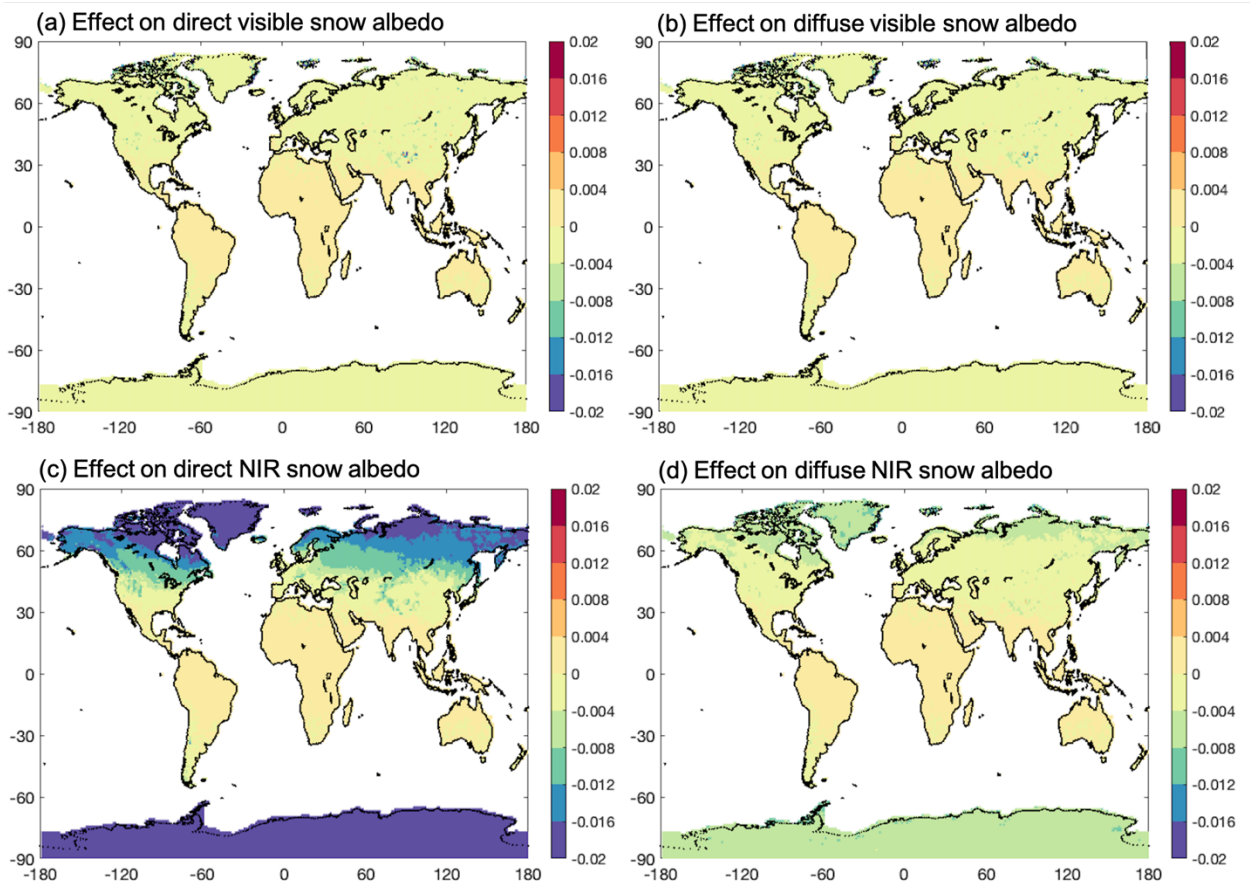

Figure 6. 5-year (2006-2010) annual mean effects of different downward solar spectra (i.e., differences between simulations using high mountain and mid-latitude summer spectra): (a)

difference for direct-beam visible snow albedo, (b) difference for diffuse visible snow albedo, (c) difference for direct-beam NIR snow albedo, (d) difference for diffuse NIR snow albedo.

3.5 Effects of updated radiative transfer solver

Figure 7 shows the 5-year annual mean snow albedo difference between simulations using the adding-doubling and Toon et al. (1989) radiative transfer solvers. The differences are negligible for the visible band but are significant (up to 0.04) for the NIR band under both direct and diffuse radiation. Specifically, using the adding-doubling solver leads to higher snow albedo under NIR direct radiation particularly in high-latitudes with a mean difference of 0.02 (Figure 7c), whereas it leads to a lower snow albedo under NIR diffuse radiation particularly in high-latitudes with a mean difference of -0.02 (Figure 7d). These difference patterns are similar across all the seasons with relatively larger differences in winter and spring (Figure S6). These results are consistent with the findings of Dang et al. (2019), where the adding-doubling solver has a similarly high accuracy as the Toon et al. (1989) solver for the visible band but substantially reduces the albedo underestimates at solar zenith angle >75° under NIR direct radiation and the albedo overestimates under NIR diffuse radiation caused by the Toon et al. (1989) solver. Thus, using the adding-doubling solver results in higher accuracy in snow albedo calculations.

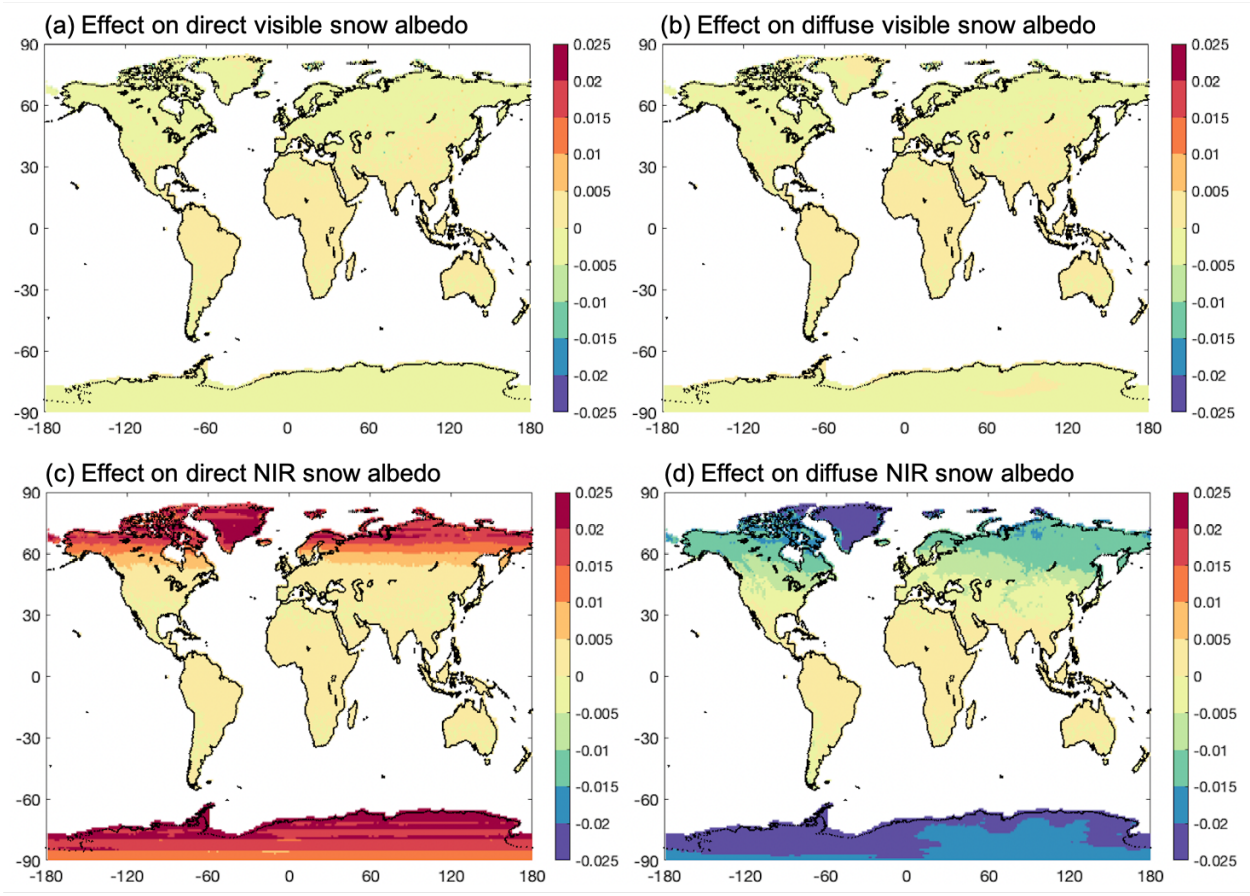

Figure 7. 5-year (2006-2010) annual mean effects of updated snow radiative transfer solvers (i.e., differences between simulations using the adding-doubling and Toon et al. (1989) solvers): (a) difference for direct-beam visible snow albedo, (b) difference for diffuse visible snow albedo, (c) difference for direct-beam NIR snow albedo, (d) difference for diffuse NIR snow albedo.

3.6 Effects of nonspherical snow grains

Figure 8 shows the 5-year all-sky annual mean effects of nonspherical snow grains on snow albedo and aerosol-induced snow albedo forcing by using fractal snowflakes versus snow spheres. These two grain shapes have the largest difference in snow optical properties, which demonstrates the upper limit of model sensitivity to snow nonsphericity in CLM5. Compared to using snow spheres, using fractal snowflakes leads to substantially higher snow albedo by more than 0.05 over some hotspots and ~0.015 globally, with a stronger impact over high-latitudes (Figure 8a). Seasonally, the albedo increase due to the use of fractal snowflakes are strongest in winter and spring over northern mid-latitudes and two polar regions (Figure S7). This is consistent with the conclusions from previous studies (Dang et al., 2016; Räisänen et al. 2017; He et al., 2018a), where

nonspherical snow grains have lower asymmetry factor (i.e., weaker forward scattering) and hence higher snow albedo by 0.02-0.05 on average, depending on specific grain shape, grain size, and snow density and thickness.

In addition, previous studies (He et al., 2018a, 2019; Shi et al., 2022) also found that nonspherical snow grains can reduce aerosol-induced snow albedo forcing because of the reduced forward scattering and hence less aerosol absorption throughout the snowpack column. This is confirmed by the results in this study, where using fractal snowflakes shows lower snow albedo forcing for BC, dust, and OC by up to 0.3 W m^{-2} or more, compared to using snow spheres (Figures 8b-d).

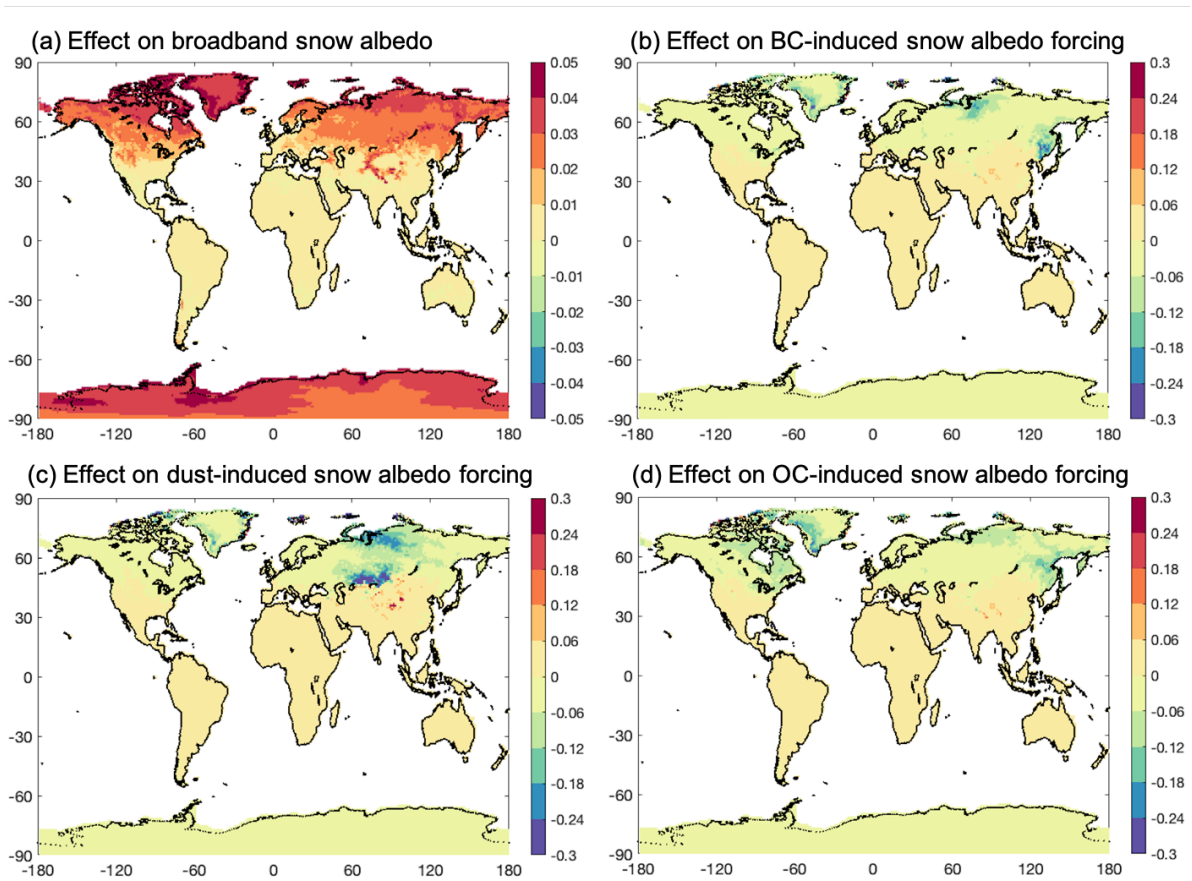

Figure 8. 5-year (2006-2010) all-sky annual mean effects of nonspherical snow grain (i.e., differences between simulations using fractal snowflake and snow sphere): (a) difference for broadband snow albedo, (b) difference for BC-induced snow albedo forcing (W m^{-2}), (c) difference for dust-induced snow albedo forcing (W m^{-2}), (d) difference for OC-induced snow albedo forcing (W m^{-2}).

3.7 Effects of BC-snow internal mixing

Figures 9a-b show the 5-year all-sky annual mean effects of BC-snow internal mixing on BC-induced snow albedo reduction and albedo forcing, compared to external mixing. Overall, the internal mixing significantly enhances BC-induced snow albedo reduction by up to 0.042 and albedo forcing by up to 1.0 W m^{-2} or more, with main effects over northern mid- and high-latitudes during winter and spring (Figure S8). This is consistent with previous studies (Flanner et al., 2012; He, 2022), where the snow albedo reduction caused by internal mixing can be enhanced by up to 0.05 or more relative to external mixing, depending on snow grain size and shape, snowpack density and thickness, BC concentration in snow, and illumination conditions. He et al. (2018a) further found that the enhanced albedo reduction due to internal mixing increases the BC-induced snow albedo forcing by up to 1 W m^{-2} in polluted regions like northern China snowpack, which agrees with the results in this study (Figure 9b).

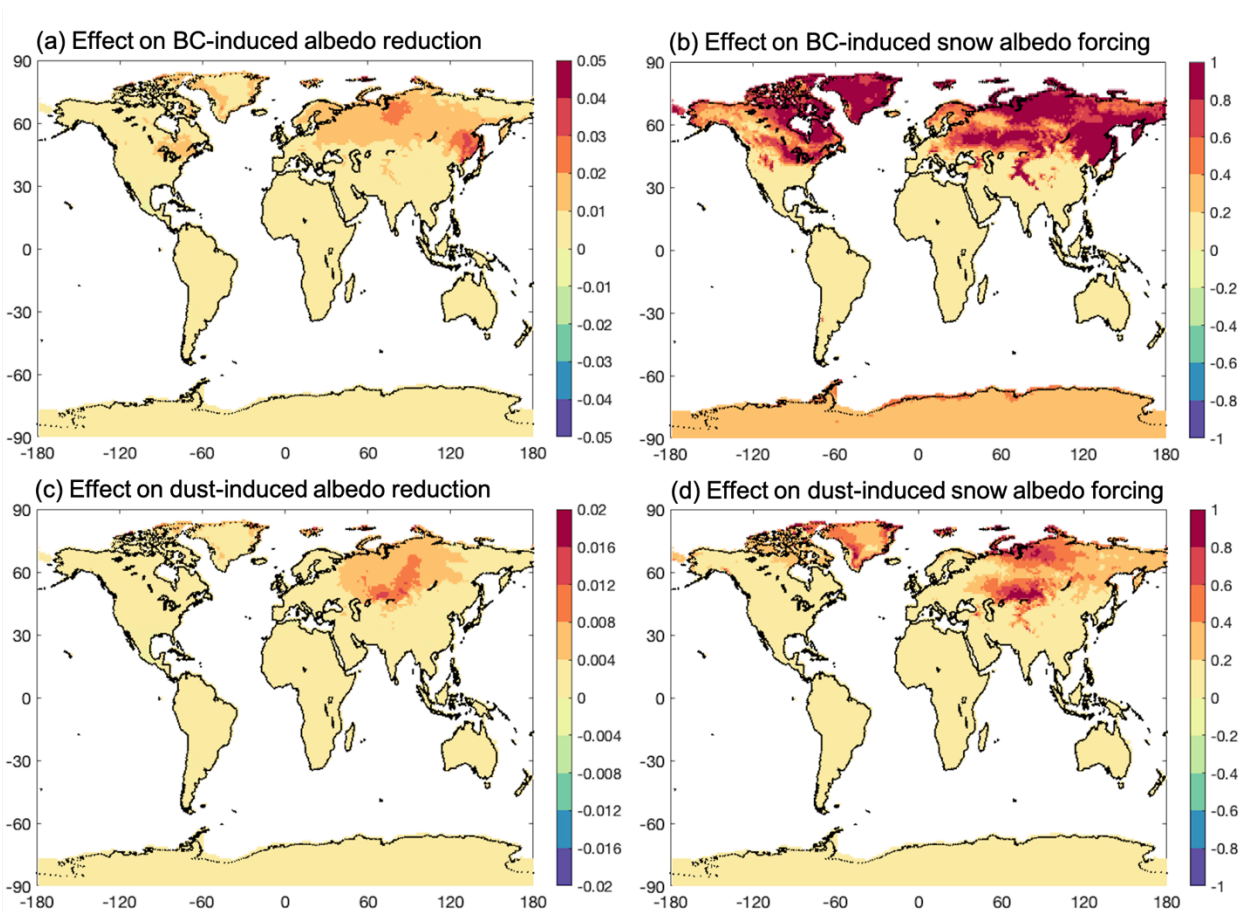

Figure 9. 5-year (2006-2010) all-sky annual mean effects of aerosol-snow internal mixing (i.e., differences between simulations using internal mixing and external mixing): (a) BC-snow internal mixing impact on BC-induced snow-covered ground albedo reduction, (b) BC-snow internal mixing impact on BC-induced snow albedo forcing (W m^{-2}), (c) dust-snow internal mixing impact on dust-induced snow-covered ground albedo reduction, (b) dust-snow internal mixing impact on dust-induced snow albedo forcing (W m^{-2}).

3.8 Effects of dust-snow internal mixing

Figures 9c-d show the 5-year all-sky annual mean effects of dust-snow internal mixing on dust-induced snow albedo reduction and albedo forcing, compared to external mixing. Similar to BC-snow internal mixing, the dust-snow internal mixing enhances snow albedo reduction by up to 0.02 and albedo forcing by up to 1.0 W m^{-2} or more, with major impacts over northern Eurasia during winter and spring as well as in the coasts of Greenland during summer (Figures 9c-d and S9). This is consistent with previous findings (He et al., 2019b; Shi et al., 2021, 2022), where dust-snow internal mixing can result in 10-45% enhancement in dust-induced snow albedo reduction and albedo forcing relative to external mixing, depending on snow grain size and shape, snowpack density and thickness, dust content in snow, and illumination conditions.

3.9 Effects of new hyperspectral capability

Figure 10 shows the 5-year annual mean difference in snow albedo between simulations using hyperspectral (480-band) and 5-band calculations. Overall, the differences in visible and NIR snow albedo under direct radiation are small (within ~0.004), while the hyperspectral calculation leads to noticeably higher visible and NIR albedo under diffuse radiation by up to >0.02 over some hotspots and 0.01-0.02 over most of two polar regions, compared to the 5-band calculations. This is consistent with the analysis of Wang et al. (2022), where the hyperspectral SNICAR calculations tend to have higher snow albedo than the 5-band SNICAR calculations. In addition, the hyperspectral calculation also results in nontrivial differences in aerosol-induced snow albedo forcing (Figure 11), with higher BC forcing (by up to 0.1 W m^{-2} over northern China and Himalayas) and OC forcing (by up to 0.2 W m^{-2} over northern high-latitudes) but lower dust forcing (by up to >0.1 W m^{-2} over northern Eurasia hotspots) compared to the 5-band calculations.

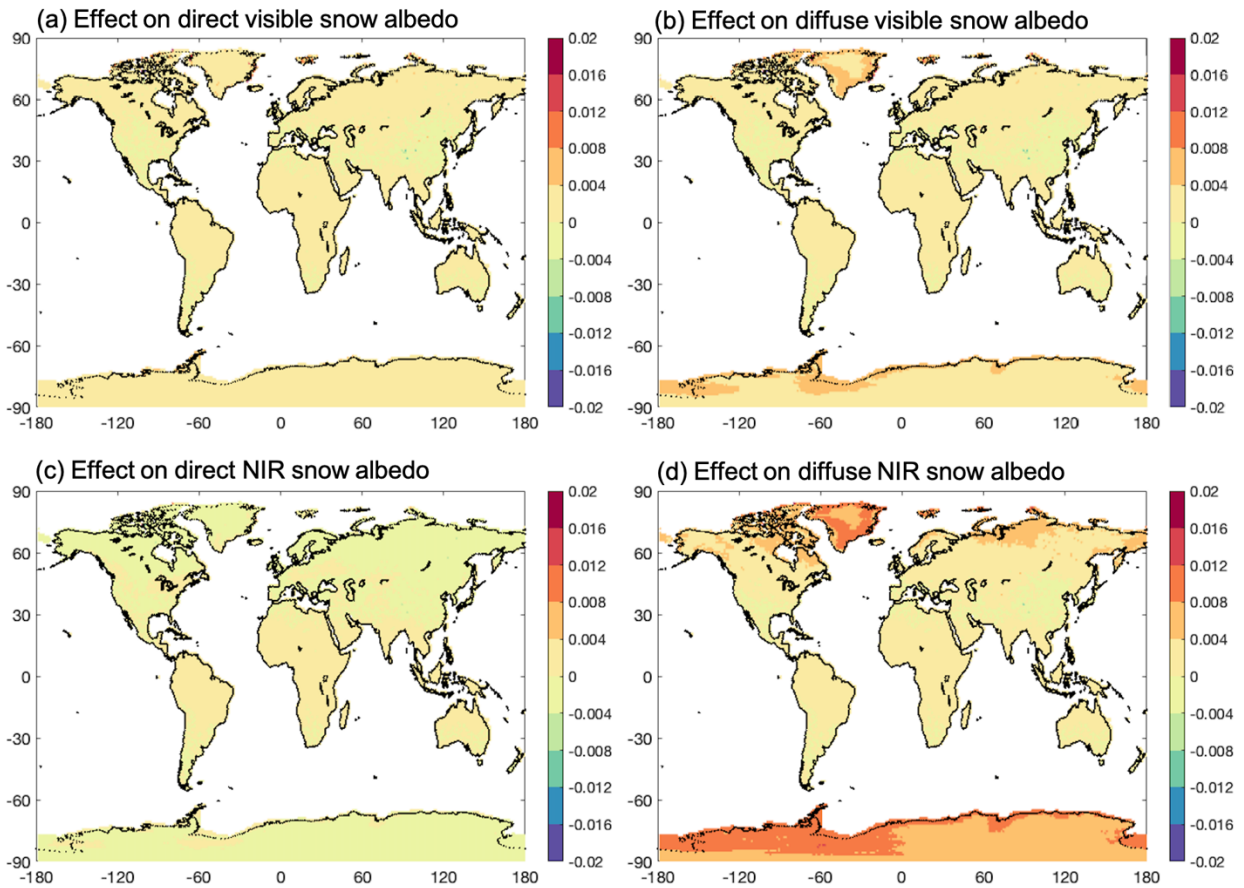

Figure 10. 5-year (2006-2010) annual mean effects of hyperspectral calculations (i.e., differences between simulations using 480 bands and 5 bands): (a) difference for direct-beam visible snow albedo, (b) difference for diffuse visible snow albedo, (c) difference for direct-beam NIR snow albedo, (d) difference for diffuse NIR snow albedo.

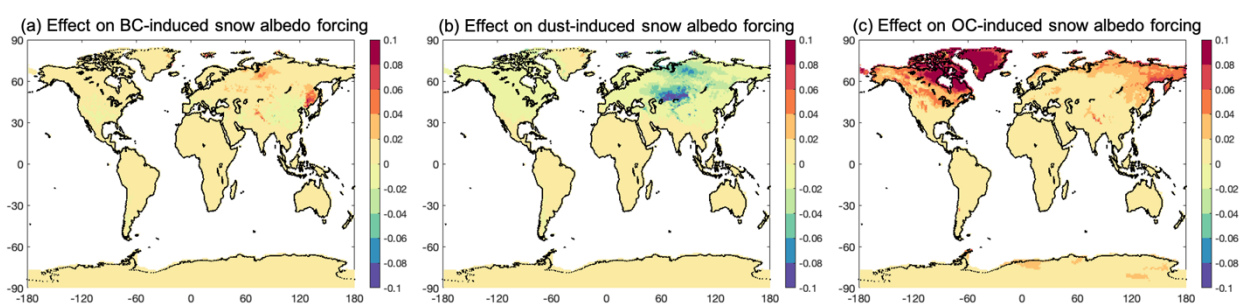

Figure 11. 5-year (2006-2010) all-sky annual mean effects of hyperspectral calculations (i.e., differences between simulations using 480 bands and 5 bands) on aerosol-induced snow albedo forcing (W m^{-2}): (a) difference for BC, (b) difference for dust, (c) difference for OC.

4. Model evaluation

Table 2. Summary of model evaluation statistics

Land surface fields	Model mean biases							
	Northern mid-latitudes (30°N-60°N)		Northern high-latitudes (60°N-90°N)		Southern mid-latitudes (30°S-60°S)		Southern high-latitudes (60°S-90°S)	
	default baseline	new baseline	default baseline	new baseline	default baseline	new baseline	default baseline	new baseline
Surface albedo (100% snow cover)	-0.022	0.004	-0.017	0.007	-0.022	0.005	0.003	0.034
Snow cover	-0.011	-0.009	-0.007	-0.004	-0.025	-0.019	-0.017	-0.012
SWE (mm)	-232.5	-178.3	-77.5	-63.4	-79.7	-64.8	-178.2	-174.0
Snow depth (m)	-2.53	-2.36	-0.67	-0.63	-1.56	-1.51	-5.12	-5.01
2-m temperature (°C)	1.32	1.26	0.53	0.47	0.62	0.55	2.35	2.26

4.1 Surface albedo

Figure 12 shows the comparison between MODIS observed and CLM5 simulated 5-year annual mean white-sky (diffuse) surface albedo over regions with 100% snow cover. The default baseline simulation tends to overestimate visible and NIR snow surface albedo in many parts of northern high-latitudes by about 0.1-0.2, but significantly underestimates the albedo in the northern mid-latitudes by up to 0.5 for the visible band and up to 0.3 for the NIR band, particularly over mountainous regions (Figures 12b, d). Compared to the default baseline result, the new baseline simulation with CLM5-SNICAR enhancements substantially reduces the albedo underestimate in the northern mid-latitudes by up to 0.1 for both visible and NIR bands (Figures 12c, f), primarily due to the use of nonspherical snow grains. The new baseline simulation also increases the snow surface albedo in northern and southern high-latitudes by up to 0.1 mainly at the NIR band, which however exacerbates the model bias in southern high-latitudes. These patterns are generally consistent throughout different seasons (Figures S10 and S11). The assessment for black-sky snow surface albedo shows similar results and conclusions (Figure S12). Table 2 summarizes the mean bias of the default and new baseline simulations. Overall, the new baseline simulation reduces the mean biases of fully snow-covered surface albedo over northern mid- and high-latitudes and southern mid-latitudes but increases the mean bias in southern high-latitudes.

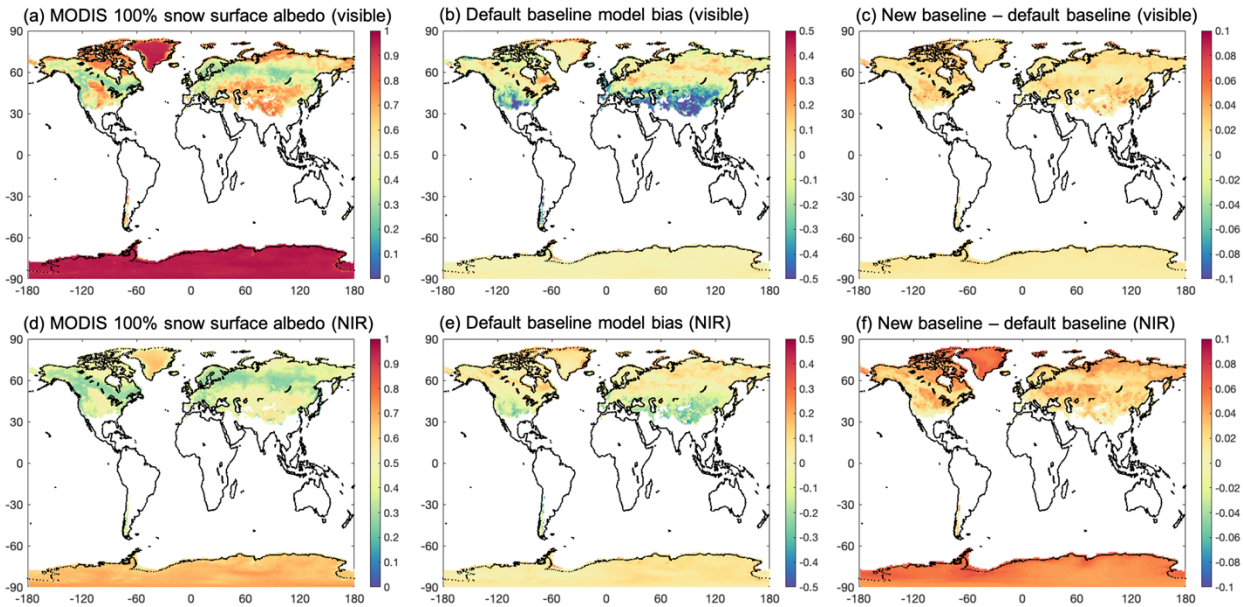

Figure 12. Comparison between MODIS and model simulations of 5-year (2006-2010) annual mean white-sky surface albedo for 100% snow cover grids. First column (a, d): MODIS observations; second column (b, e): default baseline simulation bias; third column (c, f): difference between new and default baseline simulations. First row (a, b, c): visible band; second row (d, e, f): NIR band.

4.2 Snow cover

Figures 13 and S13 shows the comparison between MODIS observed and CLM5 simulated 5-year seasonal mean snow cover fraction. The default baseline simulation significantly underestimates snow cover in the Tibetan Plateau and North American Rocky Mountains across all seasons by about 0.25, with patchy underestimates or overestimates in northern high-latitudes. Compared to the default baseline result, the new baseline simulation reduces the snow cover bias by up to 0.1 in the Tibetan Plateau and North American Rocky Mountains mainly during winter and spring, in many parts of northern Eurasia during spring and summer, and in the southern Andes during summer and fall. This is primarily caused by the increased snow albedo over those regions in the new baseline simulation (Section 4.1), which reduces the solar radiation absorbed by snowpack and hence increases snow cover. Overall, the new baseline simulation reduces the mean

snow cover biases (underestimates) across northern and southern mid- and high-latitudes (Table 2).

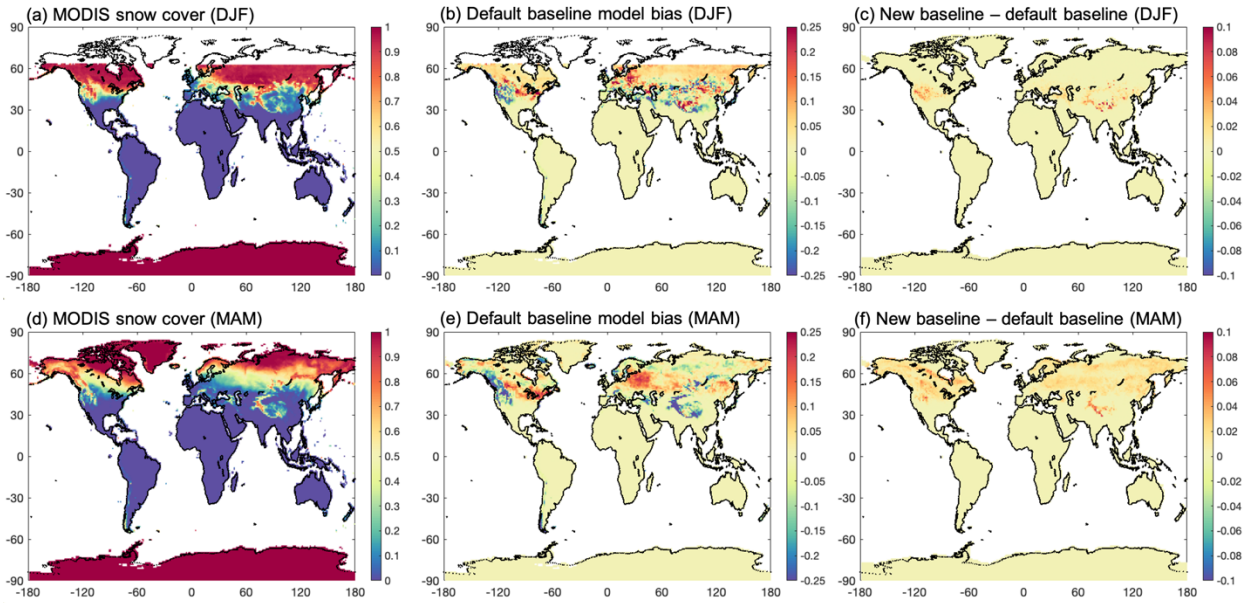

Figure 13. Comparison between MODIS and model simulations of 5-year (2006-2010) seasonal mean snow cover fraction. First column (a, d): MODIS observations; second column (b, e): default baseline simulation bias; third column (c, f): difference between new and default baseline simulations. First row (a, b, c): winter (December-January-February); second row (d, e, f): spring (March-April-May). See Figure S13 for results in summer (June-July-August) and fall (September-October-November) with relatively smaller effects from the new baseline simulation.

4.3 Snow water equivalent

Figures 14 and S14 shows the comparison between ERA-5 and CLM5 simulated 5-year seasonal mean snow water equivalent (SWE). We note that the maximum SWE allowed (i.e., SWE capping) in the CLM5 is set to 10,000 kg/m^2 to prevent unlimited snow building up over glacier regions in model simulations (particularly a coupled climate run), which would cause serious model issues (e.g., incorrect land water storage and ocean salinity). Thus, when evaluating simulated SWE, we screened out the regions with model SWE capping at 10,000 kg/m^2 (mainly Greenland and Antarctic ice sheets), because it is not meaningful to compare the model results with snow capping and the ERA-5 results without SWE capping in those regions.

The default baseline simulation systematically underestimates SWE by more than 50 mm in the Tibetan Plateau, North American Rocky Mountains, the coasts of Greenland, and the southern Andes across all seasons as well as part of northern Eurasia during winter and spring (Figure 14). Compared to the default baseline result, the new baseline simulation reduces the SWE bias by up to 50 mm in the coasts of Greenland across all seasons as well as over the Himalayas and part of North American Rocky Mountains during spring (Figures 14 and S14). This is because the increased snow albedo over those regions in the new baseline simulation (Section 4.1) reduces snow melting and hence increases SWE. Overall, the new baseline simulation reduces the mean SWE biases (underestimates) across mid- and high-latitudes, particularly over northern mid-latitudes (Table 2).

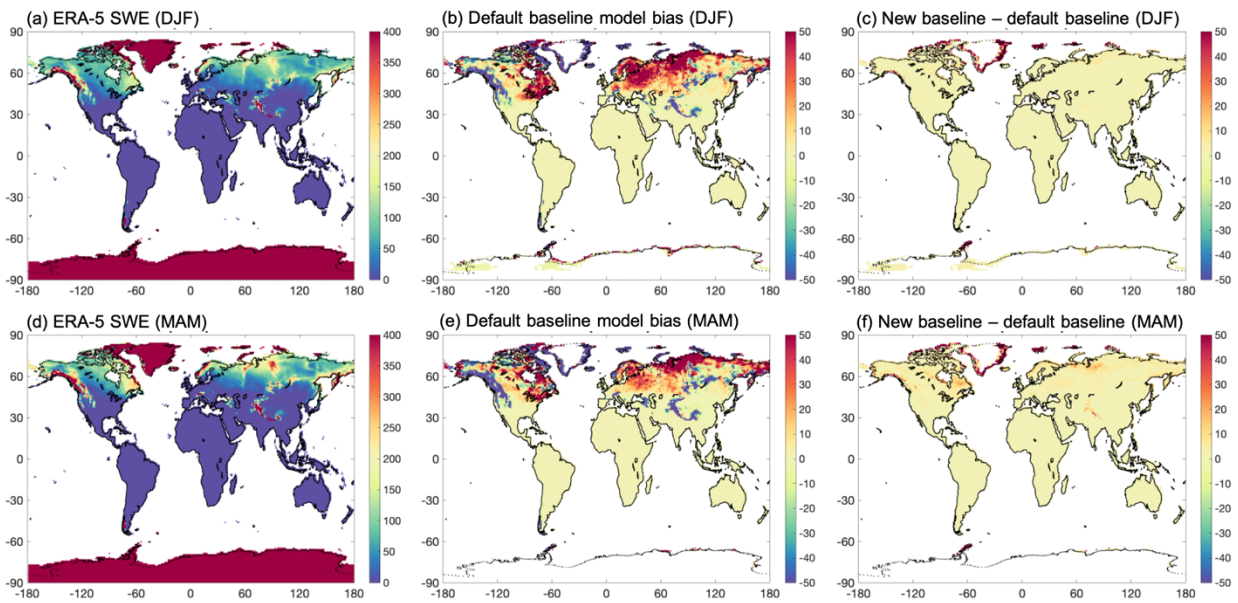

Figure 14. Comparison between ERA-5 and model simulations of 5-year (2006-2010) seasonal mean SWE (mm). First column (a, d): ERA-5 data (values >400 mm also show dark red color); second column (b, e): default baseline simulation bias; third column (c, f): difference between new and default baseline simulations. First row (a, b, c): winter (December-January-February); second row (d, e, f): spring (March-April-May). Note that most Greenland and Antarctic glacier regions with model snow capping at 10,000 kg/m^2 are screened out in second and third columns. See Figure S14 for results in summer (June-July-August) and fall (September-October-November) with relatively smaller effects from the new baseline simulation.

4.4 Snow depth

Figures 15 and S15 shows the comparison between ERA-5 and CLM5 simulated 5-year seasonal mean snow depth. Similar to the SWE evaluation (Sect. 4.3), we screened out the regions with model SWE capping at 10,000 kg/m^2 (mainly Greenland and Antarctic ice sheets). The default baseline simulation substantially underestimates snow depth by 0.2 m or more over the coasts of Greenland, the Tibetan Plateau, and the southern Andes throughout the year, as well as in the North American Rocky Mountains and many parts of northern Eurasia during winter, spring, and fall (Figures 15 and S15). Compared to the default baseline result, the new baseline simulation reduces the snow depth bias by 0.2 m or more over the coasts of Greenland across all seasons and by up to 0.1 m in the Himalayas and part of North American Rocky Mountains during spring (Figures 15 and S15). This is caused by the less light absorption by snowpack over those regions in the new baseline simulation (Section 4.1), which weakens snow densification/melting and hence increases snow depth. Overall, the new baseline simulation reduces the mean snow depth biases (underestimates) across mid- and high-latitudes, particularly in northern mid-latitudes (Table 2).

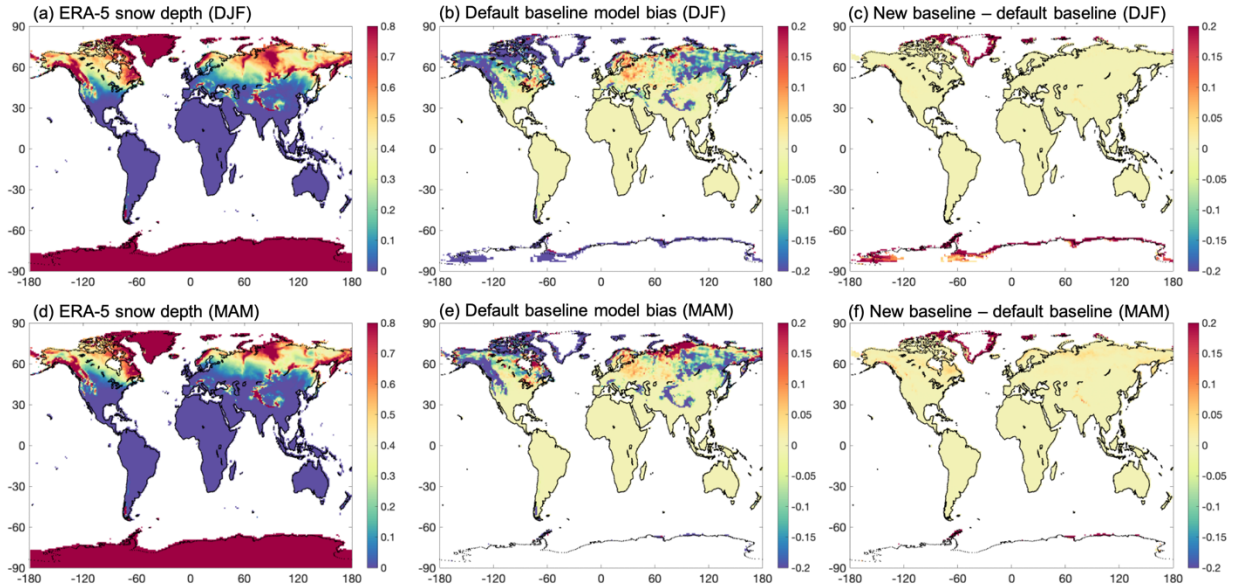

Figure 15. Same as Figure 14, but for snow depth (m) comparison between ERA-5 and model simulations. For ERA-5 snow depth, values >0.8 m also show dark red color in panels (a) and (d). Note that most Greenland and Antarctic glacier regions with model snow capping at 10,000 kg/m^2 are screened out in second and third columns. See Figure S15 for results in summer (June-July-

August) and fall (September-October-November) with relatively smaller effects from the new baseline simulation.

4.5 Surface temperature

Figures 16 and S16 shows the comparison between ERA-5 and CLM5 simulated 5-year annual and seasonal mean surface (2-m) temperature, respectively. The default baseline simulation generally overestimates the surface temperature by ~5°C over the majority of Greenland, Tibetan Plateau, and Antarctic throughout the year, and underestimates in part of northern Eurasia and northern Canada mainly during winter and spring. Compared to the default baseline result, the new baseline simulation reduces the surface temperature overestimates by up to 0.5°C over the Antarctic during winter and fall, Greenland during spring and summer, and part of Tibetan Plateau and North American Rocky Mountains during winter and spring (Figures 16 and S16). This is because of the increased snow albedo and hence less land surface heating by solar radiation absorption over those regions in the new baseline simulation (Section 4.1). The new baseline simulation, however, tends to slightly worsen the model temperature bias in part of northern Eurasia and northern Canada during spring. Overall, the new baseline simulation reduces the mean surface temperature biases (overestimates) across northern and southern mid- and high-latitudes (Table 2). The impact on surface temperature, which is strongly constrained by the forcing temperature in land-only simulations, is expected to be much stronger in a coupled climate simulation through positive snow albedo feedbacks.

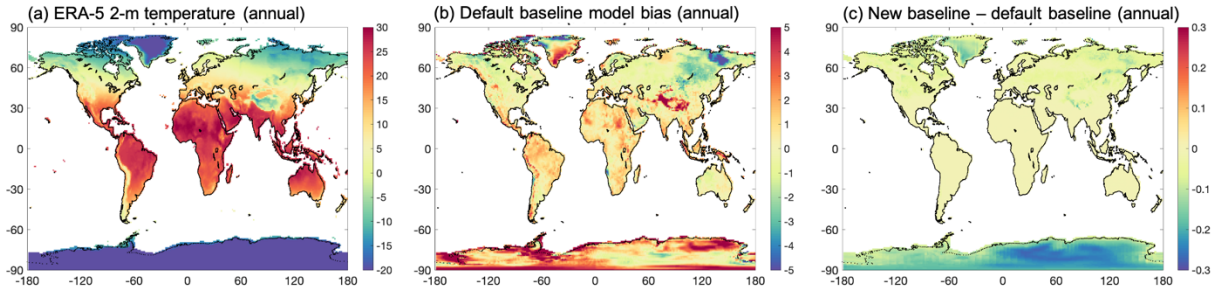

Figure 16. Comparison between ERA-5 and model simulations of 5-year (2006-2010) annual mean 2-m surface temperature (°C): (a) ERA-5 data, (b) default baseline simulation bias, and (c) difference between new and default baseline simulations.

5. Conclusions

In this study, we enhanced the CLM5-SNICAR snow albedo modeling by implementing several new features with more realistic and physical representations of snow-aerosol-radiation interactions. Specifically, we incorporated the following model enhancements: (1) updating ice and aerosol optical properties with more realistic and accurate datasets; (2) adding multiple dust types; (3) adding multiple surface downward solar spectra to account for different atmospheric conditions; (4) incorporating a more accurate adding-doubling radiative transfer solver; (5) adding nonspherical snow grain representation; (6) adding BC-snow and dust-snow internal mixing representations; (7) adding a hyperspectral (480-band versus the default 5-band) modeling capability. These model features/enhancements have been included as new CLM physics/namelist options, which allows for quantifying model sensitivities to snow albedo processes and for conducting relevant multi-physics model ensemble analyses for uncertainty assessment. The model updates will be included in the next CESM/CLM version release. Sensitivity analyses revealed stronger impacts of using the new adding-doubling solver, nonspherical snow grains, and BC/dust-snow internal mixing than the other new features/enhancements.

These enhanced snow albedo representations improve the CLM5 modeled global snowpack evolution and land surface conditions. Specifically, the enhanced CLM5-SNICAR leads to (1) a reduced snow surface albedo bias in northern mid-latitudes across all seasons; (2) a reduced snow cover bias in the Tibetan Plateau and North American Rocky Mountains during winter and spring, part of northern Eurasia during spring and summer, and the southern Andes during summer and fall; (3) a reduced SWE bias in the coasts of Greenland throughout the year and over the Tibetan Plateau and North American Rocky Mountains during spring; (4) a reduced snow depth bias in the coasts of Greenland throughout the year and in part of the Tibetan plateau and North American Rocky Mountains during spring; (5) a reduced surface temperature bias over the Antarctic during winter and fall, Greenland during spring and summer, and part of the Tibetan Plateau and North American Rocky Mountains during winter and spring. We note, however, that there are some regions without any model improvement or even with degradation by using the enhanced CLM5-SNICAR, such as the snow surface albedo in some high-latitude regions.

In future studies, coupled climate model simulations with the enhanced CLM5-SNICAR are needed to assess the full climatic impacts of the snow albedo enhancements added in this study, which are expected to be stronger than those shown here due to positive snow albedo feedback.

Acknowledgements

The authors declare no conflict of interest. This research was funded by the U.S. National Oceanic and Atmospheric Administration (NOAA) Climate Process Team project Award# 4000178550 and Award# NA19OAR4310243. NCAR is sponsored by the U.S. National Science Foundation. Any opinions, findings, conclusions, or recommendations expressed in this publication are those of the authors and do not necessarily reflect the views of the National Science Foundation.

Open Research

The default CLM5-SNICAR (CTSM Development Team, 2022) code is at:
https://github.com/ESCOMP/CTSM

The enhanced CLM5-SNICAR (CTSM Development Team, 2022) code is at:
https://github.com/ESCOMP/CTSM/pull/1861

MODIS surface albedo data (MCD43C3; Schaaf and Wang, 2021) is available at:
https://lpdaac.usgs.gov/products/mcd43c3v061/

MODIS snow cover data (MOD10C1 and MYD10C1; Hall and Riggs, 2021a, b) is available at:
https://nsidc.org/data/mod10c1/versions/61 and https://nsidc.org/data/myd10c1/versions/61

ERA-5 land data (SWE, snow depth, surface temperature; Muñoz Sabater, 2019) is available at:
https://cds.climate.copernicus.eu/cdsapp#!/dataset/reanalysis-era5-land-monthly-means?tab=overview

The model data generated in this study (He et al., 2023) is at:
https://doi.org/10.5281/zenodo.7986830

References

Abolafia-Rosenzweig, R., He, C., McKenzie Skiles, S., Chen, F., & Gochis, D. (2022). Evaluation and optimization of snow albedo scheme in Noah-MP land surface model using in situ spectral observations in the Colorado Rockies. Journal of Advances in Modeling Earth Systems, 14, e2022MS003141. https://doi. org/10.1029/2022MS003141

Bales, R. C., Molotch, N. P., Painter, T. H., Dettinger, M. D., Rice, R., & Dozier, J. (2006). Mountain hydrology of the western United States. Water Resources Research, 42(8), 1–13. https://doi.org/10.1029/2005WR004387

Briegleb BP, Light B (2007) A delta-eddington multiple scattering parameterization for solar radiation in the sea ice component of the community climate system Model. NCAR Tech. Note 472 1 STR, 100 pp

Chen, F., Barlage, M., Tewari, M., Rasmussen, R., Jin, J., Lettenmaier, D., et al. (2014). Modeling seasonal snowpack evolution in the complex terrain and forested Colorado Headwaters region: A model intercomparison study. Journal of Geophysical Research - D: Atmos- pheres, 119, 13795–13819. https://doi.org/10.1002/2014JD022167

Cook, J. M., Hodson, A. J., Gardner, A. S., Flanner, M., Tedstone, A. J., Williamson, C., ... and Tranter, M. (2017). Quantifying bioalbedo: a new physically based model and discussion of empirical methods for characterising biological influence on ice and snow albedo. The Cryosphere, 11(6), 2611-2632.

CTSM Development Team. (2022). ESCOMP/CTSM: NEON release: Some NEON updates fixing AG sites, update MOSART, small fixes (ctsm5.1.dev114). [Software]. Zenodo. https://doi.org/10.5281/zenodo.7342803

Danabasoglu, G., Lamarque, J. F., Bacmeister, J., et al. (2020). The Community Earth System Model Version 2 (CESM2). Journal of Advances in Modeling Earth Systems, 12, doi:10.1029/2019MS001916.

Dang C, Brandt RE, Warren SG (2015) Parameterizations for narrowband and broadband albedo of pure snow and snow containing mineral dust and black carbon. Journal of Geophysical Research: Atmospheres 120, 5446–5468. doi:10.1002/2014JD022646

Dang C, Fu Q, Warren SG (2016) Effect of snow grain shape on snow albedo. Journal of the Atmospheric Sciences 73(9), 3573–3583. doi:10.1175/JAS-D-15-0276.1

Dang C, Zender CS, Flanner MG (2019) Intercomparison and improvement of two-stream shortwave radiative transfer schemes in Earth system models for a unified treatment of cryospheric surfaces. The Cryosphere 13(9), 2325–2343. doi:10.5194/tc-13-2325-2019

Dirmeyer, P. A., Gao, X., Zhao, M., Guo, Z., Oki, T., and Hanasaki, N.: GSWP-2: Multimodel Analysis and Implications for Our Per- ception of the Land Surface, B. Am. Meteorol. Soc., 87, 1381– 1398, 2006.

Dominé, F., Lauzier, T., Cabanes, A., Legagneux, L., Kuhs, W. F., Techmer, K., & Heinrichs, T. (2003). Snow metamorphism as revealed by scanning electron microscopy. Microscopy Research and Technique, 62(1), 33–48. https://doi.org/10.1002/jemt.10384

Dumont, M., Tuzet, F., Gascoin, S., Picard, G., Kutuzov, S., Lafaysse, M., ... and Painter, T. H. (2020). Accelerated snow melt in the Russian Caucasus mountains after the Saharan dust outbreak in March 2018. Journal of Geophysical Research: Earth Surface, 125(9), e2020JF005641.

Dumont, M., Flin, F., Malinka, A., Brissaud, O., Hagenmuller, P., Lapalus, P., ... and Ando, E. (2021). Experimental and model-based investigation of the links between snow bidirectional reflectance and snow microstructure. The Cryosphere, 15(8), 3921-3948.

Erbe, E. F., Rango, A., Foster, J., Josberger, E. G., Pooley, C., & Wergin, W. (2003). Collecting, shipping, storing, and imaging snow crystals and ice grains with low-temperature scanning electron microscopy. Microscopy Research and Technique, 62(1), 19–32. https://doi.org/10.1002/ jemt.10383

Essery, R., Rutter, N., Pomeroy, J., Baxter, R., Stahli, M., Gustafsson, D., et al. (2009). SNPWMIP2, An evalutation of froest snow process simulations. Bulletin of the American Meteorological Society, 90, 1120–1135.

Flanner, M. G., Zender, C. S., Randerson, J. T., and Rasch, P. J. (2007). Present-day climate forcing and response from black carbon in snow. Journal of Geophysical Research: Atmospheres, 112(D11).

Flanner, M. G., Shell, K. M., Barlage, M., Perovich, D. K., and Tschudi, M. A. (2011). Radiative forcing and albedo feedback from the Northern Hemisphere cryosphere between 1979 and 2008. Nature Geoscience, 4(3), 151–155. https://doi.org/10.1038/ngeo1062

Flanner, M. G., Liu, X., Zhou, C., Penner, J. E., and Jiao, C. (2012). Enhanced solar energy absorption by internally-mixed black carbon in snow grains. Atmospheric Chemistry and Physics, 12(10), 4699-4721.

Flanner, M. G., Gardner, A. S., Eckhardt, S., Stohl, A., and Perket, J. (2014). Aerosol radiative forcing from the 2010 Eyjafjallajökull volcanic eruptions. Journal of Geophysical Research: Atmospheres, 119(15), 9481-9491.

Flanner, M. G., Arnheim, J. B., Cook, J. M., Dang, C., He, C., Huang, X., ... and Zender, C. S. (2021). SNICAR-ADv3: a community tool for modeling spectral snow albedo. Geoscientific Model Development, 14(12), 7673-7704.

Gardner AS, Sharp MJ (2010) A review of snow and ice albedo and the development of a new physically based broadband albedo parameterization. Journal of Geophysical Research 115, F01009. doi:10.1029/ 2009JF001444

Gleason, K. E., McConnell, J. R., Arienzo, M. M., Chellman, N., & Calvin, W. M. (2019). Four-fold increase in solar forcing on snow in western US burned forests since 1999. Nature communications, 10(1), 2026.

Gelman Constantin, J., Ruiz, L., Villarosa, G., Outes, V., Bajano, F. N., He, C., ... and Dawidowski, L. (2020). Measurements and modeling of snow albedo at Alerce Glacier, Argentina: effects of volcanic ash, snow grain size, and cloudiness. The Cryosphere, 14(12), 4581-4601.

Golaz, J. C., Caldwell, P. M., Van Roekel, L. P., Petersen, M. R., Tang, Q., Wolfe, J. D., ... & Zhu, Q. (2019). The DOE E3SM coupled model version 1: Overview and evaluation at standard resolution. Journal of Advances in Modeling Earth Systems, 11(7), 2089-2129.

Gul, C., Mahapatra, P. S., Kang, S., Singh, P. K., Wu, X., He, C., ... and Puppala, S. P. (2021). Black carbon concentration in the central Himalayas: Impact on glacier melt and potential source contribution. Environmental Pollution, 275, 116544.

Hall, D. K. and G. A. Riggs. (2021a). MODIS/Terra Snow Cover Daily L3 Global 0.05Deg CMG, Version 61 [Dataset]. Boulder, Colorado USA. NASA National Snow and Ice Data Center Distributed Active Archive Center. https://doi.org/10.5067/MODIS/MOD10C1.061. Date Accessed 06-06-2023.

Hall, D. K. and G. A. Riggs. (2021b). MODIS/Aqua Snow Cover Daily L3 Global 0.05Deg CMG, Version 61 [Dataset]. Boulder, Colorado USA. NASA National Snow and Ice Data Center Distributed Active Archive Center. https://doi.org/10.5067/MODIS/MYD10C1.061. Date Accessed 06-06-2023.

Hao, D., Bisht, G., Rittger, K., Bair, E., He, C., Huang, H., ... & Leung, L. R. (2023). Improving snow albedo modeling in the E3SM land model (version 2.0) and assessing its impacts on snow and surface fluxes over the Tibetan Plateau. Geoscientific Model Development, 16(1), 75-94.

He, C., Q. Li, K.-N. Liou, Y. Takano, Y. Gu, L. Qi, Y. Mao, and L. R. Leung (2014), Black carbon radiative forcing over the Tibetan Plateau, Geophys. Res. Lett., 41, 7806–7813, doi:10.1002/2014GL062191.

He, C., Y. Takano, and K. N. Liou (2017a). Close packing effects on clean and dirty snow albedo and associated climatic implications. Geophys. Res. Lett., 44, 3719–3727

He, C., Y. Takano, K. N. Liou, P. Yang, Q. Li, and F. Chen (2017b). Impact of Snow Grain Shape and Black Carbon–Snow Internal Mixing on Snow Optical Properties: Parameterizations for Climate Models. Journal of Climate, 30(24), 10019-10036.

He, C., K. N. Liou, Y. Takano, P. Yang, L. Qi, and F. Chen (2018a). Impact of grain shape and multiple black carbon internal mixing on snow albedo: Parameterization and radiative effect analysis. J. Geophys. Res.-Atmos., 123, 1253–1268.

He, C., K. N. Liou, and Y. Takano (2018b). Resolving size distribution of black carbon internally mixed with snow: Impact on snow optical properties and albedo. Geophys. Res. Lett., 45, 2697–2705.

He, C., Flanner, M. G., Chen, F., Barlage, M., Liou, K. N., Kang, S., Ming, J., and Qian, Y. (2018c): Black carbon-induced snow albedo reduction over the Tibetan Plateau: uncertainties from snow grain shape and aerosol–snow mixing state based on an updated SNICAR model, Atmos. Chem. Phys., 18, 11507-11527, doi:10.5194/acp-18-11507-2018.

He, C., Chen, F., Barlage, M., Liu, C., Newman, A., Tang, W., et al. (2019a). Can convection-permitting modeling provide decent precipitation for offline high-resolution snowpack simulations over mountains?. Journal of Geophysical Research: Atmospheres, 124, 12,631–12,654. https://doi.org/ 10.1029/2019JD030823

He, C., Liou, K. N., Takano, Y., Chen, F., and Barlage, M. (2019b). Enhanced snow absorption and albedo reduction by dust-snow internal mixing: modeling and parameterization. Journal of Advances in Modeling Earth Systems, 11(11), 3755-3776.

He, C., and Flanner, M. (2020). Snow Albedo and Radiative Transfer: Theory, Modeling, and Parameterization. In Springer Series in Light Scattering (pp. 67-133). Springer, Cham.

He, C., Chen, F., Abolafia-Rosenzweig, R., Ikeda, K., Liu, C., & Rasmussen, R. (2021). What causes the unobserved early-spring snowpack ablation in convection-permitting WRF modeling over Utah mountains? Journal of Geophysical Research: Atmospheres, 126, e2021JD035284. https://doi. org/10.1029/2021JD035284

He, C. (2022): Modeling light-absorbing particle-snow-radiation interactions and impacts on snow albedo: fundamentals, recent advances, and future directions, Environmental Chemistry, doi:10.1071/EN22013

He, C., M. Flanner, D. Lawrence, and Y. Gu (2023). Model dataset for the journal publication entitled "New features and enhancements in Community Land Model (CLM5) snow albedo modeling: description, sensitivity, and evaluation" [Dataset]. Zenodo. https://doi.org/10.5281/zenodo.7986830

Huang, H., Qian, Y., He, C., Bair, E. H., & Rittger, K. (2022). Snow albedo feedbacks enhance snow impurity- induced radiative forcing in the Sierra Nevada. Geophysical Research Letters, 49, e2022GL098102. https://doi. org/10.1029/2022GL098102

Kaempfer TU, Hopkins MA, Perovich DK (2007) A three-dimensional microstructure-based photon-tracking model of radiative transfer in snow. J Geophys Res Atmos 112(D24)

Kokhanovsky, A. A., and E. P. Zege (2004). Scattering optics of snow. Applied Optics, 43(7), 1589-1602.

Lamarque, J.-F., Bond, T. C., Eyring, V., et al.: Historical (1850–2000) gridded anthropogenic and biomass burning emissions of reactive gases and aerosols: methodol- ogy and application, Atmos. Chem. Phys., 10, 7017–7039, https://doi.org/10.5194/acp-10-7017-2010, 2010.

Lawrence, D. M., Fisher, R. A., Koven, C. D., Oleson, K. W., Swenson, S. C., Bonan, G., et al. (2019). The Community Land Model version 5: Description of new features, benchmarking,

and impact of forcing uncertainty. Journal of Advances in Modeling Earth Systems, 11, 4245–4287. https://doi.org/10.1029/2018MS001583

Lee, W. L., Liou, K. N., He, C., Liang, H. C., Wang, T. C., Li, Q., ... and Yue, Q. (2017). Impact of absorbing aerosol deposition on snow albedo reduction over the southern Tibetan plateau based on satellite observations. Theoretical and Applied Climatology, 129(3), 1373-1382.

Li, C., Yan, F., Kang, S., Yan, C., Hu, Z., Chen, P., ... & Stubbins, A. (2021). Carbonaceous matter in the atmosphere and glaciers of the Himalayas and the Tibetan plateau: An investigative review. Environment International, 146, 106281.

Libois Q, Picard G, France JL, Arnaud L, Dumont M, Carmagnola CM, King MD (2013) Influence of grain shape on light penetration in snow. The Cryosphere 7(6), 1803–1818. doi:10.5194/tc-7-1803-2013

Liou, K. N., Takano, Y., He, C., Yang, P., Leung, L. R., Gu, Y., and Lee, W. L.: Stochastic parameterization for light absorp- tion by internally mixed BC/dust in snow grains for application to climate models, J. Geophys. Res.-Atmos., 119, 7616–7632, https://doi.org/10.1002/2014JD021665, 2014.

Liu, D., He, C., Schwarz, J. P., & Wang, X. (2020). Lifecycle of light-absorbing carbonaceous aerosols in the atmosphere. NPJ climate and atmospheric science, 3(1), 40.

Liu, X., Easter, R. C., Ghan, S. J., Zaveri, R., Rasch, P., Shi, X., Lamarque, J.-F., et al.: Toward a minimal representation of aerosols in climate models: description and evaluation in the Community Atmosphere Model CAM5, Geosci. Model Dev., 5, 709–739, https://doi.org/10.5194/gmd-5-709-2012, 2012.

Muñoz Sabater, J. (2019): ERA5-Land monthly averaged data from 1950 to present. Copernicus Climate Change Service (C3S) Climate Data Store (CDS). [Dataset]. doi:10.24381/cds.68d2bb30 (Accessed on 2023-06-06)

Oaida, C.M., Xue, Y., Flanner, M.G., Skiles, S.M., De Sales, F. and Painter, T.H. (2015). Improving snow albedo processes in WRF/SSiB regional climate model to assess impact of dust and black carbon in snow on surface energy balance and hydrology over western US. Journal of Geophysical Research: Atmospheres, 120(8), pp.3228-3248.

Painter, T. H., Deems, J. S., Belnap, J., Hamlet, A. F., Landry, C. C., and Udall, B. (2010). Response of Colorado River runoff to dust radiative forcing in snow. Proceedings of the National Academy of Sciences, 107(40), 17125-17130.

Perovich, D. K. and Govoni, J. W.: Absorption Coefficients Of Ice From 250 To 400 nm, Geophys. Res. Lett., 18, 1233–1235, https://doi.org/10.1029/91GL01642, 1991.

Picard, G., Libois, Q., and Arnaud, L.: Refinement of the ice ab- sorption spectrum in the visible using radiance profile measurements in Antarctic snow, The Cryosphere, 10, 2655–2672, https://doi.org/10.5194/tc-10-2655-2016, 2016.

Picard, G., Dumont, M., Lamare, M., Tuzet, F., Larue, F., Pirazzini, R., and Arnaud, L.: Spectral albedo measurements over snow-covered slopes: theory and slope effect corrections, The Cryosphere, 14, 1497–1517, https://doi.org/10.5194/tc-14-1497- 2020, 2020.

Polashenski, C. M., Dibb, J. E., Flanner, M. G., Chen, J. Y., Courville, Z. R., Lai, A. M., Schauer, J. J., Shafer, M. M., and Bergin, M.: Neither dust nor black carbon causing apparent albedo decline in Greenland's dry snow zone: Implications for MODIS C5 surface reflectance, Geophys. Res. Lett., 42, 9319– 9327, https://doi.org/10.1002/2015GL065912, 2015.

Pu, W., Shi, T., Cui, J., Chen, Y., Zhou, Y., and Wang, X. (2021). Enhancement of snow albedo reduction and radiative forcing due to coated black carbon in snow. The Cryosphere, 15(5), 2255-2272.

Qian, Y., Yasunari, T. J., Doherty, S. J., Flanner, M. G., Lau, W. K., Ming, J., ... and Zhang, R. (2015). Light-absorbing particles in snow and ice: Measurement and modeling of climatic and hydrological impact. Advances in Atmospheric Sciences, 32(1), 64-91.

Räisänen, P., R. Makkonen, A. Kirkevåg, and J. B. Debernard (2017). Effects of snow grain shape on climate simulations: sensitivity tests with the Norwegian Earth System Model. The Cryosphere, 11, 2919–2942.

Roeckner E, Bauml G, Bonaventura L et al (2003) The atmospheric general circulation model ECHAM5. Part I: model description. Max Planck Institute for Meteorology, Rep 349, 127 pp

Saito M, Yang P, Loeb NG, Kato S (2019) A novel parameterization of snow albedo based on a two-layer snow model with a mixture of grain habits. J Atmos Sci 76(5):1419–1436

Scanza, R. A., Mahowald, N., Ghan, S., Zender, C. S., Kok, J. F., Liu, X., Zhang, Y., and Albani, S.: Modeling dust as component minerals in the Community Atmosphere Model: development of framework and impact on radiative forcing, Atmos. Chem. Phys., 15, 537–561, https://doi.org/10.5194/acp-15-537-2015, 2015.

Schaaf, C., Wang, Z. (2021). MODIS/Terra+Aqua BRDF/Albedo Albedo Daily L3 Global 0.05Deg CMG V061 [Dataset]. NASA EOSDIS Land Processes DAAC. Accessed 2023-06-06 from https://doi.org/10.5067/MODIS/MCD43C3.061

Shi T, Cui J, Chen Y, Zhou Y, Pu W, Xu X, et al. (2021) Enhanced light absorption and reduced snow albedo due to internally mixed mineral dust in grains of snow. Atmospheric Chemistry and Physics 21(8), 6035–6051. doi:10.5194/acp-21-6035-2021

Shi, T., He, C., Zhang, D., Zhang, X., Niu, X., Xing, Y., ... & Wang, X. (2022). Opposite Effects of Mineral Dust Nonsphericity and Size on Dust-Induced Snow Albedo Reduction. Geophysical Research Letters, 49(12), e2022GL099031.

Skiles, S. M. and Painter, T.: Daily evolution in dust and black carbon content, snow grain size, and snow albedo during snowmelt, Rocky Mountains, Colorado, J. Glaciol., 63, 118–132, https://doi.org/10.1017/jog.2016.125, 2017.

Skiles, S. M., Flanner, M., Cook, J. M., Dumont, M., and Painter, T. H. (2018). Radiative forcing by light-absorbing particles in snow. Nature Climate Change, 8(11), 964-971.

Stamnes K, Tsay SC, Wiscombe W, Jayaweera K (1988) Numerically stable algorithm for discrete-ordinate-method radiative transfer in multiple scattering and emitting layered media. Appl Opt 27(12):2502–2509

Thackeray, C. W., and Fletcher, C. G. (2016). Snow albedo feedback: Current knowledge, importance, outstanding issues and future directions. Progress in Physical Geography, 40(3), 392-408.

Thackeray, C. W., Fletcher, C. G., & Derksen, C. (2019). Diagnosing the impacts of Northern Hemisphere surface albedo biases on simulated climate. Journal of Climate, 32(6), 1777-1795.

Toon, O. B., McKay, C. P., Ackerman, T. P., and Santhanam, K.: Rapid calculation of radiative heating rates and photodissocia- tion rates in inhomogeneous multiple scattering atmospheres, J. Geophys. Res., 94, 16287–16301, 1989.

Toure, A. M., Luojus, K., Rodell, M., Beaudoing, H., & Getirana, A. (2018). Evaluation of simulated snow and snowmelt timing in the Community Land Model using satellite-based products and streamflow observations. Journal of Advances in Modeling Earth Systems, 10, 2933–2951. https://doi.org/ 10.1029/2018MS001389

Tuzet F, Dumont M, Lafaysse M et al (2017) A multilayer physically based snowpack model simulating direct and indirect radiative impacts of light-absorbing impurities in snow. Cryosphere, 11(6):2633–2653

Verseghy DL (1991) CLASS–A Canadian land surface scheme for GCMs. I. Soil model. Int J Climatol 11(2):111–133

Vionnet V, Brun E, Morin S et al (2012) The detailed snowpack scheme Crocus and its implementation in SURFEX v7. 2. Geosci Model Dev 5:773–791

Wang, W., He, C., Moore, J., Wang, G., & Niu, G. Y. (2022). Physics-Based Narrowband Optical Parameters for Snow Albedo Simulation in Climate Models. Journal of Advances in Modeling Earth Systems, 14(1), e2020MS002431.

Warren, S. G.: Optical constants of ice from the ultraviolet to the microwave, Appl. Optics, 23, 1206–1225, 1984.

Warren, S. G. and Brandt, R. E.: Optical constants of ice from the ultraviolet to the microwave: A revised compilation, J. Geophys. Res., 113, D14220, https://doi.org/10.1029/2007JD009744, 2008.

Warren SG, Wiscombe WJ (1980) A model for the spectral albedo of snow. II: Snow containing atmospheric aerosols. J Atmos Sci 37(12):2734–2745

Wiscombe WJ, Warren SG (1980) A model for the spectral albedo of snow. I: Pure snow. Journal of the Atmospheric Sciences 37(12), 2712–2733.

Williamson, C. J., Cook, J., Tedstone, A., Yallop, M., McCutcheon, J., Poniecka, E., ... and Anesio, A. (2020). Algal photophysiology drives darkening and melt of the Greenland Ice Sheet. Proceedings of the National Academy of Sciences, 117(11), 5694-5705.

Yan, F., He, C., Kang, S., Chen, P., Hu, Z., Han, X., ... & Li, C. (2019). Deposition of organic and black carbon: direct measurements at three remote stations in the Himalayas and Tibetan Plateau. Journal of Geophysical Research: Atmospheres, 124(16), 9702-9715.

Yang, Z. L., Dickinson, R. E., Robock, A., & Vinnikov, K. Y. (1997). Validation of the snow submodel of the biosphere–atmosphere transfer scheme with Russian snow cover and meteorological observational data. Journal of climate, 10(2), 353-373.

Yi, K., Meng, J., Yang, H., He, C., Henze, D. K., Liu, J., ... and Tao, S. (2019). The cascade of global trade to large climate forcing over the Tibetan Plateau glaciers. Nature communications, 10(1), 1-9.

Young, C. L., Sokolik, I. N., Flanner, M. G., and Dufek, J. (2014). Surface radiative impacts of ash deposits from the 2009 eruption of Redoubt volcano. Journal of Geophysical Research: Atmospheres, 119(19), 11-387.

New features and enhancements in Community Land Model (CLM5) snow albedo modeling: description, sensitivity, and evaluation

Cenlin He[1], Mark Flanner[2], David M. Lawrence[1], Yu Gu[3]

1. National Center for Atmospheric Research (NCAR), Boulder, CO, USA
2. University of Michigan Ann Arbor, MI, USA
3. University of California Los Angeles (UCLA), Los Angeles, CA, USA

Correspondence to: Cenlin He (cenlinhe@ucar.edu)

Key points

- We enhance CLM5 snow albedo modeling by including more realistic and physical representations of snow-aerosol-radiation interactions
- The new adding-doubling solver, nonspherical snow grains, and aerosol-snow internal mixing show stronger impacts than other new features
- The enhanced snow albedo representation improves the CLM simulated global snowpack evolution and land surface conditions

Abstract

We enhance the Community Land Model (CLM) snow albedo modeling by implementing several new features with more realistic and physical representations of snow-aerosol-radiation interactions. Specifically, we incorporate the following model enhancements: (1) updating ice and aerosol optical properties with more realistic and accurate datasets, (2) adding multiple dust types, (3) adding multiple surface downward solar spectra to account for different atmospheric conditions, (4) incorporating a more accurate adding-doubling radiative transfer solver, (5) adding nonspherical snow grain representation, (6) adding black carbon-snow and dust-snow internal mixing representations, and (7) adding a hyperspectral (480-band versus the default 5-band) modeling capability. These model features/enhancements are included as new CLM physics/namelist options, which allows for quantification of model sensitivity to snow albedo

processes and for multi-physics model ensemble analyses for uncertainty assessment. The model updates will be included in the next CLM version release. Sensitivity analyses reveal stronger impacts of using the new adding-doubling solver, nonspherical snow grains, and aerosol-snow internal mixing than the other new features/enhancements. These enhanced snow albedo representations improve the CLM simulated global snowpack evolution and land surface conditions, with reduced biases in simulated snow surface albedo, snow cover, snow water equivalent, snow depth, and surface temperature, particularly over northern mid-latitude mountainous regions and polar regions.

Plain Language Summary

Snow albedo plays a critical role in the Earth system, affecting land surface energy and water balance and related hydrological processes and also serving as an important land process that feeds back to the atmosphere. Several recent studies have identified new or improved physical representations of snow-aerosol-radiation interactions that show promise to improve snow albedo modeling. In this study, we leverage those recent advances in snow albedo modeling to implement a number of relevant new features into the widely-used Community Land Model (CLM), which is the land component of the Community Earth System Model (CESM). Specifically, we improve the ice and aerosol optical properties, the treatment of dust types and downward solar spectra, the albedo computation algorithm, the representation of snow grain shape and aerosol-snow mixing state, and the spectral calculation capability. These model updates will be included in the next CLM version release. Overall, the enhanced snow albedo representations improve the simulated global snowpack evolution and related land surface conditions.

1. Introduction

Snow albedo plays a key role in altering surface energy and water balance in the Earth system. It affects not only the evolution of snowpack states (e.g., snow depth, snow water equivalent (SWE), and snow cover) and hydrology (e.g., runoff/streamflow, reservoir storage, and flooding/drought) but also the atmosphere (e.g., surface temperature, humidity, local/regional boundary layer height, and clouds) through positive snow albedo feedback and land-atmosphere interactions (Bales et al., 2006; Painter et al., 2010; Flanner et al., 2011; Qian et al., 2015; Lee et

al., 2017; Skiles et al., 2018; Gleason et al., 2019; Yi et al., 2019; Dumont et al., 2020; Gul et al., 2021; Huang et al., 2022). Snow albedo represents an important source of uncertainty in regional and global weather, climate, and hydrological modeling (Essery et al. 2009; Chen et al., 2014; Oaida et al., 2015; Thackeray and Fletcher, 2016; Räisänen et al., 2017; He et al., 2019a, 2021). Snow albedo is affected by many factors, including snow grain size and shape, snow depth, snow density, snow microstructure, light-absorbing particles (LAPs) present in the snowpack, the solar zenith angle, and the downward solar spectrum (Wiscombe and Warren, 1980; Kokhanovsky and Zege, 2004; Flanner et al., 2007, 2021; He et al., 2014, 2017a; Liou et al. 2014; Dang et al., 2015; Gelman Constantin et al., 2020; He and Flanner, 2020; Picard et al., 2020; Dumont et al., 2021). Accurate simulation of snow albedo requires realistic characterization and physical representation of those key factors in land, weather, and climate models.

In the past decades, many empirical or semi-physical parameterizations have been developed to statistically link snow albedo with snowpack properties and environment conditions for application in weather and climate models (Verseghy, 1991; Yang et al., 1997; Roeckner et al., 2003; Gardner and Sharp, 2010; Vionnet et al., 2012; Abolafia-Rosenzweig et al., 2022), which however have their own limitations and uncertainties (He and Flanner, 2020). To achieve higher accuracy of snow albedo, several physics-based snowpack radiative transfer models have been developed, such as those based on the two-stream radiative transfer (Flanner et al., 2007; Libois et al., 2013; Tuzet et al. 2017), the Discrete-Ordinate-Method Radiative Transfer (DISORT) (Stamnes et al., 1988), the adding-doubling radiative transfer (Briegleb and Light, 2007; Dang et al., 2019), the Approximate Asymptotic Radiative Transfer (AART) Theory (Kokhanovsky and Zege, 2004; Libois et al., 2013), and the Monte Carlo Photon Tracing method (Kaempfer et al., 2007). Among them, the Snow, Ice, and Aerosol Radiative (SNICAR) model (Flanner et al, 2007, 2021) stands as one of the most widely used snowpack radiative transfer models, which has been implemented in several land and climate models including the Community Earth System Model (CESM)/Community Land Model (CLM; Lawrence et al., 2019) and the DOE's Energy Exascale Earth System Model (E3SM) Land Model (ELM; Golaz et al., 2019).

In previous snow radiative transfer models, it was a common practice to treat snow grains as spheres, externally mixed with LAPs such as black carbon (BC) and dust (Warren and Wiscombe, 1980; Flanner et al., 2007; Dang et al., 2015; Tuzet et al. 2017). However, in reality, snow grains are predominantly nonspherical, particularly for fresh snow (Erbe et al., 2003; Dominé

et al., 2003). Additionally, BC and dust can be mixed within snow grains (i.e., internal mixing) rather than the common assumption that BC and dust only exist outside snow grains (i.e., external mixing) (Flanner et al., 2012; He et al., 2019b). To accurately compute snow albedo with more realistic representations of snow grain shape and its interaction with LAPs, physics-based parameterizations have been developed that account for snow nonsphericity and snow-LAP internal mixing for applications in weather and climate models (e.g., Dang et al., 2016; Räisänen et al., 2017; He et al., 2017b, 2019b; Saito et al., 2019), revealing important impacts of these two factors (He, 2022). In addition, the size, shape, and composition of LAPs play a nontrivial role in snow-LAP-radiation interactions (Liou et al., 2014; He et al., 2018b, 2019b; Flanner et al., 2021; Pu et al., 2021; Shi et al. 2022). Moreover, in addition to the traditionally modeled LAPs, such as BC and dust, there is increasing attention on other types of LAPs including brown carbon (Yan et al., 2019; Liu et al., 2020; Li et al., 2021), snow algae (Cook et al., 2017; Williamson et al., 2020), and volcanic ash (Young et al., 2014; Flanner et al., 2014; Gelman Constantin et al., 2020).

The standalone version of SNICAR has been updated to include these more realistic and physical treatments of snow-LAP-radiation interactions (updated version is SNICAR-ADv3; Flanner et al., 2021), including updated ice and aerosol optics as well as downward solar spectra, incorporation of multiple dust types and nonspherical snow grains, and the use of a more accurate adding-doubling (AD) two-stream radiative transfer solver. The standalone SNICAR-ADv3 model does not include BC/dust-snow internal mixing but uses a coated BC particle treatment instead, which shows similar effects as with explicit BC-snow internal mixing (Flanner et al., 2021). Leveraging the SNICAR-ADv3 updates and other aforementioned new LAP-snow parameterizations, the E3SM/ELM model with SNICAR as its embedded snow albedo scheme has been updated to include snow nonsphericity, BC/dust-snow internal mixing, and the adding-doubling radiative transfer solver, which leads to improved simulations of snow surface energy and water balances (Hao et al., 2023).

In view of the scientific and modeling advances, it is imperative to enhance the CESM/CLM-SNICAR snow albedo modeling with more realistic and physical representations of snow-LAP-radiation interactions, considering the broad use of CESM/CLM (Lawrence et al., 2019). The default CLM uses the original SNICAR model developed 16 years ago (Flanner et al., 2007), which assumes spherical snow grains externally mixed with LAPs via a less accurate two-stream solver and outdated input databases for ice and aerosol optics and downward solar spectra.

These inadequate snow albedo treatments in CLM-SNICAR have been identified as a contributing factor to model biases in simulating surface albedo and snowpack evolution (e.g., Chen et al., 2014; Toure et al., 2018; Thackeray et al., 2019). Therefore, this study aims to improve the CLM-SNICAR snow albedo scheme by incorporating more realistic and physically-based representations of snow-LAP-radiation interactions.

This paper is organized as follows. Section 2 provides descriptions of model enhancements and simulations as well as observational datasets used for model evaluation. Section 3 investigates model sensitivities to each of the new features and enhancements implemented in this study. Section 4 presents evaluations of the updated model for key snow and surface fields. Section 5 concludes the study.

2. Model and data

2.1 CLM5 snow albedo scheme

We use the CLM version 5.0 (CLM5) in this study, which is the land component of CESM2. CLM5 represents a full suite of terrestrial biogeophysical and biogeochemical processes, including carbon and nitrogen cycles, vegetation dynamics for ecosystems, and land surface and subsurface energy and water processes. More details about CLM5 are provided in Lawrence et al. (2019). Since this study specifically focuses on snow albedo, we briefly summarize the key elements of the CLM5 snow albedo scheme below.

CLM5 includes the SNICAR model (Flanner et al., 2007) to compute snow albedo for the multi-layer (up to 12 layers) snowpack. It accounts for the effects of snow grain size (and hence snow aging) and LAP contamination on snow albedo. The original version of SNICAR leverages a multi-layer two-stream radiative transfer scheme based on Wiscombe and Warren (1980) and Toon et al. (1989). The required input variables for SNICAR include direct/diffuse radiation, surface downward solar spectrum, solar zenith angle (under direct radiation), ground albedo underlying snowpack, vertical distributions of snow grain size, snow layer thickness, snow density, and aerosol concentration, and optical properties of ice and aerosols. The ice and aerosol optical properties (single-scattering albedo, mass extinction cross-section, and asymmetry factor) are computed offline by Mie theory using particle refractive indices and size distributions, and are archived as look-up tables. The CLM5-SNICAR assumes snow spheres externally mixed with aerosols. The surface downward solar spectrum used in CLM5-SNICAR represents clear- or

cloudy-sky atmospheric conditions typical of mid-latitude winter. The CLM5-SNICAR computes snow albedo at 5 spectral bands (300-700 nm, 700-1000 nm, 1000-1200 nm, 1200-1500 nm, and 1500-5000 nm), which are then averaged to values at two broadbands (visible: 300-700 nm; near-infrared (NIR): 700-5000 nm) weighted by the downward solar spectrum. More detailed descriptions of CLM-SNICAR can be found in Flanner et al. (2007). Figure 1 summarizes the general workflow for the key elements in CLM5-SNICAR snow albedo calculations.

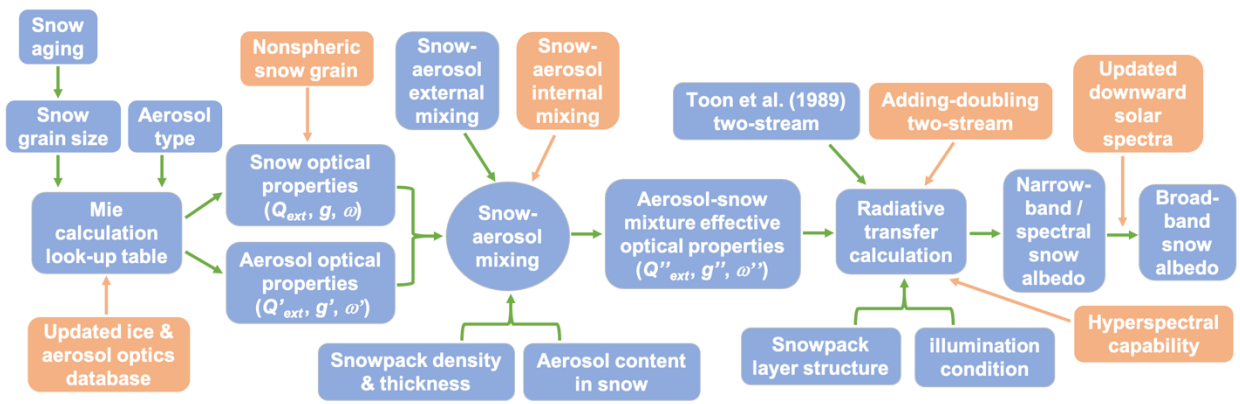

Figure 1. Workflow for key elements in CLM5-SNICAR snow albedo modeling. Blue boxes indicate the default model processes/capabilities. Orange boxes indicate the new model capabilities/enhancements implemented in this study. Q_{ext} is the mass extinction cross section, g is the asymmetry factor, and ω is the single-scattering albedo.

2.2 New features and enhancements in CLM5 snow albedo scheme

The standalone version of SNICAR has been recently updated to SNICAR-ADv3 by Flanner et al. (2021) with several new features as mentioned in Section 1. In addition, new parameterizations that account for BC-snow and dust-snow internal mixing have been recently developed. Thus, we combine all these recent updates that more physically and realistically represent snowpack characteristics in snow albedo computation, and implement them into CLM5-SNICAR (Table 1 and Figure 1). Particularly, we include these new features/enhancements as additional CLM5-SNICAR physics/namelist options, which offers an effective way to quantify model sensitivity to snow albedo processes and allows for relevant multi-physics model ensemble analyses for uncertainty evaluation.

Table 1. List of new features and enhancements in CLM-SNICAR snow albedo scheme implemented in this study

Features/enhancements	New schemes & namelist options (* for new baseline)	Original scheme
Ice optical properties: updates from Flanner et al. (2021), with multiple options for ice refractive indices	snicar_snw_optics = 1 (Warren, 1984) 2 (Warren and Brandt, 2008) 3* (Picard et al., 2016)	Warren (1984)
BC and OC optical properties: updates from Flanner et al. (2021)	Flanner et al. (2021)	Flanner et al. (2007)
Dust optical properties: updates from Flanner et al. (2021) with multiple dust types	snicar_dust_optics = 1* (Saharan dust) 2 (Colorado dust) 3 (Greenland dust)	Saharan dust (Flanner et al., 2007)
Downward solar spectra: updates from Flanner et al. (2021) for multiple atmospheric conditions	snicar_solarspec = 1* (mid-latitude winter) 2 (mid-latitude summer) 3 (sub-Arctic winter) 4 (sub-Arctic summer) 5 (Summit, Greenland) 6 (high mountain)	mid-latitude winter (Flanner et al., 2007)
Radiative transfer solver: new adding-doubling solver from Dang et al. (2019)	snicar_rt_solver = 1 (Toon et al. 1989) 2* (Adding-Doubling)	Toon et al. (1989)
Snow grain shape: nonspherical snow grains from He et al. (2017b)	snicar_snw_shape = 1 (sphere) 2 (spheroid) 3* (hexagonal) 4 (snowflake)	sphere
BC-snow mixing: internal mixing from He et al. (2017b)	snicar_snobc_intmix = true (internal mixing) false* (external mixing)	external mixing
Dust-snow mixing: internal mixing from He et al. (2019b)	snicar_snodst_intmix = true (internal mixing) false* (external mixing)	external mixing
Wavelength band: new hyperspectral (480-band, 10-nm spectral resolution) capability from Flanner et al. (2021)	snicar_numrad_snw = 5* (5-band) 480 (480-band)	5-band
New namelist controls for aerosol & OC	snicar_use_aerosol = true*, false DO_SNO_OC = true, false*	No namelist controls on using aerosol and OC (hard-coded)

2.2.1 Updated ice optical properties

The original CLM5-SNICAR uses the Warren (1984) compilation of ice refractive indices (RI) across the solar spectrum. Later, Warren and Brandt (2008) further updated the ice refractive indices data with much weaker absorption at wavelengths below 600 nm. However, more recent measurements by Picard et al. (2016) showed a larger ice absorption (i.e., the imaginary part of refractive indices) at 320-600 nm wavelengths than the Warren and Brandt (2008) data but smaller than the Warren (1984) data. This is consistent with the systematic snow albedo overestimate at wavelengths below 500 nm in SNICAR simulations using the Warren and Brandt (2008) data (He et al., 2018c). Thus, Flanner et al. (2021) updated the imaginary part of ice refractive indices by replacing the Warren and Brandt (2008) data with the Picard et al. (2016) data at wavelengths shorter than 600 nm. Flanner et al. (2021) also compiled another dataset for the imaginary part of ice refractive indices by merging the Warren (1984) and Perovich and Govoni (1991) datasets. These three datasets use the same Warren and Brandt (2008) compilation of the real part of refractive indices, and only differ in the imaginary part at wavelengths less than 600 nm, which is extremely challenging to measure accurately. Including all these three datasets in CLM5-SNICAR (i.e., ice optics namelist option "snicar_snw_optics" in Table 1) will allow uncertainty quantification. Following Flanner et al. (2021), we use the merged Picard et al. (2016) dataset as the new baseline model option in the updated CLM5-SNICAR.

Using the ice refractive indices, ice optical properties (i.e., single-scattering albedo, mass extinction cross-section, and asymmetry factor) are then computed by Mie theory based on various ice grain effective radii ranging from 30 to 1500 μm with lognormal size distributions (Flanner et al., 2021), and are archived as an input look-up table. The look-up table of ice optical properties created by Flanner et al. (2021) is for 480-band at 10-nm spectral (i.e., hyperspectral) resolution across the solar spectrum (200-5000 nm). To work with the 5 spectral bands in CLM5-SNICAR, we further use the spectral weighted averaging technique to convert the hyperspectral ice optical properties to the 5-band values following Flanner et al. (2007). For the new hyperspectral computation option added to CLM5-SNICAR (see Section 2.2.9), we directly use the 480-band ice optics dataset produced by Flanner et al. (2021).

2.2.2 Updated aerosol optical properties

The original CLM5-SNICAR accounts for three types of LAPs, including BC, OC (i.e., brown carbon), and dust (Saharan type), using the aerosol optics dataset developed by Flanner et al. (2007). Flanner et al. (2021) updated the optical properties for all three aerosol types using updated particle density, size distribution, and refractive indices via Mie theory calculations. Overall, the updated aerosol optical properties lead to a stronger light absorption for OC and Saharan dust but a weaker light absorption for BC. We implement the Flanner et al. (2021) dataset into CLM5-SNICAR and conduct the spectral weighted averaging to convert the hyperspectral (480-band) aerosol optical properties to the 5-band values following Flanner et al. (2007). For the new hyperspectral computation option (see Section 2.2.9), we directly use the 480-band aerosol optics dataset (Flanner et al., 2021). Given the substantial uncertainty in OC modeling due to a lack of observational constraints (Liu et al., 2020), we turn off the OC effect on snow albedo (namelist option "DO_SNO_OC" in Table 1) in our proposed new baseline model configuration, but we activate it in sensitivity simulations to test its impact (Section 3).

2.2.3 Updated dust types

The original CLM5-SNICAR only accounts for one dust type (i.e., Saharan dust; Flanner et al., 2007), while previous studies showed substantial differences in dust optical properties due to different particle size and composition for dust that originates from different regions (Scanza et al., 2015; Polashenski et al., 2015; Skiles et al., 2017). Thus, in addition to the Saharan dust (Scanza et al., 2015), Flanner et al. (2021) included two more dust types, Colorado dust (Skiles et al., 2017) and Greenland dust (Polashenski et al., 2015), which are added to the updated CLM5-SNICAR in this study. Overall, Greenland dust shows the strongest light absorbing ability, followed by Saharan dust, while Colorado dust has the weakest light absorbing capacity among the three (Flanner et al., 2021). Including different dust types in CLM5-SNICAR (i.e., dust optics namelist option "snicar_dust_optics" in Table 1) offers a way for uncertainty analysis. Following Flanner et al. (2021), we use the Saharan dust as the new baseline model option in the updated CLM5-SNICAR. We note that the updated model does not have the capability of simultaneously using multiple dust types over different regions in one single simulation. Ideally, the CLM5-SNICAR should be able to take the spatiotemporally varying aerosol optical properties (dust, BC, and OC) directly from the coupled atmospheric model component for consistent simulations, which will be improved in the future.

2.2.4 Updated surface downward solar spectra

The original CLM5-SNICAR uses the surface downward solar spectrum for clear-sky or cloudy-sky atmospheric conditions typical of mid-latitude winter (Flanner et al., 2007). In the model, the downward solar spectrum is used uniformly across the simulation domain to compute the spectrally-integrated broadband snow albedo from the spectral albedo derived from the radiative transfer solver. However, atmospheric conditions significantly affect the downward solar spectrum at the surface and therefore using only one downward solar spectrum may lead to nontrivial errors in simulated broadband snow albedo. Thus, Flanner et al. (2021) developed 5 additional downward solar spectra to represent clear-sky and cloudy-sky atmospheric conditions typical of mid-latitude summer, sub-Arctic winter, sub-Arctic summer, Summit Greenland, and high mountain environments. We implement these new downward solar spectra (i.e., solar spectrum namelist option "snicar_solarspec" in Table 1) into CLM5-SNICAR to offer more accurate albedo calculations for applications in those specific regions. Following Flanner et al. (2021), we use the mid-latitude winter spectrum as the new baseline model option in the updated CLM5-SNICAR. We note that the updated model does not have the capability of simultaneously using multiple solar spectra over different regions in one single simulation. Ideally, the CLM5-SNICAR should be able to take the spatiotemporally varying downward solar spectrum directly from the coupled atmospheric model component for consistent simulations. This is an important opportunity for further future improvement.

2.2.5 Updated radiative transfer solver

The original CLM5-SNICAR adopts the tri-diagonal matrix two-stream solver (Toon et al., 1989), which shows larger snow albedo biases (i.e., overestimates) particularly under diffuse conditions than an adding-doubling two-stream solution (Dang et al., 2019). Moreover, the adding-doubling solution has a stronger computational stability under different solar zenith angles and a higher computational efficiency than the tri-diagonal matrix solution. The adding-doubling solver also allows accounting for internal Fresnel layers in snow-ice interface, providing the potential for a unified snow-ice radiative transfer treatment. Because of these advantages, the adding-doubling solution has been implemented in the standalone SNICAR-ADv3 (Flanner et al., 2021) and the E3SM/ELM model (Hao et al., 2023). Following these recent studies, we implement the adding-

doubling solution into CLM5-SNICAR (i.e., radiative transfer namelist option "snicar_rt_solver" in Table 1), and use it as the new baseline model option in the updated CLM5-SNICAR, considering its higher computational accuracy, efficiency, and stability. Detailed descriptions of the adding-doubling formulation can be found in Dang et al. (2019).

2.2.6 Representation of snow nonsphericity

The original CLM5-SNICAR assumes spherical snow grains (Flanner et al., 2007), which however may not be a realistic representation since nonspherical snow grains are ubiquitous in reality (Erbe et al., 2003; Dominé et al., 2003). To quantify the impact of snow nonsphericity, He et al. (2017b) developed a set of snow optical parameterizations based on sophisticated geometric-optics ray-tracing calculations (Liou et al., 2014) for four typical snow grain shapes representative of real-world observations, including sphere, spheroid, hexagonal plate/column, and fractal snowflake (Figure 2). Snow grain shape mainly affects the snow asymmetry factor with very limited impact on extinction cross section and single-scattering albedo (Dang et al., 2016; He and Flanner, 2020). Thus, the He et al. (2017b) parameterizations make corrections to the asymmetry factor of snow spheres to account for nonsphericity effects based on grain shape, aspect ratio, effective radius, and wavelength. The parameterizations have been implemented into the standalone SNICAR-ADv3 (Flanner et al., 2021) and the E3SM/ELM model (Hao et al., 2023), which provide detailed descriptions of the associated formulation and implementation. Following these recent studies, we implement the same parameterizations for the four grain shapes into CLM5-SNICAR (i.e., snow shape namelist option "snicar_snw_shape" in Table 1). We set the hexagonal shape (one of the most common shapes for ice crystal) as the new baseline model option in the updated CLM5-SNICAR following Flanner et al. (2021).

We note that there are other parameterizations that account for nonspherical snow grains in albedo calculations, which have been used in other land/climate models (e.g., Libois et al., 2013; Räisänen et al., 2017; Saito et al., 2019). These studies all find that accounting for snow nonsphericity provides a more realistic representation of snow characteristics in albedo calculations. All of these models are limited by a lack of dynamic evolution of snow grain shapes, which is another opportunity for future model development. We note that in this study, the snow aging scheme that simulates the dynamic evolution of specific surface area (Flanner et al., 2007)

is the same as that in the default CLM-SNICAR. Thus, the snow nonsphericity effect analyzed here quantifies the impact of different grain shapes with equal specific surface area.

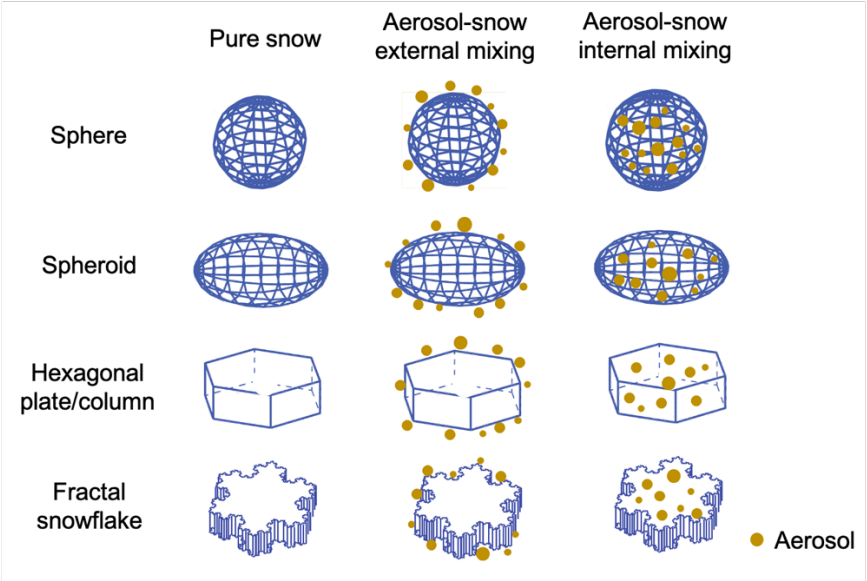

Figure 2. Demonstration of snow grains with four different shapes as well as aerosol-snow external and internal mixing states that are implemented in this study.

2.2.7 Representation of BC-snow internal mixing

The original CLM5-SNICAR assumes BC-snow external mixing, whereas previous studies pointed out that BC can also be internally mixed with snow grains (Figure 2), through a number of BC-cloud-precipitation interaction processes, which strongly enhances BC-induced snow albedo reduction (Flanner et al., 2012; Liou et al., 2014; He et al., 2017b). He et al. (2017b) developed a parameterization to account for BC-snow internal mixing in snow albedo calculations, where the internal mixing mainly affects the single-scattering albedo of BC-snow mixtures with negligible impacts on snow asymmetry factor and extinction cross section. This parameterization was developed based on sophisticated geometric-optics ray-tracing calculations and computes the change of snow single-scattering albedo caused by BC-snow internal mixing as a function of BC particle effective radius and concentration in snow. This parameterization was implemented into an earlier version of SNICARv2 (He et al., 2018c), which describes the formulation and implementation in detail. Following this study, we implement the BC-snow internal mixing parameterization into CLM5-SNICAR (i.e., BC-snow mixing namelist option

"snicar_snobc_intmix" in Table 1). We note that there is a lack of observational constraints for BC-snow mixing state (internal versus external) and there is also substantial uncertainty in modeling the evolution of BC-snow mixing state, therefore we maintain the BC-snow external mixing as the new baseline model option in the updated CLM5-SNICAR, but we activate the internal mixing in sensitivity simulations to test its impact (Section 3).

There are other methods developed to account for the effect of BC-snow internal mixing, such as the look-up table method developed based on a dynamic effective medium approximation in Flanner et al. (2012), which has been adopted by E3SM/ELM-SNICAR (Hao et al., 2023). He et al. (2018c) showed that the He et al. (2017b) parameterization of BC-snow internal mixing leads to consistent snow albedo reductions with the results computed from the Flanner et al. (2012) look-up tables. More observations of BC-snow mixing state are needed to constrain models to achieve more accurate estimates of BC-induced snow albedo changes.

2.2.8 Representation of dust-snow internal mixing

Similar to the BC-snow mixing treatment, the original CLM5-SNICAR assumes dust-snow external mixing. However, previous studies found that dust can also be mixed internally with snow grains (Figure 2) via dust-cloud-precipitation interactions, which enhances dust-induced snow albedo reduction (He et al., 2019b; Shi et al., 2021). To quantify the impact of dust-snow internal mixing, He et al. (2019b) developed a parameterization that nonlinearly connects internal mixing-induced changes of snow single-scattering albedo to dust concentration in snow based on sophisticated geometric-optics ray-tracing calculations. The dust-snow internal mixing has negligible effects on the snow asymmetry factor and extinction cross section. The He et al. (2019b) parameterization was implemented into E3SM/ELM-SNICAR (Hao et al., 2023). In the present study, we implement the dust-snow internal mixing parameterization into CLM5-SNICAR (i.e., dust-snow mixing namelist option "snicar_snodst_intmix" in Table 1). Similar to BC-snow mixing, there is also a lack of observational constraints for dust-snow mixing state and large model uncertainty for the mixing state evolution. Thus, we maintain the dust-snow external mixing as the new baseline model option in the updated CLM5-SNICAR, but we activate the internal mixing in sensitivity simulations to test its impact (Section 3). We note that the He et al. (2019b) parameterization of dust-snow internal mixing was developed without the presence of internally

mixed BC, so we suggest not activating BC-snow and dust-snow internal mixing simultaneously in CLM5-SNICAR.

Recently, Shi et al. (2021) used another method (i.e., the effective medium approximation) to account for dust-snow internal mixing in snow albedo modeling, which shows generally consistent results with those derived from the He et al. (2019b) parameterization. In the future, more observations of dust-snow mixing state are needed to better constrain modeled dust impacts on snow albedo.

2.2.9 New hyperspectral computation capability

The original CLM5-SNICAR uses 5 spectral bands (300-700 nm, 700-1000 nm, 1000-1200 nm, 1200-1500 nm, and 1500-5000 nm) in radiative transfer calculations to increase computational efficiency. Accordingly, the ice and aerosol optical properties and downward solar spectra in input datasets are all spectrally averaged into the 5 bands. However, a recent study (Wang et al., 2022) found that because of the nonlinearity of radiative transfer computation, using the 5 spectral bands in SNICAR leads to a nontrivial snow albedo bias (up to 0.05) compared to hyperspectral (10-nm spectral resolution) calculations. Thus, we implement a hyperspectral (10-nm spectral resolution with 480 bands) computation capability into CLM5-SNICAR in this study, similar to that used by the standalone SNICAR-ADv3 model. The hyperspectral modeling capability includes all the new features and enhancements mentioned in Sections 2.2.1-2.2.8. The addition of this hyperspectral capability particularly targets on local/regional process-level investigations that require higher snow albedo accuracy, because it is much more computationally expensive than the 5-band calculations (e.g., 8 times slower for global 1-deg 10-year simulations in this study using the configuration described in Section 2.3). However, as computational power increases, the use of this hyperspectral capability in global or high-resolution modeling will become more feasible.

2.3 Model simulations

To assess the model sensitivities and performance with the aforementioned new features and enhancements, we conduct a series of global 1-deg land-only CLM5-SNICAR simulations driven by the atmospheric forcing from the 3-hourly 0.5° Global Soil Wetness Project Phase 3 dataset (GSWP3; Dirmeyer et al., 2006), which has been widely used and evaluated by previous studies (e.g., Lawrence et al., 2019; Hao et al., 2023). All model simulations use the prescribed

monthly climatological MODIS satellite phenology mode (i.e., CLM configuration/compset: I2000Clm51Sp) (Lawrence et al., 2019), and the prescribed monthly aerosol (BC, dust, OC) wet and dry deposition flux from the CESM2-WACCM simulations participated in CMIP6 experiments (Danabasoglu et al., 2020).

Model experiments include a default baseline simulation using the original CLM5-SNICAR (hereinafter "default baseline"), a new baseline simulation using the enhanced CLM5-SNICAR (hereinafter "new baseline") with the new baseline physics option identified above and in Table 1, and a set of twin sensitivity simulations by turning on and off each new feature/enhancement (Table 1) at a time with the same baseline setup for other snow physics options in order to quantify the impact of the targeted feature/enhancement. The aerosol-induced snow albedo radiative forcing analyzed in this study is based on the instantaneous ground net radiative flux difference through double calls of SNICAR with and without specific aerosol species. We spin up the model simulations for the years 2000-2005 and use the 2006-2010 period for analysis. For seasonal analysis, we define each season as winter (December-January-February), spring (March-April-May), summer (June-July-August), and fall (September-October-November).

2.4 Data for model evaluation

To evaluate the default and new baseline model simulations of snow albedo and other snowpack properties, global spatiotemporally continuous observation-based datasets are preferred. Thus, we use the daily 0.05° MODIS data for snow cover fraction (MOD10C1 and MYD10C1) and surface albedo (MCD43C3) as well as the monthly 0.1° ERA-5 land reanalysis data for snow water equivalent (SWE), snow depth, and surface 2-m temperature. The MODIS MCD43C3 product is an Aqua-Terra merged surface albedo dataset and we use the data with quality flag of 0-2 (i.e., "ok", "good", and "best") to achieve a balance between enough samples and data quality, following He et al. (2019a). We use the MODIS snow cover data with quality flag of 0 and 1 (i.e., "good" and "best") and cloud fraction of <20% (more clouds lead to degraded data accuracy) to achieve a balance between enough samples and data quality, following He et al. (2019a). We further merge the Aqua (MYD10C1) and Terra (MOD10C1) MODIS snow cover data to obtain more complete global maps by replacing the data gaps in MOD10C1 with valid values (if existing) from MYD10C1 or averaging the pixel values if both MOD10C1 and MYD10C1 have valid data. To compare with model simulations at consistent spatial grids, we re-map the MODIS and ERA-

5 data to the model grids by averaging the values across the MODIS 0.05° pixels and ERA-5 0.1° pixels that are within each of the model 1° grids, respectively.

3. Model sensitivities to new features/enhancements

3.1 Effects of updated ice optics

Figure 3 shows the all-sky annual mean effects of updated ice optical properties on global snow albedo by using the Picard et al. (2016) versus Warren and Brandt (2008) ice refractive indices. Because the two datasets mainly differ at the visible band, there are negligible impacts on the NIR albedo. For the visible snow albedo, the differences are also small (<0.003) with slightly lower albedo using the Picard et al. (2016) data mainly over two polar regions under diffuse radiation (Figures 3 and S1). This is because the Picard et al. (2016) data leads to a stronger visible ice absorption (Flanner et al., 2021). Although the impact of using the Picard et al. (2016) data is small, it appears to more accurately capture the ice absorption in the visible band (He et al., 2018c; Flanner et al., 2021) and hence is recommended to use in future studies.

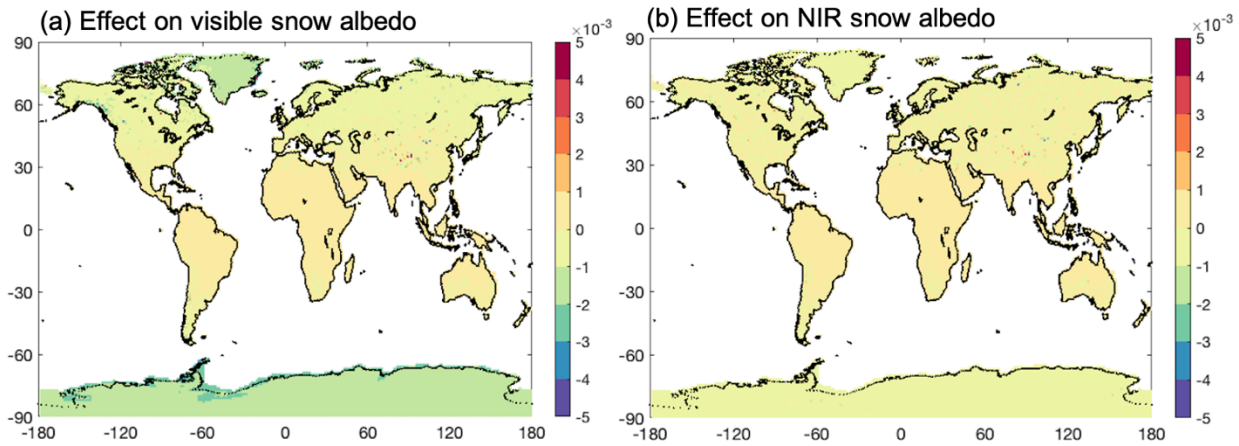

Figure 3. 5-year (2006-2010) all-sky annual mean effects of updated ice optical properties (i.e., differences between simulations using the Picard et al. (2016) and Warren and Brandt (2008) ice refractive indices): (a) difference for visible snow albedo, (b) difference for NIR snow albedo.

3.2 Effects of updated aerosol optics

Figure 4 shows the all-sky annual mean effects of updated aerosol (BC, OC, and Saharan dust) optical properties from the Flanner et al. (2021) data versus the Flanner et al. (2007) data on

snow-covered ground albedo and corresponding aerosol-induced snow albedo radiative forcing. Compared to using the Flanner et al. (2007) aerosol optics, the total aerosol-induced snow-covered ground albedo reduction using the Flanner et al. (2021) data is enhanced by up to 0.02 mainly over northern mid-latitudes (Figure 4a). This is primarily driven by stronger dust and OC light absorption using the Flanner et al. (2021) data relative to the Flanner et al. (2007) data, which further leads to stronger induced snow albedo forcing (Figures 4c, d) by up to >2.0 W m^{-2} (dust and OC combined) over heavily polluted hotspots, by ~0.17 W m^{-2} averaged over Northern Hemisphere, and by ~0.09 W m^{-2} globally. We note that the largely enhanced OC albedo forcing is due to the use of relatively strong-absorbing brown carbon optics in Flanner et al. (2021), which may not be representative of all OC or brown carbon. The enhanced snow albedo forcing caused by dust and OC is partially offset by the weaker BC light absorption with the BC forcing reduced by about 0.03 W m^{-2} averaged over Northern Hemisphere and 0.01 W m^{-2} globally (Figure 4b). The differences caused by updated aerosol optics mainly occur over northern mid-latitudes during winter and spring, and northern high-latitudes during spring and summer (Figure S2).

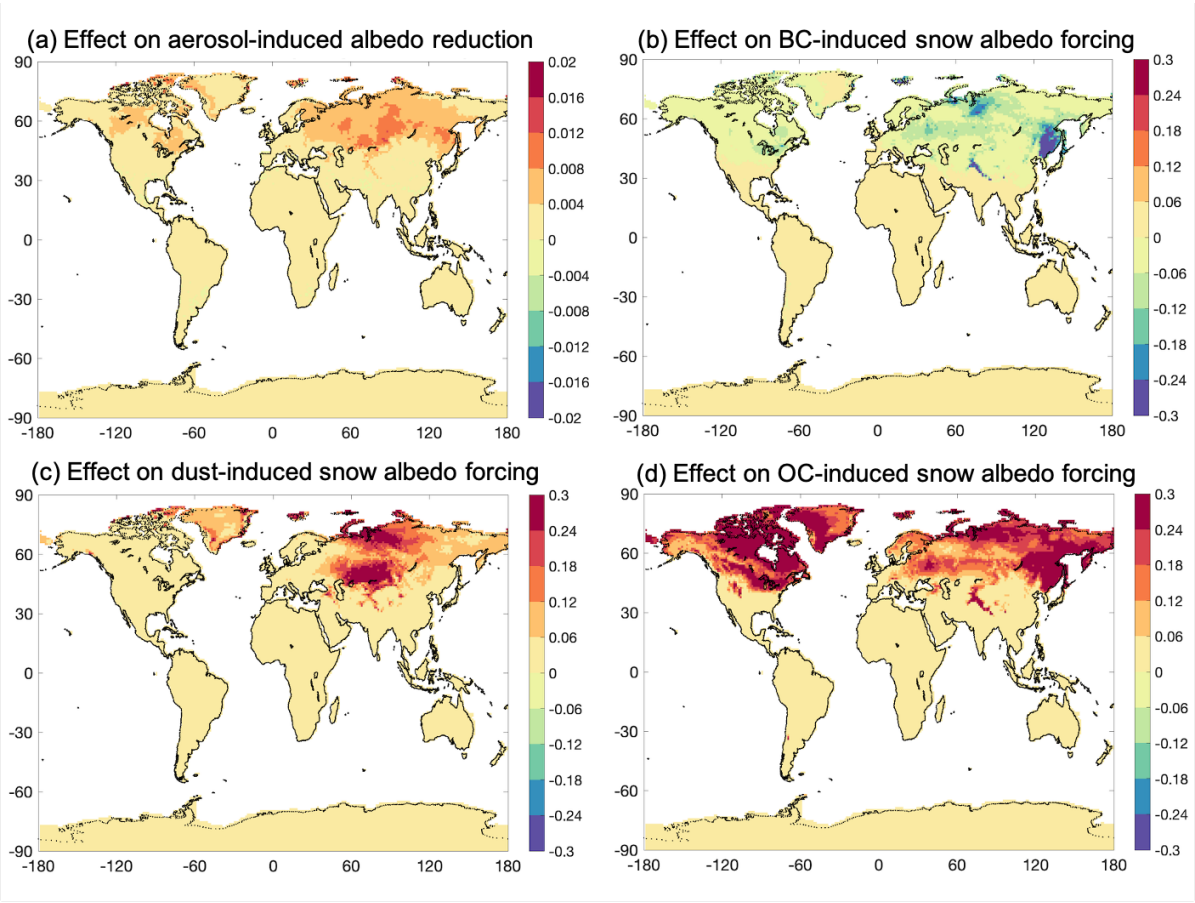

Figure 4. 5-year (2006-2010) all-sky annual mean effects of updated aerosol optical properties (i.e., differences between simulations using the Flanner et al. (2021) and Flanner et al. (2007) data): (a) difference for snow-covered ground albedo reduction caused by all aerosols, (b) difference for BC-induced snow albedo forcing (W m^{-2}), (c) difference for dust-induced snow albedo forcing (W m^{-2}), (d) difference for OC-induced snow albedo forcing (W m^{-2}).

3.3 Effects of different dust types

Figure 5 shows the all-sky annual mean differences between simulations using Greenland dust and Colorado dust in snow-covered ground albedo reduction and snow albedo forcing caused by dust. These two types of dust show the largest difference in light absorption capabilities among all the three dust types in the model (Section 2.2.3), which demonstrates the upper limit of model sensitivity to dust types in CLM5. Overall, using Greenland dust shows stronger albedo reduction by up to 0.02 mainly over northern Eurasia during winter and spring (Figures 5a and S3), compared to using Colorado dust. The corresponding annual difference in dust-induced snow albedo forcing reaches more than 3 W m^{-2} over polluted hotspots, with ~0.1 W m^{-2} averaged over Northern Hemisphere and ~0.05 W m^{-2} globally. Seasonally, the differences in snow albedo forcing mainly locate in northern mid-latitudes during winter and spring, and northern high-latitudes during spring and summer (Figure S5).

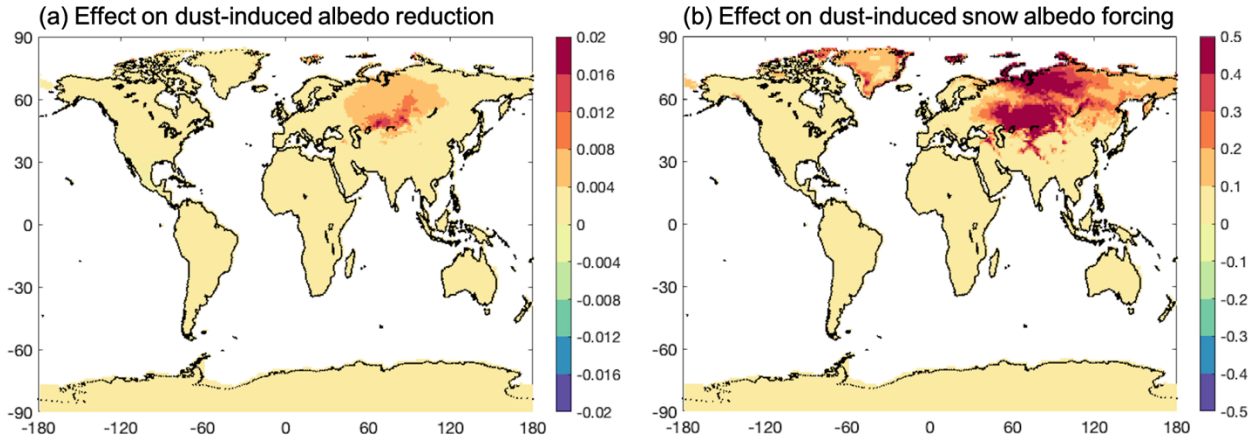

Figure 5. 5-year (2006-2010) all-sky annual mean effects of different dust types (i.e., differences between simulations using Greenland dust and Colorado dust): (a) difference for snow-covered

ground albedo reduction caused by dust, (b) difference for dust-induced snow albedo forcing (W m^{-2}).

3.4 Effects of updated downward solar spectra

Figure 6 shows the 5-year annual mean effects of downward solar spectra on snow albedo by using the high mountain spectrum versus the mid-latitude summer spectrum. These two spectra have the largest difference in energy distribution in the CLM5 spectral bands particularly for direct radiation (Figure S5), which demonstrates the upper limit of model sensitivity to downward solar spectra. Specifically, the snow albedo difference (by up to -0.04) between using the two spectra primarily occurs in the NIR band under direct radiation (Figure 5c), particularly over high latitudes with a mean difference of -0.02. The impact is minimal in the visible band or diffuse NIR band (Figures 5a, b, d).

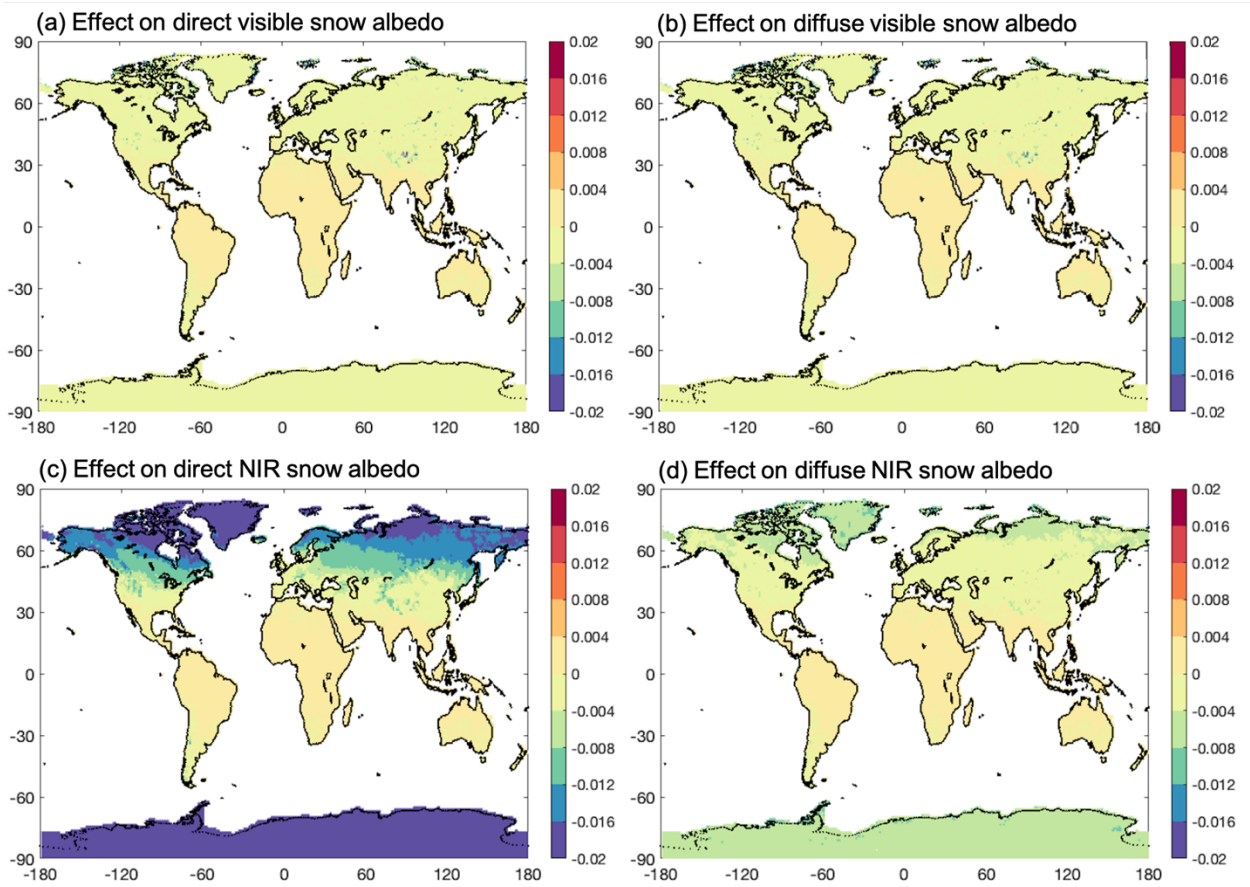

Figure 6. 5-year (2006-2010) annual mean effects of different downward solar spectra (i.e., differences between simulations using high mountain and mid-latitude summer spectra): (a)

difference for direct-beam visible snow albedo, (b) difference for diffuse visible snow albedo, (c) difference for direct-beam NIR snow albedo, (d) difference for diffuse NIR snow albedo.

3.5 Effects of updated radiative transfer solver

Figure 7 shows the 5-year annual mean snow albedo difference between simulations using the adding-doubling and Toon et al. (1989) radiative transfer solvers. The differences are negligible for the visible band but are significant (up to 0.04) for the NIR band under both direct and diffuse radiation. Specifically, using the adding-doubling solver leads to higher snow albedo under NIR direct radiation particularly in high-latitudes with a mean difference of 0.02 (Figure 7c), whereas it leads to a lower snow albedo under NIR diffuse radiation particularly in high-latitudes with a mean difference of -0.02 (Figure 7d). These difference patterns are similar across all the seasons with relatively larger differences in winter and spring (Figure S6). These results are consistent with the findings of Dang et al. (2019), where the adding-doubling solver has a similarly high accuracy as the Toon et al. (1989) solver for the visible band but substantially reduces the albedo underestimates at solar zenith angle >75° under NIR direct radiation and the albedo overestimates under NIR diffuse radiation caused by the Toon et al. (1989) solver. Thus, using the adding-doubling solver results in higher accuracy in snow albedo calculations.

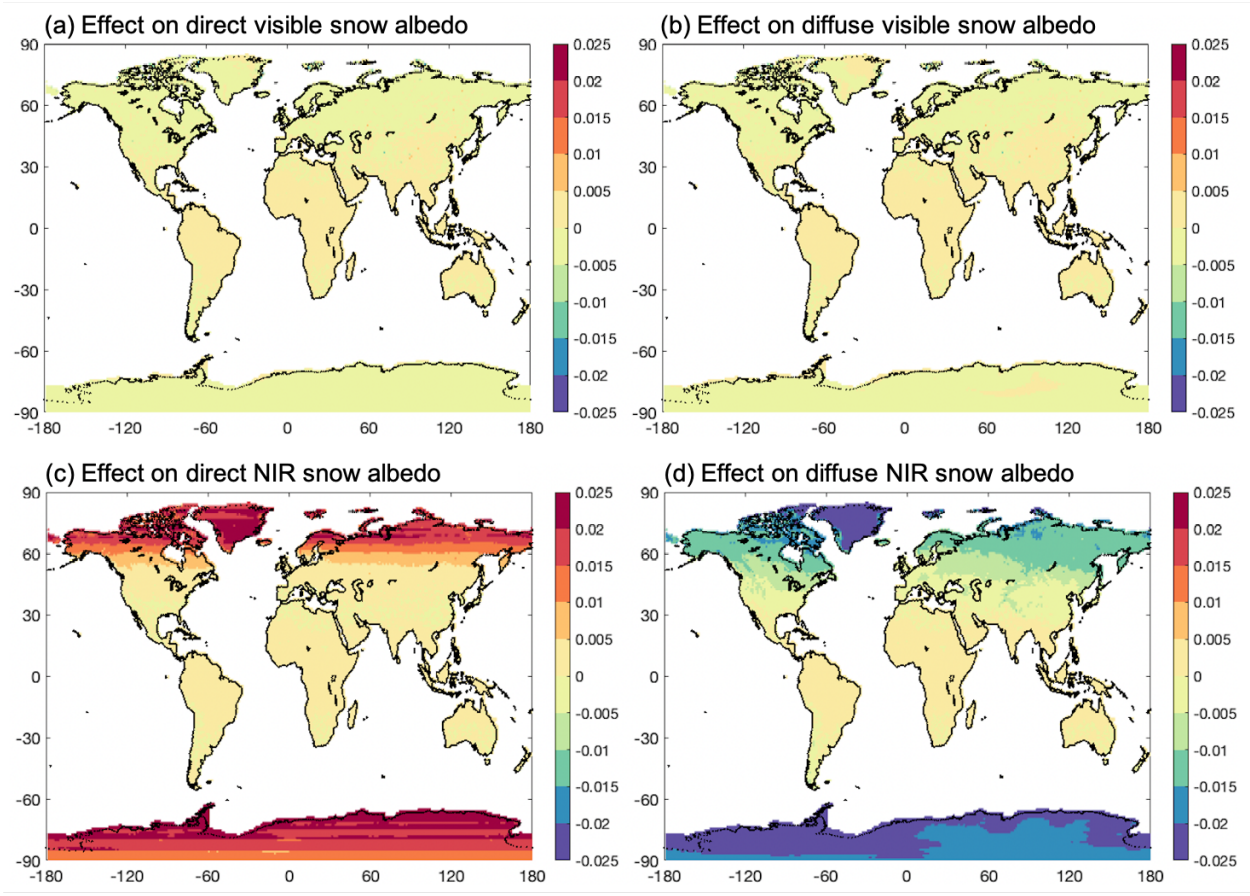

Figure 7. 5-year (2006-2010) annual mean effects of updated snow radiative transfer solvers (i.e., differences between simulations using the adding-doubling and Toon et al. (1989) solvers): (a) difference for direct-beam visible snow albedo, (b) difference for diffuse visible snow albedo, (c) difference for direct-beam NIR snow albedo, (d) difference for diffuse NIR snow albedo.

3.6 Effects of nonspherical snow grains

Figure 8 shows the 5-year all-sky annual mean effects of nonspherical snow grains on snow albedo and aerosol-induced snow albedo forcing by using fractal snowflakes versus snow spheres. These two grain shapes have the largest difference in snow optical properties, which demonstrates the upper limit of model sensitivity to snow nonsphericity in CLM5. Compared to using snow spheres, using fractal snowflakes leads to substantially higher snow albedo by more than 0.05 over some hotspots and ~0.015 globally, with a stronger impact over high-latitudes (Figure 8a). Seasonally, the albedo increase due to the use of fractal snowflakes are strongest in winter and spring over northern mid-latitudes and two polar regions (Figure S7). This is consistent with the conclusions from previous studies (Dang et al., 2016; Räisänen et al. 2017; He et al., 2018a), where

nonspherical snow grains have lower asymmetry factor (i.e., weaker forward scattering) and hence higher snow albedo by 0.02-0.05 on average, depending on specific grain shape, grain size, and snow density and thickness.

In addition, previous studies (He et al., 2018a, 2019; Shi et al., 2022) also found that nonspherical snow grains can reduce aerosol-induced snow albedo forcing because of the reduced forward scattering and hence less aerosol absorption throughout the snowpack column. This is confirmed by the results in this study, where using fractal snowflakes shows lower snow albedo forcing for BC, dust, and OC by up to 0.3 W m^{-2} or more, compared to using snow spheres (Figures 8b-d).

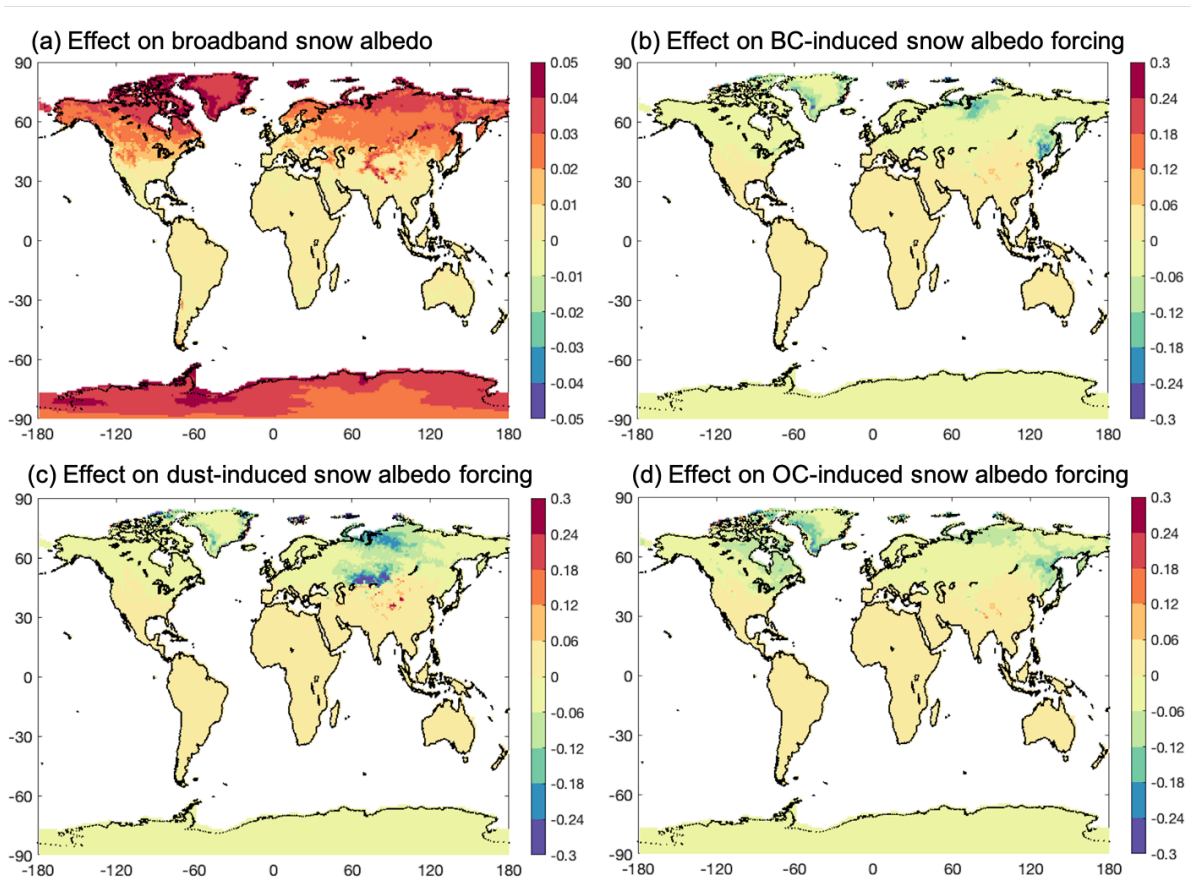

Figure 8. 5-year (2006-2010) all-sky annual mean effects of nonspherical snow grain (i.e., differences between simulations using fractal snowflake and snow sphere): (a) difference for broadband snow albedo, (b) difference for BC-induced snow albedo forcing (W m^{-2}), (c) difference for dust-induced snow albedo forcing (W m^{-2}), (d) difference for OC-induced snow albedo forcing (W m^{-2}).

3.7 Effects of BC-snow internal mixing

Figures 9a-b show the 5-year all-sky annual mean effects of BC-snow internal mixing on BC-induced snow albedo reduction and albedo forcing, compared to external mixing. Overall, the internal mixing significantly enhances BC-induced snow albedo reduction by up to 0.042 and albedo forcing by up to 1.0 W m^{-2} or more, with main effects over northern mid- and high-latitudes during winter and spring (Figure S8). This is consistent with previous studies (Flanner et al., 2012; He, 2022), where the snow albedo reduction caused by internal mixing can be enhanced by up to 0.05 or more relative to external mixing, depending on snow grain size and shape, snowpack density and thickness, BC concentration in snow, and illumination conditions. He et al. (2018a) further found that the enhanced albedo reduction due to internal mixing increases the BC-induced snow albedo forcing by up to 1 W m^{-2} in polluted regions like northern China snowpack, which agrees with the results in this study (Figure 9b).

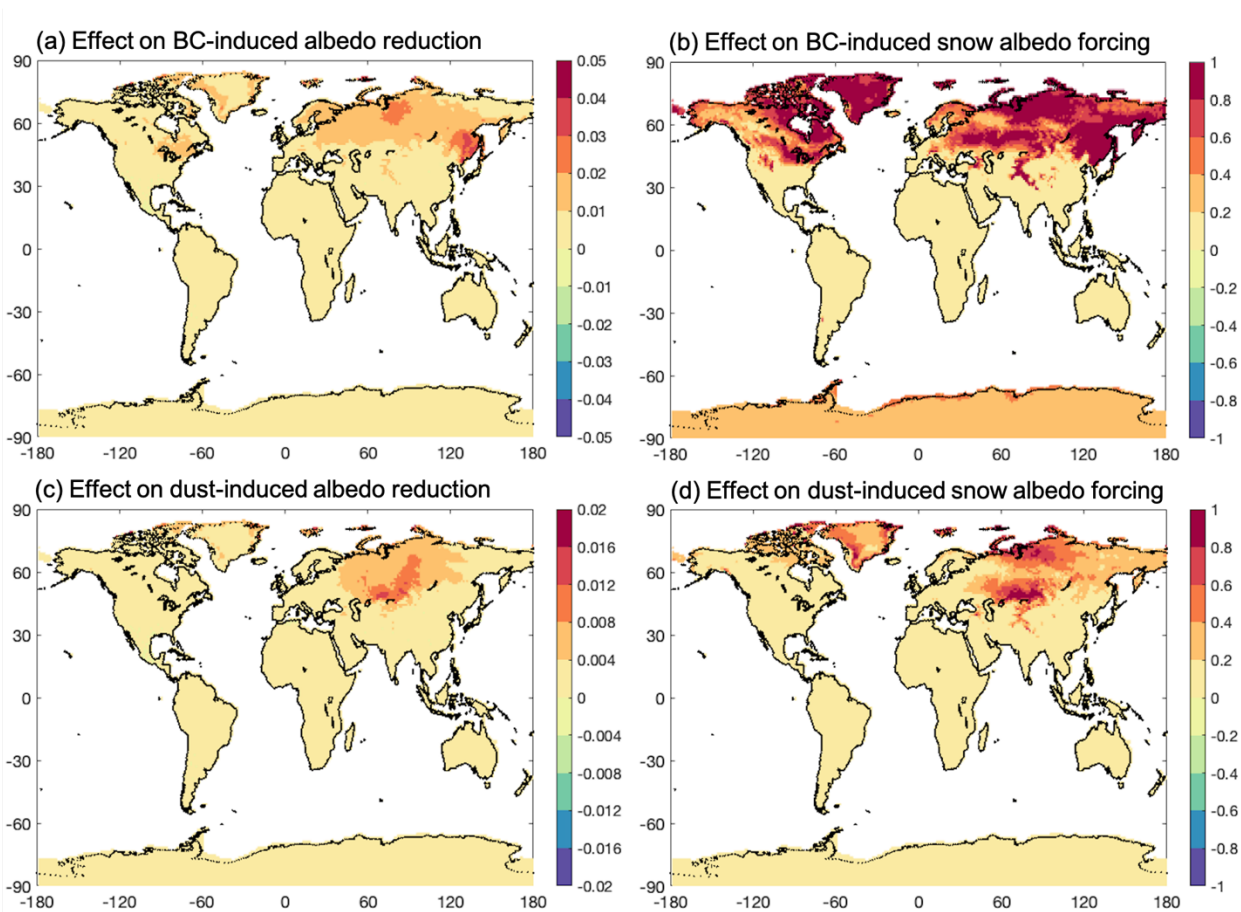

Figure 9. 5-year (2006-2010) all-sky annual mean effects of aerosol-snow internal mixing (i.e., differences between simulations using internal mixing and external mixing): (a) BC-snow internal mixing impact on BC-induced snow-covered ground albedo reduction, (b) BC-snow internal mixing impact on BC-induced snow albedo forcing (W m^{-2}), (c) dust-snow internal mixing impact on dust-induced snow-covered ground albedo reduction, (b) dust-snow internal mixing impact on dust-induced snow albedo forcing (W m^{-2}).

3.8 Effects of dust-snow internal mixing

Figures 9c-d show the 5-year all-sky annual mean effects of dust-snow internal mixing on dust-induced snow albedo reduction and albedo forcing, compared to external mixing. Similar to BC-snow internal mixing, the dust-snow internal mixing enhances snow albedo reduction by up to 0.02 and albedo forcing by up to 1.0 W m^{-2} or more, with major impacts over northern Eurasia during winter and spring as well as in the coasts of Greenland during summer (Figures 9c-d and S9). This is consistent with previous findings (He et al., 2019b; Shi et al., 2021, 2022), where dust-snow internal mixing can result in 10-45% enhancement in dust-induced snow albedo reduction and albedo forcing relative to external mixing, depending on snow grain size and shape, snowpack density and thickness, dust content in snow, and illumination conditions.

3.9 Effects of new hyperspectral capability

Figure 10 shows the 5-year annual mean difference in snow albedo between simulations using hyperspectral (480-band) and 5-band calculations. Overall, the differences in visible and NIR snow albedo under direct radiation are small (within ~0.004), while the hyperspectral calculation leads to noticeably higher visible and NIR albedo under diffuse radiation by up to >0.02 over some hotspots and 0.01-0.02 over most of two polar regions, compared to the 5-band calculations. This is consistent with the analysis of Wang et al. (2022), where the hyperspectral SNICAR calculations tend to have higher snow albedo than the 5-band SNICAR calculations. In addition, the hyperspectral calculation also results in nontrivial differences in aerosol-induced snow albedo forcing (Figure 11), with higher BC forcing (by up to 0.1 W m^{-2} over northern China and Himalayas) and OC forcing (by up to 0.2 W m^{-2} over northern high-latitudes) but lower dust forcing (by up to >0.1 W m^{-2} over northern Eurasia hotspots) compared to the 5-band calculations.

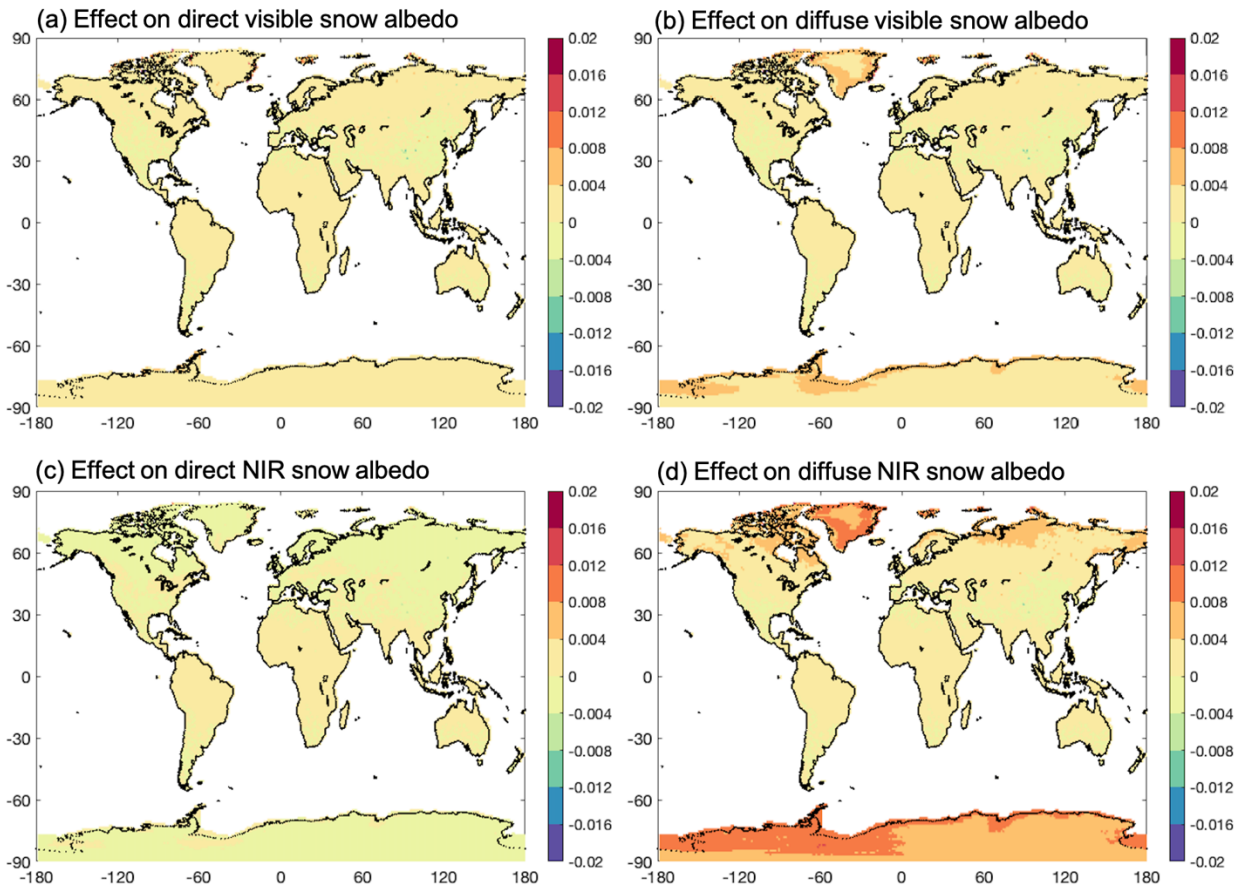

Figure 10. 5-year (2006-2010) annual mean effects of hyperspectral calculations (i.e., differences between simulations using 480 bands and 5 bands): (a) difference for direct-beam visible snow albedo, (b) difference for diffuse visible snow albedo, (c) difference for direct-beam NIR snow albedo, (d) difference for diffuse NIR snow albedo.

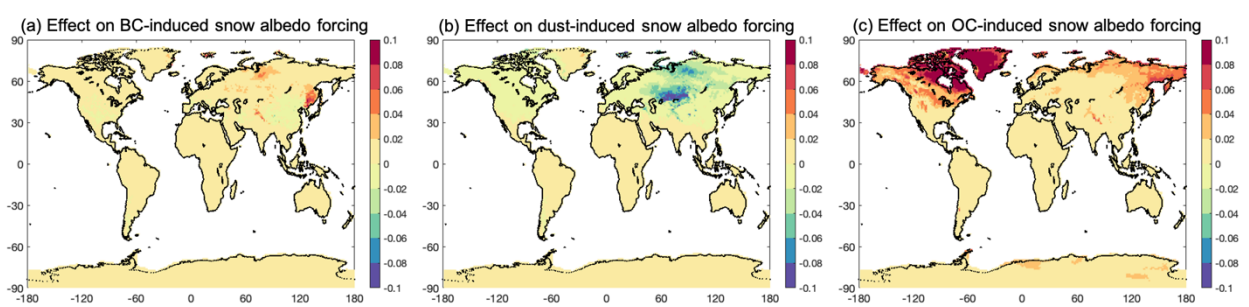

Figure 11. 5-year (2006-2010) all-sky annual mean effects of hyperspectral calculations (i.e., differences between simulations using 480 bands and 5 bands) on aerosol-induced snow albedo forcing (W m^{-2}): (a) difference for BC, (b) difference for dust, (c) difference for OC.

4. Model evaluation

Table 2. Summary of model evaluation statistics

Land surface fields	Model mean biases							
	Northern mid-latitudes (30°N-60°N)		Northern high-latitudes (60°N-90°N)		Southern mid-latitudes (30°S-60°S)		Southern high-latitudes (60°S-90°S)	
	default baseline	new baseline	default baseline	new baseline	default baseline	new baseline	default baseline	new baseline
Surface albedo (100% snow cover)	-0.022	0.004	-0.017	0.007	-0.022	0.005	0.003	0.034
Snow cover	-0.011	-0.009	-0.007	-0.004	-0.025	-0.019	-0.017	-0.012
SWE (mm)	-232.5	-178.3	-77.5	-63.4	-79.7	-64.8	-178.2	-174.0
Snow depth (m)	-2.53	-2.36	-0.67	-0.63	-1.56	-1.51	-5.12	-5.01
2-m temperature (°C)	1.32	1.26	0.53	0.47	0.62	0.55	2.35	2.26

4.1 Surface albedo

Figure 12 shows the comparison between MODIS observed and CLM5 simulated 5-year annual mean white-sky (diffuse) surface albedo over regions with 100% snow cover. The default baseline simulation tends to overestimate visible and NIR snow surface albedo in many parts of northern high-latitudes by about 0.1-0.2, but significantly underestimates the albedo in the northern mid-latitudes by up to 0.5 for the visible band and up to 0.3 for the NIR band, particularly over mountainous regions (Figures 12b, d). Compared to the default baseline result, the new baseline simulation with CLM5-SNICAR enhancements substantially reduces the albedo underestimate in the northern mid-latitudes by up to 0.1 for both visible and NIR bands (Figures 12c, f), primarily due to the use of nonspherical snow grains. The new baseline simulation also increases the snow surface albedo in northern and southern high-latitudes by up to 0.1 mainly at the NIR band, which however exacerbates the model bias in southern high-latitudes. These patterns are generally consistent throughout different seasons (Figures S10 and S11). The assessment for black-sky snow surface albedo shows similar results and conclusions (Figure S12). Table 2 summarizes the mean bias of the default and new baseline simulations. Overall, the new baseline simulation reduces the mean biases of fully snow-covered surface albedo over northern mid- and high-latitudes and southern mid-latitudes but increases the mean bias in southern high-latitudes.

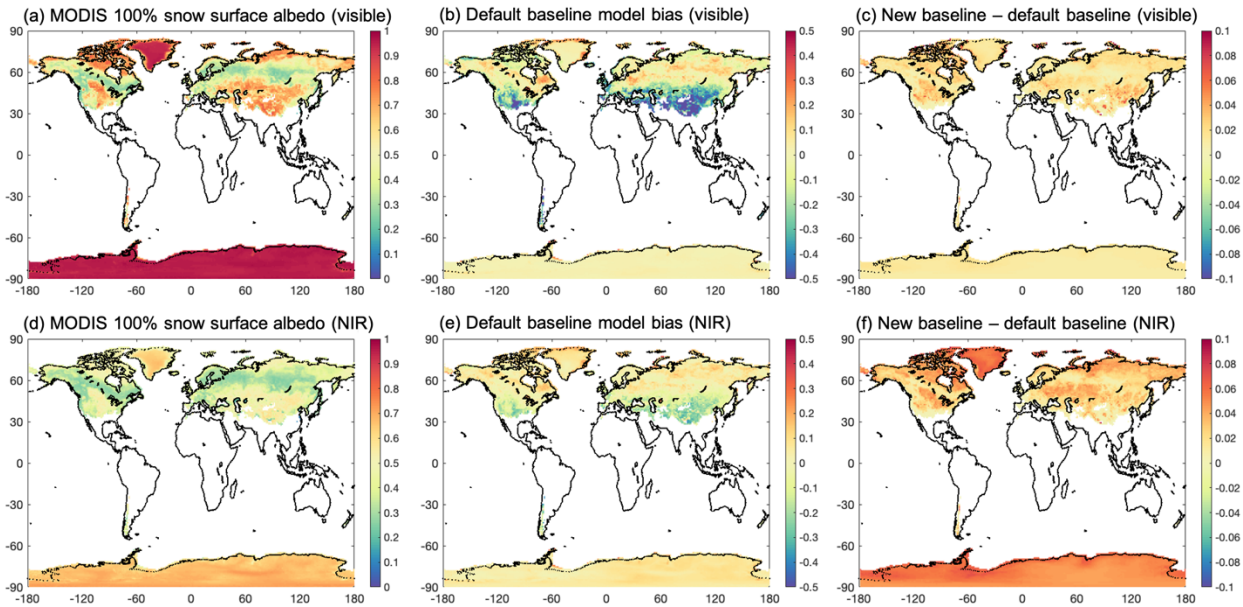

Figure 12. Comparison between MODIS and model simulations of 5-year (2006-2010) annual mean white-sky surface albedo for 100% snow cover grids. First column (a, d): MODIS observations; second column (b, e): default baseline simulation bias; third column (c, f): difference between new and default baseline simulations. First row (a, b, c): visible band; second row (d, e, f): NIR band.

4.2 Snow cover

Figures 13 and S13 shows the comparison between MODIS observed and CLM5 simulated 5-year seasonal mean snow cover fraction. The default baseline simulation significantly underestimates snow cover in the Tibetan Plateau and North American Rocky Mountains across all seasons by about 0.25, with patchy underestimates or overestimates in northern high-latitudes. Compared to the default baseline result, the new baseline simulation reduces the snow cover bias by up to 0.1 in the Tibetan Plateau and North American Rocky Mountains mainly during winter and spring, in many parts of northern Eurasia during spring and summer, and in the southern Andes during summer and fall. This is primarily caused by the increased snow albedo over those regions in the new baseline simulation (Section 4.1), which reduces the solar radiation absorbed by snowpack and hence increases snow cover. Overall, the new baseline simulation reduces the mean

snow cover biases (underestimates) across northern and southern mid- and high-latitudes (Table 2).

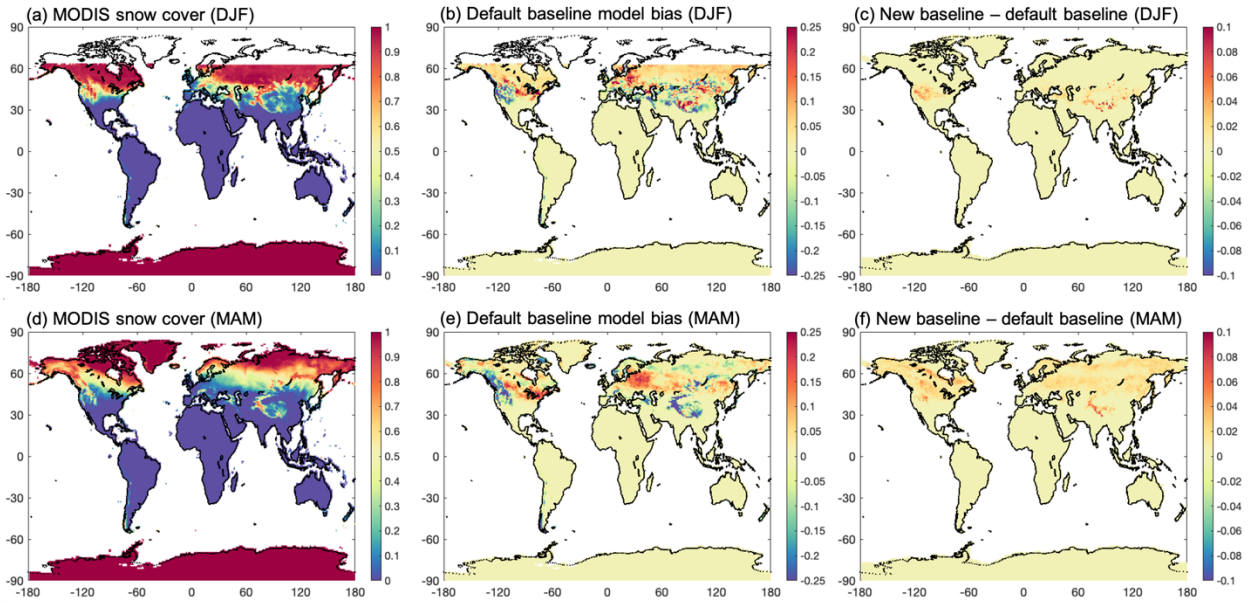

Figure 13. Comparison between MODIS and model simulations of 5-year (2006-2010) seasonal mean snow cover fraction. First column (a, d): MODIS observations; second column (b, e): default baseline simulation bias; third column (c, f): difference between new and default baseline simulations. First row (a, b, c): winter (December-January-February); second row (d, e, f): spring (March-April-May). See Figure S13 for results in summer (June-July-August) and fall (September-October-November) with relatively smaller effects from the new baseline simulation.

4.3 Snow water equivalent

Figures 14 and S14 shows the comparison between ERA-5 and CLM5 simulated 5-year seasonal mean snow water equivalent (SWE). We note that the maximum SWE allowed (i.e., SWE capping) in the CLM5 is set to 10,000 kg/m^2 to prevent unlimited snow building up over glacier regions in model simulations (particularly a coupled climate run), which would cause serious model issues (e.g., incorrect land water storage and ocean salinity). Thus, when evaluating simulated SWE, we screened out the regions with model SWE capping at 10,000 kg/m^2 (mainly Greenland and Antarctic ice sheets), because it is not meaningful to compare the model results with snow capping and the ERA-5 results without SWE capping in those regions.

The default baseline simulation systematically underestimates SWE by more than 50 mm in the Tibetan Plateau, North American Rocky Mountains, the coasts of Greenland, and the southern Andes across all seasons as well as part of northern Eurasia during winter and spring (Figure 14). Compared to the default baseline result, the new baseline simulation reduces the SWE bias by up to 50 mm in the coasts of Greenland across all seasons as well as over the Himalayas and part of North American Rocky Mountains during spring (Figures 14 and S14). This is because the increased snow albedo over those regions in the new baseline simulation (Section 4.1) reduces snow melting and hence increases SWE. Overall, the new baseline simulation reduces the mean SWE biases (underestimates) across mid- and high-latitudes, particularly over northern mid-latitudes (Table 2).

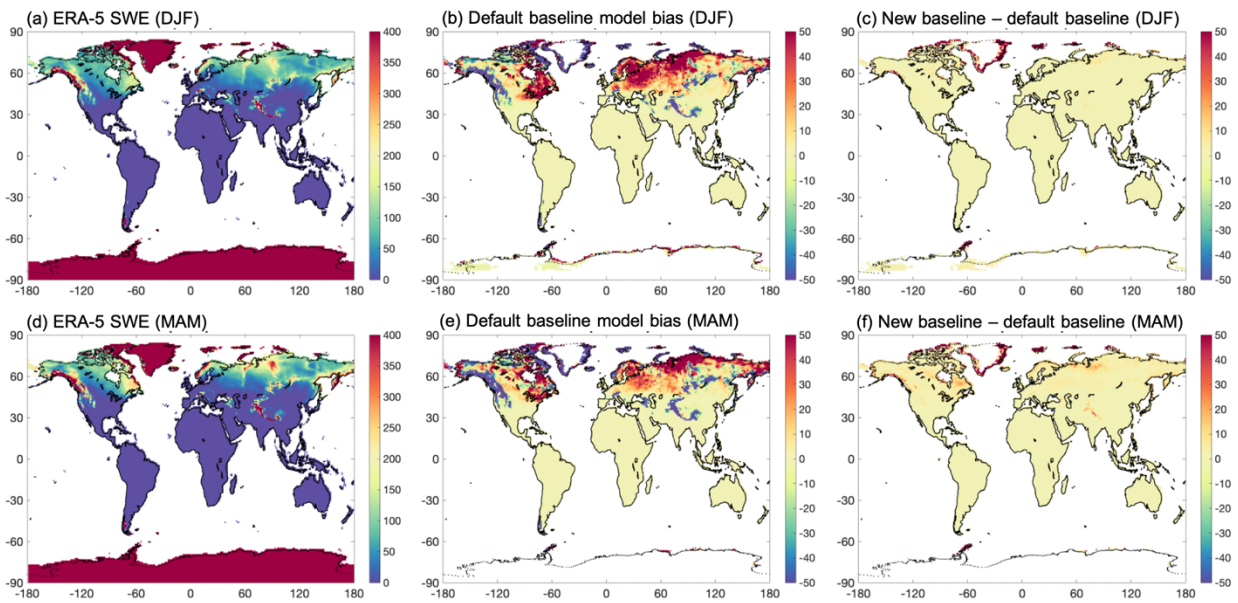

Figure 14. Comparison between ERA-5 and model simulations of 5-year (2006-2010) seasonal mean SWE (mm). First column (a, d): ERA-5 data (values >400 mm also show dark red color); second column (b, e): default baseline simulation bias; third column (c, f): difference between new and default baseline simulations. First row (a, b, c): winter (December-January-February); second row (d, e, f): spring (March-April-May). Note that most Greenland and Antarctic glacier regions with model snow capping at 10,000 kg/m^2 are screened out in second and third columns. See Figure S14 for results in summer (June-July-August) and fall (September-October-November) with relatively smaller effects from the new baseline simulation.

4.4 Snow depth

Figures 15 and S15 shows the comparison between ERA-5 and CLM5 simulated 5-year seasonal mean snow depth. Similar to the SWE evaluation (Sect. 4.3), we screened out the regions with model SWE capping at 10,000 kg/m^2 (mainly Greenland and Antarctic ice sheets). The default baseline simulation substantially underestimates snow depth by 0.2 m or more over the coasts of Greenland, the Tibetan Plateau, and the southern Andes throughout the year, as well as in the North American Rocky Mountains and many parts of northern Eurasia during winter, spring, and fall (Figures 15 and S15). Compared to the default baseline result, the new baseline simulation reduces the snow depth bias by 0.2 m or more over the coasts of Greenland across all seasons and by up to 0.1 m in the Himalayas and part of North American Rocky Mountains during spring (Figures 15 and S15). This is caused by the less light absorption by snowpack over those regions in the new baseline simulation (Section 4.1), which weakens snow densification/melting and hence increases snow depth. Overall, the new baseline simulation reduces the mean snow depth biases (underestimates) across mid- and high-latitudes, particularly in northern mid-latitudes (Table 2).

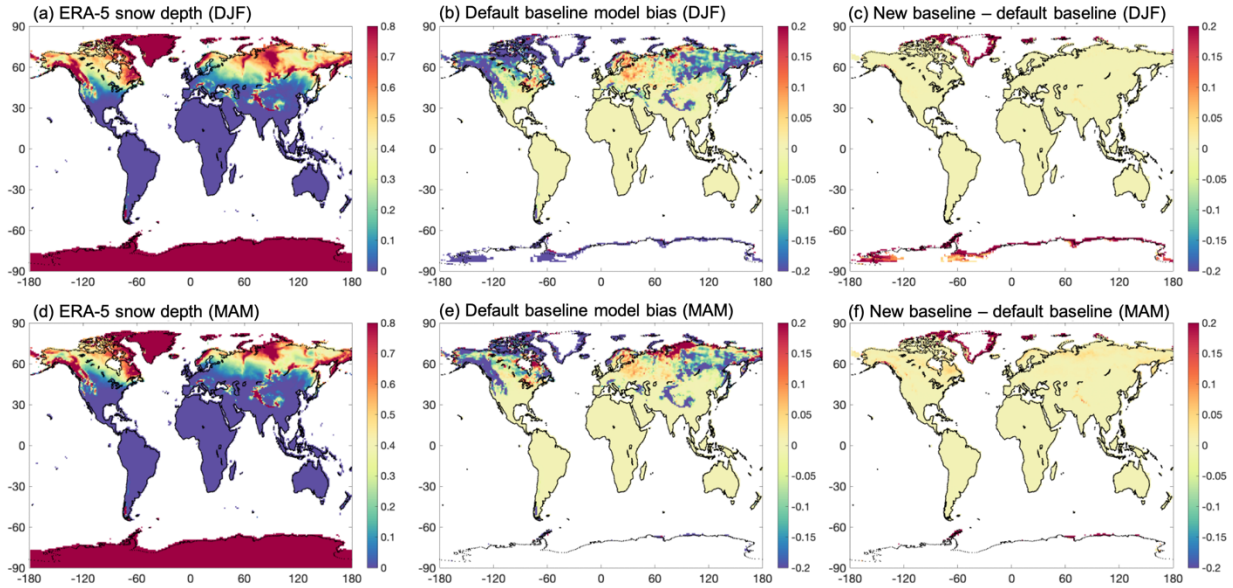

Figure 15. Same as Figure 14, but for snow depth (m) comparison between ERA-5 and model simulations. For ERA-5 snow depth, values >0.8 m also show dark red color in panels (a) and (d). Note that most Greenland and Antarctic glacier regions with model snow capping at 10,000 kg/m^2 are screened out in second and third columns. See Figure S15 for results in summer (June-July-

August) and fall (September-October-November) with relatively smaller effects from the new baseline simulation.

4.5 Surface temperature

Figures 16 and S16 shows the comparison between ERA-5 and CLM5 simulated 5-year annual and seasonal mean surface (2-m) temperature, respectively. The default baseline simulation generally overestimates the surface temperature by ~5°C over the majority of Greenland, Tibetan Plateau, and Antarctic throughout the year, and underestimates in part of northern Eurasia and northern Canada mainly during winter and spring. Compared to the default baseline result, the new baseline simulation reduces the surface temperature overestimates by up to 0.5°C over the Antarctic during winter and fall, Greenland during spring and summer, and part of Tibetan Plateau and North American Rocky Mountains during winter and spring (Figures 16 and S16). This is because of the increased snow albedo and hence less land surface heating by solar radiation absorption over those regions in the new baseline simulation (Section 4.1). The new baseline simulation, however, tends to slightly worsen the model temperature bias in part of northern Eurasia and northern Canada during spring. Overall, the new baseline simulation reduces the mean surface temperature biases (overestimates) across northern and southern mid- and high-latitudes (Table 2). The impact on surface temperature, which is strongly constrained by the forcing temperature in land-only simulations, is expected to be much stronger in a coupled climate simulation through positive snow albedo feedbacks.

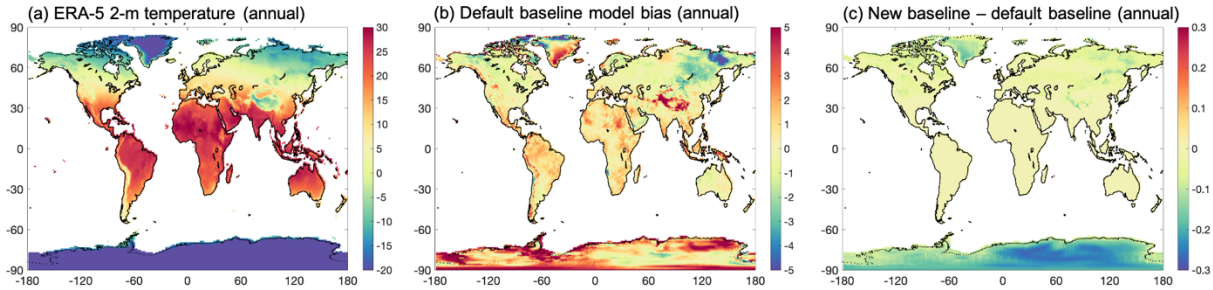

Figure 16. Comparison between ERA-5 and model simulations of 5-year (2006-2010) annual mean 2-m surface temperature (°C): (a) ERA-5 data, (b) default baseline simulation bias, and (c) difference between new and default baseline simulations.

5. Conclusions

In this study, we enhanced the CLM5-SNICAR snow albedo modeling by implementing several new features with more realistic and physical representations of snow-aerosol-radiation interactions. Specifically, we incorporated the following model enhancements: (1) updating ice and aerosol optical properties with more realistic and accurate datasets; (2) adding multiple dust types; (3) adding multiple surface downward solar spectra to account for different atmospheric conditions; (4) incorporating a more accurate adding-doubling radiative transfer solver; (5) adding nonspherical snow grain representation; (6) adding BC-snow and dust-snow internal mixing representations; (7) adding a hyperspectral (480-band versus the default 5-band) modeling capability. These model features/enhancements have been included as new CLM physics/namelist options, which allows for quantifying model sensitivities to snow albedo processes and for conducting relevant multi-physics model ensemble analyses for uncertainty assessment. The model updates will be included in the next CESM/CLM version release. Sensitivity analyses revealed stronger impacts of using the new adding-doubling solver, nonspherical snow grains, and BC/dust-snow internal mixing than the other new features/enhancements.

These enhanced snow albedo representations improve the CLM5 modeled global snowpack evolution and land surface conditions. Specifically, the enhanced CLM5-SNICAR leads to (1) a reduced snow surface albedo bias in northern mid-latitudes across all seasons; (2) a reduced snow cover bias in the Tibetan Plateau and North American Rocky Mountains during winter and spring, part of northern Eurasia during spring and summer, and the southern Andes during summer and fall; (3) a reduced SWE bias in the coasts of Greenland throughout the year and over the Tibetan Plateau and North American Rocky Mountains during spring; (4) a reduced snow depth bias in the coasts of Greenland throughout the year and in part of the Tibetan plateau and North American Rocky Mountains during spring; (5) a reduced surface temperature bias over the Antarctic during winter and fall, Greenland during spring and summer, and part of the Tibetan Plateau and North American Rocky Mountains during winter and spring. We note, however, that there are some regions without any model improvement or even with degradation by using the enhanced CLM5-SNICAR, such as the snow surface albedo in some high-latitude regions.

In future studies, coupled climate model simulations with the enhanced CLM5-SNICAR are needed to assess the full climatic impacts of the snow albedo enhancements added in this study, which are expected to be stronger than those shown here due to positive snow albedo feedback.

Acknowledgements

The authors declare no conflict of interest. This research was funded by the U.S. National Oceanic and Atmospheric Administration (NOAA) Climate Process Team project Award# 4000178550 and Award# NA19OAR4310243. NCAR is sponsored by the U.S. National Science Foundation. Any opinions, findings, conclusions, or recommendations expressed in this publication are those of the authors and do not necessarily reflect the views of the National Science Foundation.

Open Research

The default CLM5-SNICAR (CTSM Development Team, 2022) code is at:
https://github.com/ESCOMP/CTSM

The enhanced CLM5-SNICAR (CTSM Development Team, 2022) code is at:
https://github.com/ESCOMP/CTSM/pull/1861

MODIS surface albedo data (MCD43C3; Schaaf and Wang, 2021) is available at:
https://lpdaac.usgs.gov/products/mcd43c3v061/

MODIS snow cover data (MOD10C1 and MYD10C1; Hall and Riggs, 2021a, b) is available at:
https://nsidc.org/data/mod10c1/versions/61 and https://nsidc.org/data/myd10c1/versions/61

ERA-5 land data (SWE, snow depth, surface temperature; Muñoz Sabater, 2019) is available at:
https://cds.climate.copernicus.eu/cdsapp#!/dataset/reanalysis-era5-land-monthly-means?tab=overview

The model data generated in this study (He et al., 2023) is at:
https://doi.org/10.5281/zenodo.7986830

References

Abolafia-Rosenzweig, R., He, C., McKenzie Skiles, S., Chen, F., & Gochis, D. (2022). Evaluation and optimization of snow albedo scheme in Noah-MP land surface model using in situ spectral observations in the Colorado Rockies. Journal of Advances in Modeling Earth Systems, 14, e2022MS003141. https://doi. org/10.1029/2022MS003141

Bales, R. C., Molotch, N. P., Painter, T. H., Dettinger, M. D., Rice, R., & Dozier, J. (2006). Mountain hydrology of the western United States. Water Resources Research, 42(8), 1–13. https://doi.org/10.1029/2005WR004387

Briegleb BP, Light B (2007) A delta-eddington multiple scattering parameterization for solar radiation in the sea ice component of the community climate system Model. NCAR Tech. Note 472 1 STR, 100 pp

Chen, F., Barlage, M., Tewari, M., Rasmussen, R., Jin, J., Lettenmaier, D., et al. (2014). Modeling seasonal snowpack evolution in the complex terrain and forested Colorado Headwaters region: A model intercomparison study. Journal of Geophysical Research - D: Atmos- pheres, 119, 13795–13819. https://doi.org/10.1002/2014JD022167

Cook, J. M., Hodson, A. J., Gardner, A. S., Flanner, M., Tedstone, A. J., Williamson, C., ... and Tranter, M. (2017). Quantifying bioalbedo: a new physically based model and discussion of empirical methods for characterising biological influence on ice and snow albedo. The Cryosphere, 11(6), 2611-2632.

CTSM Development Team. (2022). ESCOMP/CTSM: NEON release: Some NEON updates fixing AG sites, update MOSART, small fixes (ctsm5.1.dev114). [Software]. Zenodo. https://doi.org/10.5281/zenodo.7342803

Danabasoglu, G., Lamarque, J. F., Bacmeister, J., et al. (2020). The Community Earth System Model Version 2 (CESM2). Journal of Advances in Modeling Earth Systems, 12, doi:10.1029/2019MS001916.

Dang C, Brandt RE, Warren SG (2015) Parameterizations for narrowband and broadband albedo of pure snow and snow containing mineral dust and black carbon. Journal of Geophysical Research: Atmospheres 120, 5446–5468. doi:10.1002/2014JD022646

Dang C, Fu Q, Warren SG (2016) Effect of snow grain shape on snow albedo. Journal of the Atmospheric Sciences 73(9), 3573–3583. doi:10.1175/JAS-D-15-0276.1

Dang C, Zender CS, Flanner MG (2019) Intercomparison and improvement of two-stream shortwave radiative transfer schemes in Earth system models for a unified treatment of cryospheric surfaces. The Cryosphere 13(9), 2325–2343. doi:10.5194/tc-13-2325-2019

Dirmeyer, P. A., Gao, X., Zhao, M., Guo, Z., Oki, T., and Hanasaki, N.: GSWP-2: Multimodel Analysis and Implications for Our Per- ception of the Land Surface, B. Am. Meteorol. Soc., 87, 1381– 1398, 2006.

Dominé, F., Lauzier, T., Cabanes, A., Legagneux, L., Kuhs, W. F., Techmer, K., & Heinrichs, T. (2003). Snow metamorphism as revealed by scanning electron microscopy. Microscopy Research and Technique, 62(1), 33–48. https://doi.org/10.1002/jemt.10384

Dumont, M., Tuzet, F., Gascoin, S., Picard, G., Kutuzov, S., Lafaysse, M., ... and Painter, T. H. (2020). Accelerated snow melt in the Russian Caucasus mountains after the Saharan dust outbreak in March 2018. Journal of Geophysical Research: Earth Surface, 125(9), e2020JF005641.

Dumont, M., Flin, F., Malinka, A., Brissaud, O., Hagenmuller, P., Lapalus, P., ... and Ando, E. (2021). Experimental and model-based investigation of the links between snow bidirectional reflectance and snow microstructure. The Cryosphere, 15(8), 3921-3948.

Erbe, E. F., Rango, A., Foster, J., Josberger, E. G., Pooley, C., & Wergin, W. (2003). Collecting, shipping, storing, and imaging snow crystals and ice grains with low-temperature scanning electron microscopy. Microscopy Research and Technique, 62(1), 19–32. https://doi.org/10.1002/ jemt.10383

Essery, R., Rutter, N., Pomeroy, J., Baxter, R., Stahli, M., Gustafsson, D., et al. (2009). SNPWMIP2, An evalutation of froest snow process simulations. Bulletin of the American Meteorological Society, 90, 1120–1135.

Flanner, M. G., Zender, C. S., Randerson, J. T., and Rasch, P. J. (2007). Present-day climate forcing and response from black carbon in snow. Journal of Geophysical Research: Atmospheres, 112(D11).

Flanner, M. G., Shell, K. M., Barlage, M., Perovich, D. K., and Tschudi, M. A. (2011). Radiative forcing and albedo feedback from the Northern Hemisphere cryosphere between 1979 and 2008. Nature Geoscience, 4(3), 151–155. https://doi.org/10.1038/ngeo1062

Flanner, M. G., Liu, X., Zhou, C., Penner, J. E., and Jiao, C. (2012). Enhanced solar energy absorption by internally-mixed black carbon in snow grains. Atmospheric Chemistry and Physics, 12(10), 4699-4721.

Flanner, M. G., Gardner, A. S., Eckhardt, S., Stohl, A., and Perket, J. (2014). Aerosol radiative forcing from the 2010 Eyjafjallajökull volcanic eruptions. Journal of Geophysical Research: Atmospheres, 119(15), 9481-9491.

Flanner, M. G., Arnheim, J. B., Cook, J. M., Dang, C., He, C., Huang, X., ... and Zender, C. S. (2021). SNICAR-ADv3: a community tool for modeling spectral snow albedo. Geoscientific Model Development, 14(12), 7673-7704.

Gardner AS, Sharp MJ (2010) A review of snow and ice albedo and the development of a new physically based broadband albedo parameterization. Journal of Geophysical Research 115, F01009. doi:10.1029/ 2009JF001444

Gleason, K. E., McConnell, J. R., Arienzo, M. M., Chellman, N., & Calvin, W. M. (2019). Four-fold increase in solar forcing on snow in western US burned forests since 1999. Nature communications, 10(1), 2026.

Gelman Constantin, J., Ruiz, L., Villarosa, G., Outes, V., Bajano, F. N., He, C., ... and Dawidowski, L. (2020). Measurements and modeling of snow albedo at Alerce Glacier, Argentina: effects of volcanic ash, snow grain size, and cloudiness. The Cryosphere, 14(12), 4581-4601.

Golaz, J. C., Caldwell, P. M., Van Roekel, L. P., Petersen, M. R., Tang, Q., Wolfe, J. D., ... & Zhu, Q. (2019). The DOE E3SM coupled model version 1: Overview and evaluation at standard resolution. Journal of Advances in Modeling Earth Systems, 11(7), 2089-2129.

Gul, C., Mahapatra, P. S., Kang, S., Singh, P. K., Wu, X., He, C., ... and Puppala, S. P. (2021). Black carbon concentration in the central Himalayas: Impact on glacier melt and potential source contribution. Environmental Pollution, 275, 116544.

Hall, D. K. and G. A. Riggs. (2021a). MODIS/Terra Snow Cover Daily L3 Global 0.05Deg CMG, Version 61 [Dataset]. Boulder, Colorado USA. NASA National Snow and Ice Data Center Distributed Active Archive Center. https://doi.org/10.5067/MODIS/MOD10C1.061. Date Accessed 06-06-2023.

Hall, D. K. and G. A. Riggs. (2021b). MODIS/Aqua Snow Cover Daily L3 Global 0.05Deg CMG, Version 61 [Dataset]. Boulder, Colorado USA. NASA National Snow and Ice Data Center Distributed Active Archive Center. https://doi.org/10.5067/MODIS/MYD10C1.061. Date Accessed 06-06-2023.

Hao, D., Bisht, G., Rittger, K., Bair, E., He, C., Huang, H., ... & Leung, L. R. (2023). Improving snow albedo modeling in the E3SM land model (version 2.0) and assessing its impacts on snow and surface fluxes over the Tibetan Plateau. Geoscientific Model Development, 16(1), 75-94.

He, C., Q. Li, K.-N. Liou, Y. Takano, Y. Gu, L. Qi, Y. Mao, and L. R. Leung (2014), Black carbon radiative forcing over the Tibetan Plateau, Geophys. Res. Lett., 41, 7806–7813, doi:10.1002/2014GL062191.

He, C., Y. Takano, and K. N. Liou (2017a). Close packing effects on clean and dirty snow albedo and associated climatic implications. Geophys. Res. Lett., 44, 3719–3727

He, C., Y. Takano, K. N. Liou, P. Yang, Q. Li, and F. Chen (2017b). Impact of Snow Grain Shape and Black Carbon–Snow Internal Mixing on Snow Optical Properties: Parameterizations for Climate Models. Journal of Climate, 30(24), 10019-10036.

He, C., K. N. Liou, Y. Takano, P. Yang, L. Qi, and F. Chen (2018a). Impact of grain shape and multiple black carbon internal mixing on snow albedo: Parameterization and radiative effect analysis. J. Geophys. Res.-Atmos., 123, 1253–1268.

He, C., K. N. Liou, and Y. Takano (2018b). Resolving size distribution of black carbon internally mixed with snow: Impact on snow optical properties and albedo. Geophys. Res. Lett., 45, 2697–2705.

He, C., Flanner, M. G., Chen, F., Barlage, M., Liou, K. N., Kang, S., Ming, J., and Qian, Y. (2018c): Black carbon-induced snow albedo reduction over the Tibetan Plateau: uncertainties from snow grain shape and aerosol–snow mixing state based on an updated SNICAR model, Atmos. Chem. Phys., 18, 11507-11527, doi:10.5194/acp-18-11507-2018.

He, C., Chen, F., Barlage, M., Liu, C., Newman, A., Tang, W., et al. (2019a). Can convection-permitting modeling provide decent precipitation for offline high-resolution snowpack simulations over mountains?. Journal of Geophysical Research: Atmospheres, 124, 12,631–12,654. https://doi.org/ 10.1029/2019JD030823

He, C., Liou, K. N., Takano, Y., Chen, F., and Barlage, M. (2019b). Enhanced snow absorption and albedo reduction by dust-snow internal mixing: modeling and parameterization. Journal of Advances in Modeling Earth Systems, 11(11), 3755-3776.

He, C., and Flanner, M. (2020). Snow Albedo and Radiative Transfer: Theory, Modeling, and Parameterization. In Springer Series in Light Scattering (pp. 67-133). Springer, Cham.

He, C., Chen, F., Abolafia-Rosenzweig, R., Ikeda, K., Liu, C., & Rasmussen, R. (2021). What causes the unobserved early-spring snowpack ablation in convection-permitting WRF modeling over Utah mountains? Journal of Geophysical Research: Atmospheres, 126, e2021JD035284. https://doi. org/10.1029/2021JD035284

He, C. (2022): Modeling light-absorbing particle-snow-radiation interactions and impacts on snow albedo: fundamentals, recent advances, and future directions, Environmental Chemistry, doi:10.1071/EN22013

He, C., M. Flanner, D. Lawrence, and Y. Gu (2023). Model dataset for the journal publication entitled "New features and enhancements in Community Land Model (CLM5) snow albedo modeling: description, sensitivity, and evaluation" [Dataset]. Zenodo. https://doi.org/10.5281/zenodo.7986830

Huang, H., Qian, Y., He, C., Bair, E. H., & Rittger, K. (2022). Snow albedo feedbacks enhance snow impurity- induced radiative forcing in the Sierra Nevada. Geophysical Research Letters, 49, e2022GL098102. https://doi. org/10.1029/2022GL098102

Kaempfer TU, Hopkins MA, Perovich DK (2007) A three-dimensional microstructure-based photon-tracking model of radiative transfer in snow. J Geophys Res Atmos 112(D24)

Kokhanovsky, A. A., and E. P. Zege (2004). Scattering optics of snow. Applied Optics, 43(7), 1589-1602.

Lamarque, J.-F., Bond, T. C., Eyring, V., et al.: Historical (1850–2000) gridded anthropogenic and biomass burning emissions of reactive gases and aerosols: methodol- ogy and application, Atmos. Chem. Phys., 10, 7017–7039, https://doi.org/10.5194/acp-10-7017-2010, 2010.

Lawrence, D. M., Fisher, R. A., Koven, C. D., Oleson, K. W., Swenson, S. C., Bonan, G., et al. (2019). The Community Land Model version 5: Description of new features, benchmarking,

and impact of forcing uncertainty. Journal of Advances in Modeling Earth Systems, 11, 4245–4287. https://doi.org/10.1029/2018MS001583

Lee, W. L., Liou, K. N., He, C., Liang, H. C., Wang, T. C., Li, Q., ... and Yue, Q. (2017). Impact of absorbing aerosol deposition on snow albedo reduction over the southern Tibetan plateau based on satellite observations. Theoretical and Applied Climatology, 129(3), 1373-1382.

Li, C., Yan, F., Kang, S., Yan, C., Hu, Z., Chen, P., ... & Stubbins, A. (2021). Carbonaceous matter in the atmosphere and glaciers of the Himalayas and the Tibetan plateau: An investigative review. Environment International, 146, 106281.

Libois Q, Picard G, France JL, Arnaud L, Dumont M, Carmagnola CM, King MD (2013) Influence of grain shape on light penetration in snow. The Cryosphere 7(6), 1803–1818. doi:10.5194/tc-7-1803-2013

Liou, K. N., Takano, Y., He, C., Yang, P., Leung, L. R., Gu, Y., and Lee, W. L.: Stochastic parameterization for light absorp- tion by internally mixed BC/dust in snow grains for application to climate models, J. Geophys. Res.-Atmos., 119, 7616–7632, https://doi.org/10.1002/2014JD021665, 2014.

Liu, D., He, C., Schwarz, J. P., & Wang, X. (2020). Lifecycle of light-absorbing carbonaceous aerosols in the atmosphere. NPJ climate and atmospheric science, 3(1), 40.

Liu, X., Easter, R. C., Ghan, S. J., Zaveri, R., Rasch, P., Shi, X., Lamarque, J.-F., et al.: Toward a minimal representation of aerosols in climate models: description and evaluation in the Community Atmosphere Model CAM5, Geosci. Model Dev., 5, 709–739, https://doi.org/10.5194/gmd-5-709-2012, 2012.

Muñoz Sabater, J. (2019): ERA5-Land monthly averaged data from 1950 to present. Copernicus Climate Change Service (C3S) Climate Data Store (CDS). [Dataset]. doi:10.24381/cds.68d2bb30 (Accessed on 2023-06-06)

Oaida, C.M., Xue, Y., Flanner, M.G., Skiles, S.M., De Sales, F. and Painter, T.H. (2015). Improving snow albedo processes in WRF/SSiB regional climate model to assess impact of dust and black carbon in snow on surface energy balance and hydrology over western US. Journal of Geophysical Research: Atmospheres, 120(8), pp.3228-3248.

Painter, T. H., Deems, J. S., Belnap, J., Hamlet, A. F., Landry, C. C., and Udall, B. (2010). Response of Colorado River runoff to dust radiative forcing in snow. Proceedings of the National Academy of Sciences, 107(40), 17125-17130.

Perovich, D. K. and Govoni, J. W.: Absorption Coefficients Of Ice From 250 To 400 nm, Geophys. Res. Lett., 18, 1233–1235, https://doi.org/10.1029/91GL01642, 1991.

Picard, G., Libois, Q., and Arnaud, L.: Refinement of the ice ab- sorption spectrum in the visible using radiance profile measurements in Antarctic snow, The Cryosphere, 10, 2655–2672, https://doi.org/10.5194/tc-10-2655-2016, 2016.

Picard, G., Dumont, M., Lamare, M., Tuzet, F., Larue, F., Pirazzini, R., and Arnaud, L.: Spectral albedo measurements over snow-covered slopes: theory and slope effect corrections, The Cryosphere, 14, 1497–1517, https://doi.org/10.5194/tc-14-1497- 2020, 2020.

Polashenski, C. M., Dibb, J. E., Flanner, M. G., Chen, J. Y., Courville, Z. R., Lai, A. M., Schauer, J. J., Shafer, M. M., and Bergin, M.: Neither dust nor black carbon causing apparent albedo decline in Greenland's dry snow zone: Implications for MODIS C5 surface reflectance, Geophys. Res. Lett., 42, 9319– 9327, https://doi.org/10.1002/2015GL065912, 2015.

Pu, W., Shi, T., Cui, J., Chen, Y., Zhou, Y., and Wang, X. (2021). Enhancement of snow albedo reduction and radiative forcing due to coated black carbon in snow. The Cryosphere, 15(5), 2255-2272.

Qian, Y., Yasunari, T. J., Doherty, S. J., Flanner, M. G., Lau, W. K., Ming, J., ... and Zhang, R. (2015). Light-absorbing particles in snow and ice: Measurement and modeling of climatic and hydrological impact. Advances in Atmospheric Sciences, 32(1), 64-91.

Räisänen, P., R. Makkonen, A. Kirkevåg, and J. B. Debernard (2017). Effects of snow grain shape on climate simulations: sensitivity tests with the Norwegian Earth System Model. The Cryosphere, 11, 2919–2942.

Roeckner E, Bauml G, Bonaventura L et al (2003) The atmospheric general circulation model ECHAM5. Part I: model description. Max Planck Institute for Meteorology, Rep 349, 127 pp

Saito M, Yang P, Loeb NG, Kato S (2019) A novel parameterization of snow albedo based on a two-layer snow model with a mixture of grain habits. J Atmos Sci 76(5):1419–1436

Scanza, R. A., Mahowald, N., Ghan, S., Zender, C. S., Kok, J. F., Liu, X., Zhang, Y., and Albani, S.: Modeling dust as component minerals in the Community Atmosphere Model: development of framework and impact on radiative forcing, Atmos. Chem. Phys., 15, 537–561, https://doi.org/10.5194/acp-15-537-2015, 2015.

Schaaf, C., Wang, Z. (2021). MODIS/Terra+Aqua BRDF/Albedo Albedo Daily L3 Global 0.05Deg CMG V061 [Dataset]. NASA EOSDIS Land Processes DAAC. Accessed 2023-06-06 from https://doi.org/10.5067/MODIS/MCD43C3.061

Shi T, Cui J, Chen Y, Zhou Y, Pu W, Xu X, et al. (2021) Enhanced light absorption and reduced snow albedo due to internally mixed mineral dust in grains of snow. Atmospheric Chemistry and Physics 21(8), 6035–6051. doi:10.5194/acp-21-6035-2021

Shi, T., He, C., Zhang, D., Zhang, X., Niu, X., Xing, Y., ... & Wang, X. (2022). Opposite Effects of Mineral Dust Nonsphericity and Size on Dust-Induced Snow Albedo Reduction. Geophysical Research Letters, 49(12), e2022GL099031.

Skiles, S. M. and Painter, T.: Daily evolution in dust and black carbon content, snow grain size, and snow albedo during snowmelt, Rocky Mountains, Colorado, J. Glaciol., 63, 118–132, https://doi.org/10.1017/jog.2016.125, 2017.

Skiles, S. M., Flanner, M., Cook, J. M., Dumont, M., and Painter, T. H. (2018). Radiative forcing by light-absorbing particles in snow. Nature Climate Change, 8(11), 964-971.

Stamnes K, Tsay SC, Wiscombe W, Jayaweera K (1988) Numerically stable algorithm for discrete-ordinate-method radiative transfer in multiple scattering and emitting layered media. Appl Opt 27(12):2502–2509

Thackeray, C. W., and Fletcher, C. G. (2016). Snow albedo feedback: Current knowledge, importance, outstanding issues and future directions. Progress in Physical Geography, 40(3), 392-408.

Thackeray, C. W., Fletcher, C. G., & Derksen, C. (2019). Diagnosing the impacts of Northern Hemisphere surface albedo biases on simulated climate. Journal of Climate, 32(6), 1777-1795.

Toon, O. B., McKay, C. P., Ackerman, T. P., and Santhanam, K.: Rapid calculation of radiative heating rates and photodissocia- tion rates in inhomogeneous multiple scattering atmospheres, J. Geophys. Res., 94, 16287–16301, 1989.

Toure, A. M., Luojus, K., Rodell, M., Beaudoing, H., & Getirana, A. (2018). Evaluation of simulated snow and snowmelt timing in the Community Land Model using satellite-based products and streamflow observations. Journal of Advances in Modeling Earth Systems, 10, 2933–2951. https://doi.org/ 10.1029/2018MS001389

Tuzet F, Dumont M, Lafaysse M et al (2017) A multilayer physically based snowpack model simulating direct and indirect radiative impacts of light-absorbing impurities in snow. Cryosphere, 11(6):2633–2653

Verseghy DL (1991) CLASS–A Canadian land surface scheme for GCMs. I. Soil model. Int J Climatol 11(2):111–133

Vionnet V, Brun E, Morin S et al (2012) The detailed snowpack scheme Crocus and its implementation in SURFEX v7. 2. Geosci Model Dev 5:773–791

Wang, W., He, C., Moore, J., Wang, G., & Niu, G. Y. (2022). Physics-Based Narrowband Optical Parameters for Snow Albedo Simulation in Climate Models. Journal of Advances in Modeling Earth Systems, 14(1), e2020MS002431.

Warren, S. G.: Optical constants of ice from the ultraviolet to the microwave, Appl. Optics, 23, 1206–1225, 1984.

Warren, S. G. and Brandt, R. E.: Optical constants of ice from the ultraviolet to the microwave: A revised compilation, J. Geophys. Res., 113, D14220, https://doi.org/10.1029/2007JD009744, 2008.

Warren SG, Wiscombe WJ (1980) A model for the spectral albedo of snow. II: Snow containing atmospheric aerosols. J Atmos Sci 37(12):2734–2745

Wiscombe WJ, Warren SG (1980) A model for the spectral albedo of snow. I: Pure snow. Journal of the Atmospheric Sciences 37(12), 2712–2733.

Williamson, C. J., Cook, J., Tedstone, A., Yallop, M., McCutcheon, J., Poniecka, E., ... and Anesio, A. (2020). Algal photophysiology drives darkening and melt of the Greenland Ice Sheet. Proceedings of the National Academy of Sciences, 117(11), 5694-5705.

Yan, F., He, C., Kang, S., Chen, P., Hu, Z., Han, X., ... & Li, C. (2019). Deposition of organic and black carbon: direct measurements at three remote stations in the Himalayas and Tibetan Plateau. Journal of Geophysical Research: Atmospheres, 124(16), 9702-9715.

Yang, Z. L., Dickinson, R. E., Robock, A., & Vinnikov, K. Y. (1997). Validation of the snow submodel of the biosphere–atmosphere transfer scheme with Russian snow cover and meteorological observational data. Journal of climate, 10(2), 353-373.

Yi, K., Meng, J., Yang, H., He, C., Henze, D. K., Liu, J., ... and Tao, S. (2019). The cascade of global trade to large climate forcing over the Tibetan Plateau glaciers. Nature communications, 10(1), 1-9.

Young, C. L., Sokolik, I. N., Flanner, M. G., and Dufek, J. (2014). Surface radiative impacts of ash deposits from the 2009 eruption of Redoubt volcano. Journal of Geophysical Research: Atmospheres, 119(19), 11-387.

Journal of Advances in Modeling Earth Systems

Supporting Information for

New features and enhancements in Community Land Model (CLM5) snow albedo modeling: description, sensitivity, and evaluation

Cenlin He[1], Mark Flanner[2], David M. Lawrence[1], Yu Gu[3]

1. National Center for Atmospheric Research (NCAR), Boulder, CO, USA
2. University of Michigan Ann Arbor, MI, USA
3. University of California Los Angeles, CA, USA

Correspondence to: Cenlin He (cenlinhe@ucar.edu)

Content of this file:

Figures S1 to S16

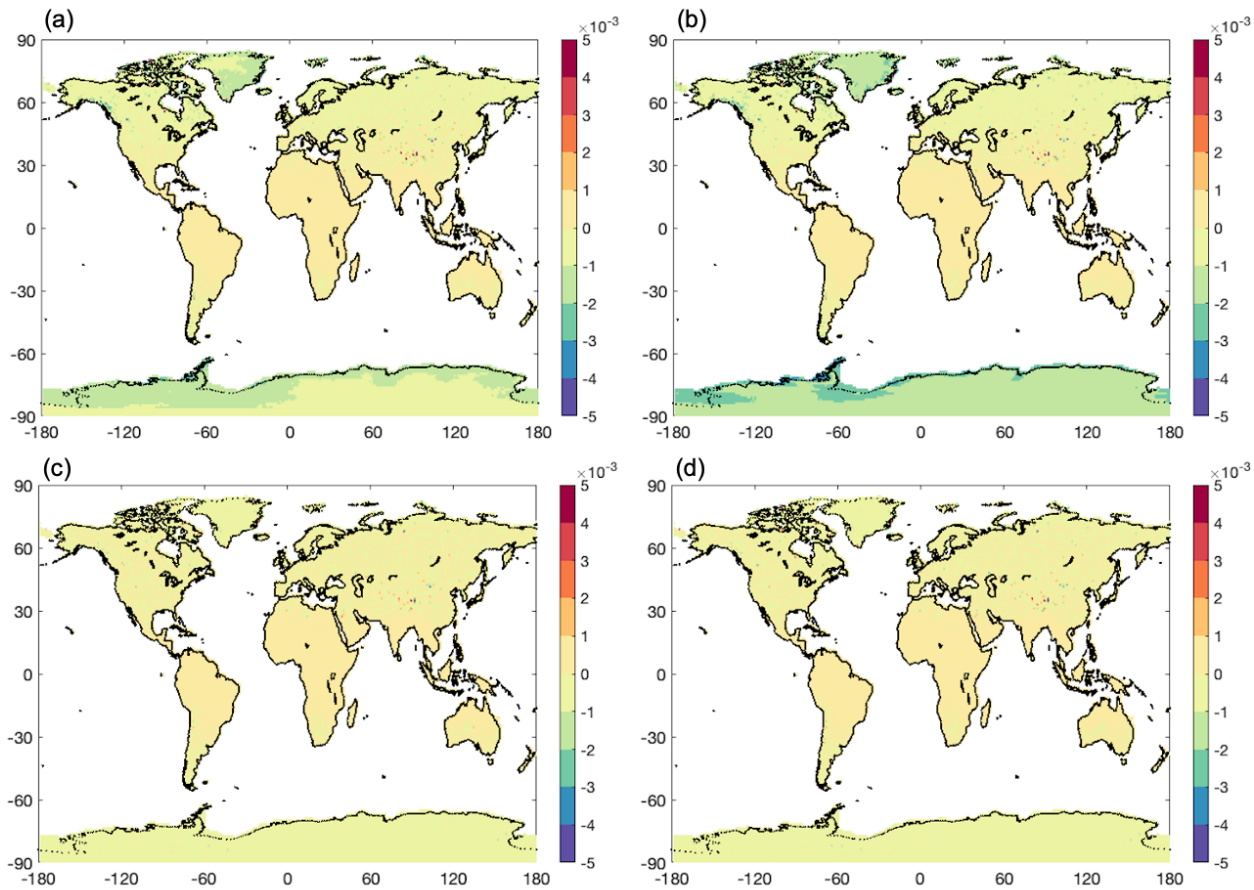

Figure S1. 5-year (2006-2010) annual mean effects of updated ice optical properties (i.e., differences between simulations using the Picard et al. (2016) and Warren and Brandt (2008) visible ice refractive indices): (a) difference for direct-beam visible snow albedo, (b) difference for diffuse visible snow albedo, (c) difference for direct-beam NIR snow albedo, (d) difference for diffuse NIR snow albedo.

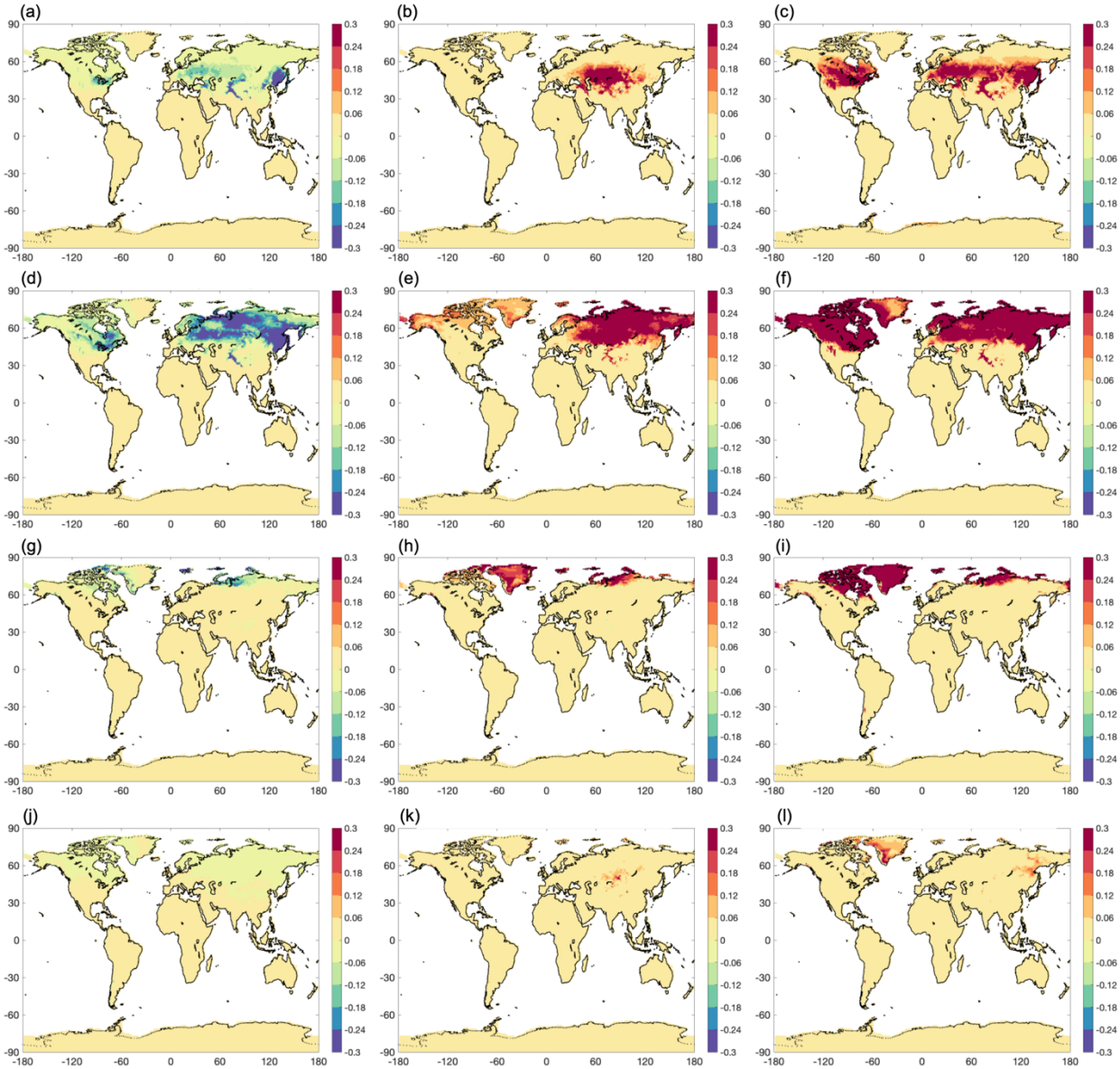

Figure S2. 5-year (2006-2010) all-sky seasonal mean effects of updated aerosol optical properties (i.e., differences between simulations using the Flanner et al. (2021) and Flanner et al. (2007) data). First column: difference for BC-induced snow albedo forcing (W m^{-2}); second column: difference for dust-induced snow albedo forcing (W m^{-2}); third column: difference for OC-induced snow albedo forcing (W m^{-2}). First row: winter (December-January-February); second row: spring (March-April-May); third row: summer (June-July-August); fourth row: fall (September-October-November).

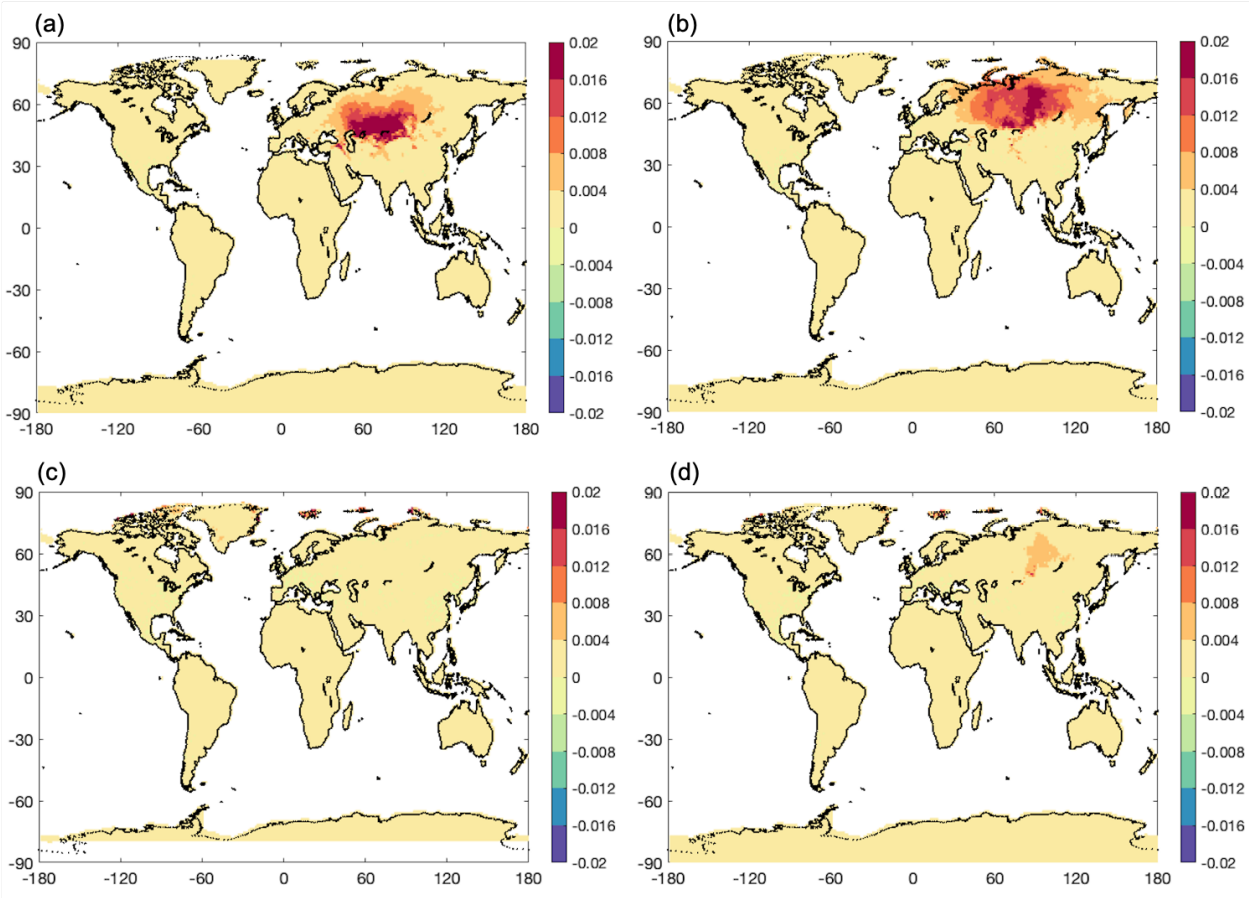

Figure S3. 5-year (2006-2010) all-sky seasonal mean effects of different dust types (i.e., differences between simulations using Greenland dust and Colorado dust) on snow-covered ground albedo reduction caused by dust: (a) winter (December-January-February), (b) spring (March-April-May), (c) summer (June-July-August), (d) fall (September-October-November).

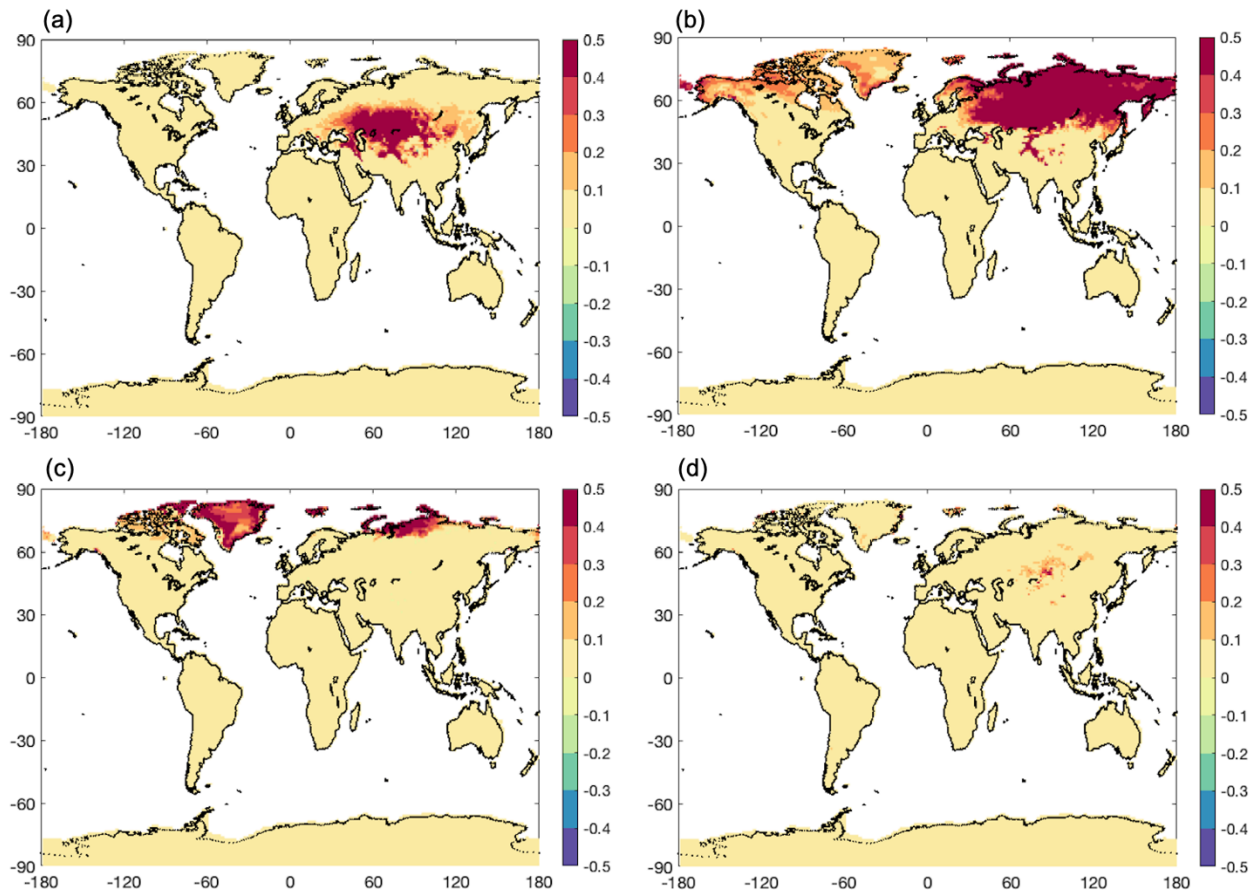

Figure S4. 5-year (2006-2010) all-sky seasonal mean effects of different dust types (i.e., differences between simulations using Greenland dust and Colorado dust) on dust-induced snow albedo forcing (W m^{-2}): (a) winter (December-January-February), (b) spring (March-April-May), (c) summer (June-July-August), (d) fall (September-October-November).

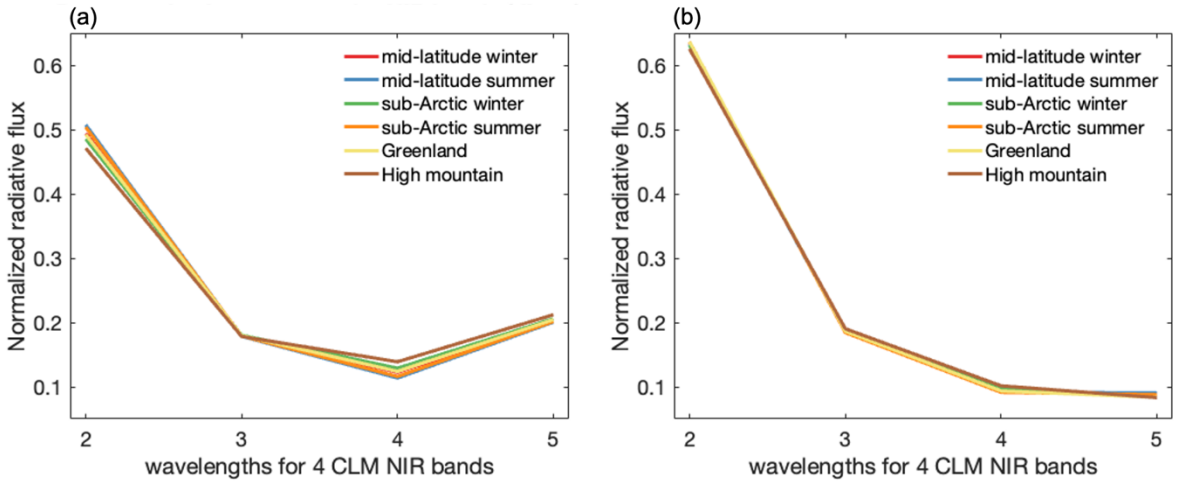

Figure S5. Normalized downward solar radiative flux spectra for six different atmospheric conditions at the four CLM near-infrared (NIR) bands for (a) direct and (b) diffuse radiation.

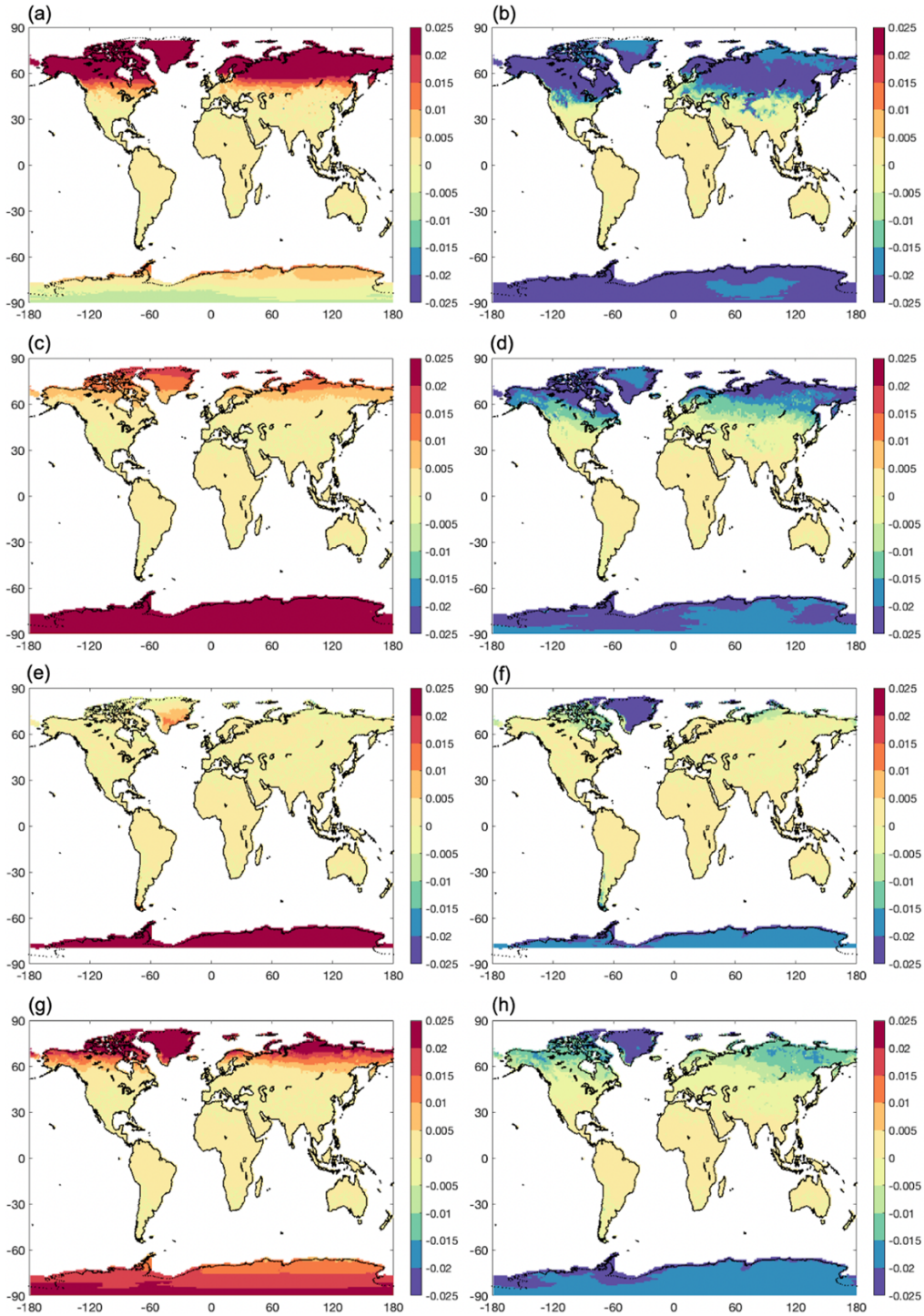

Figure S6. 5-year (2006-2010) seasonal mean effects of updated snow radiative transfer solvers (i.e., differences between simulations using the adding-doubling and Toon et al. (1989) solvers) on NIR snow albedo. First column: difference under direct radiation; second column: difference under diffuse radiation. First row: winter (December-January-February); second row: spring (March-April-May); third row: summer (June-July-August); fourth row: fall (September-October-November).

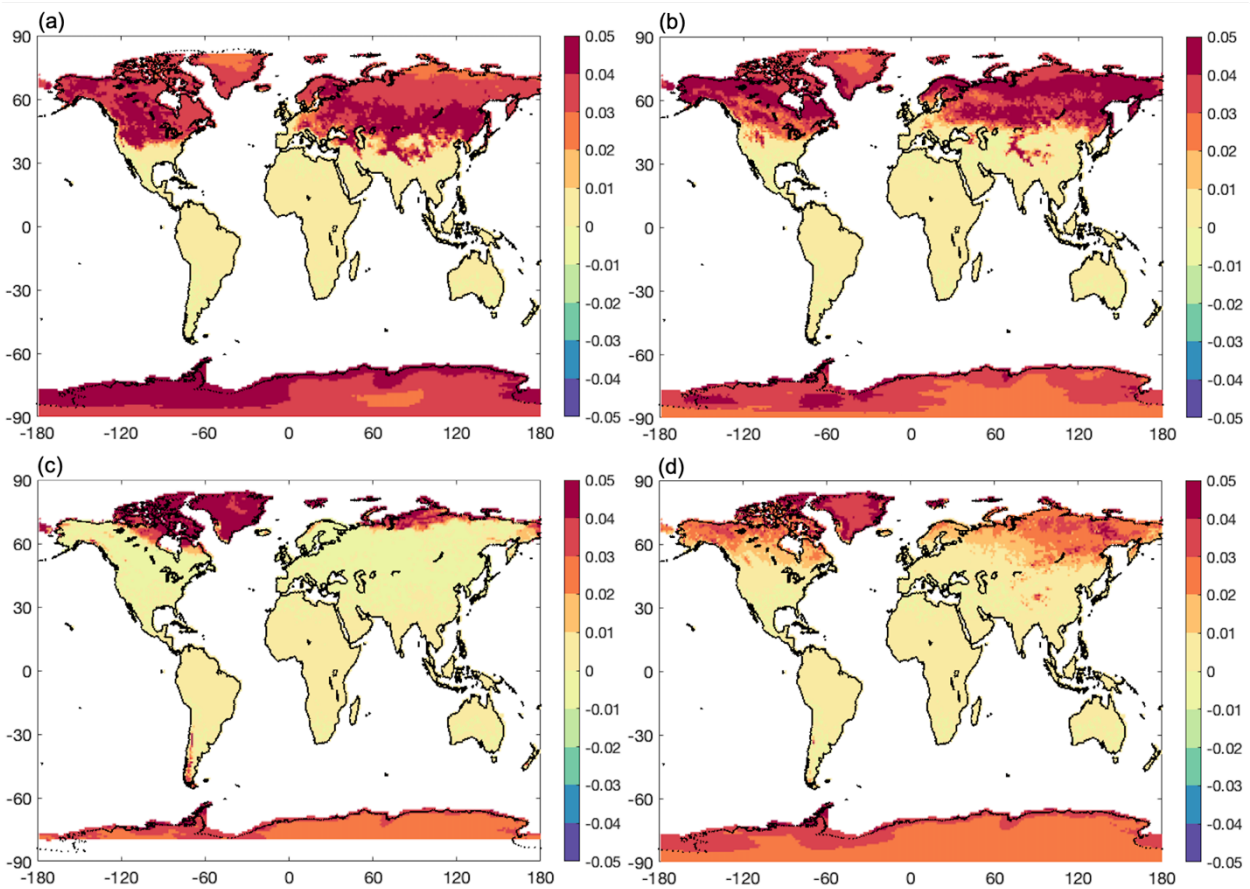

Figure S7. 5-year (2006-2010) all-sky annual mean effects of nonspherical snow grain (i.e., differences between simulations using fractal snowflake and snow sphere) on broadband snow albedo: (a) winter (December-January-February), (b) spring (March-April-May), (c) summer (June-July-August), (d) fall (September-October-November).

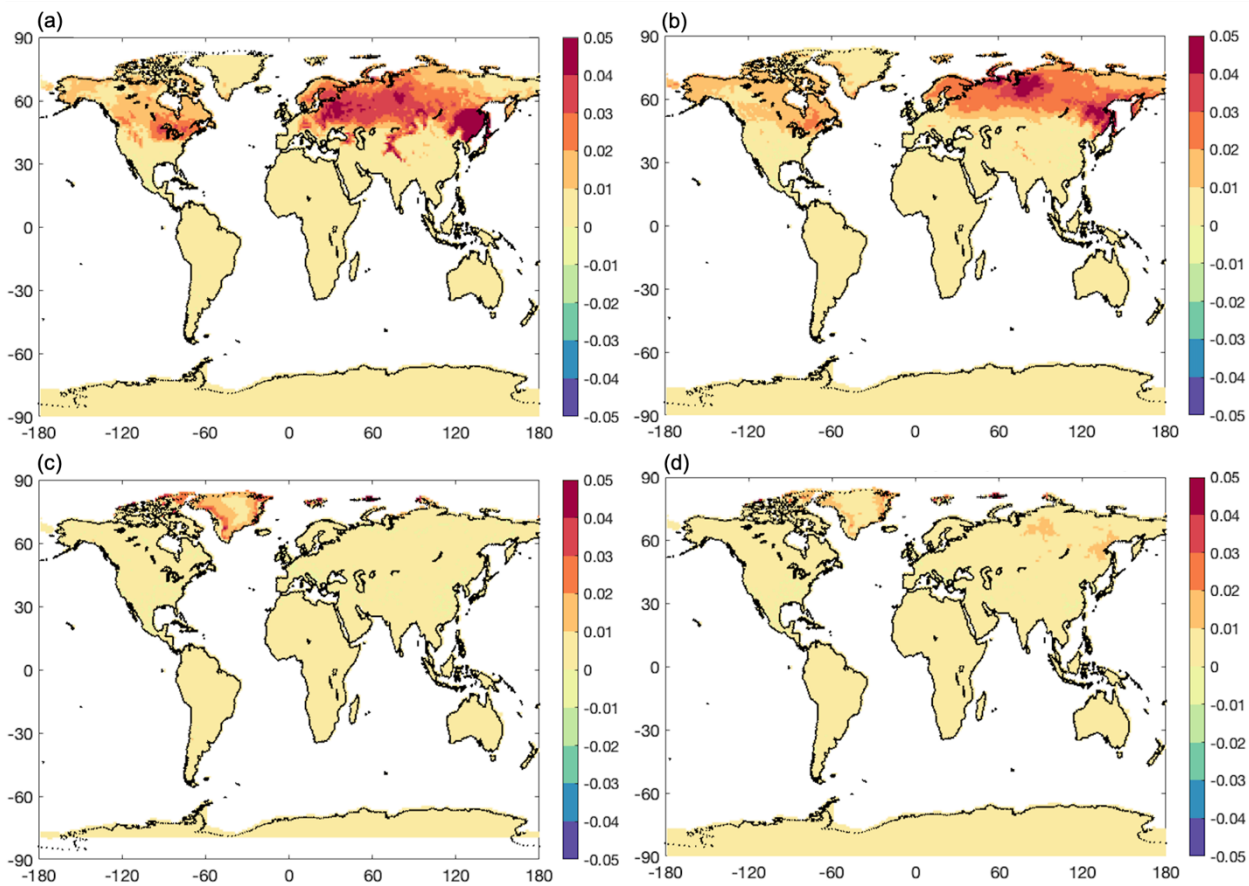

Figure S8. 5-year (2006-2010) all-sky annual mean effects of BC-snow internal mixing (i.e., differences between simulations using BC-snow internal mixing and external mixing) on BC-induced snow ground albedo reduction: (a) winter (December-January-February), (b) spring (March-April-May), (c) summer (June-July-August), (d) fall (September-October-November).

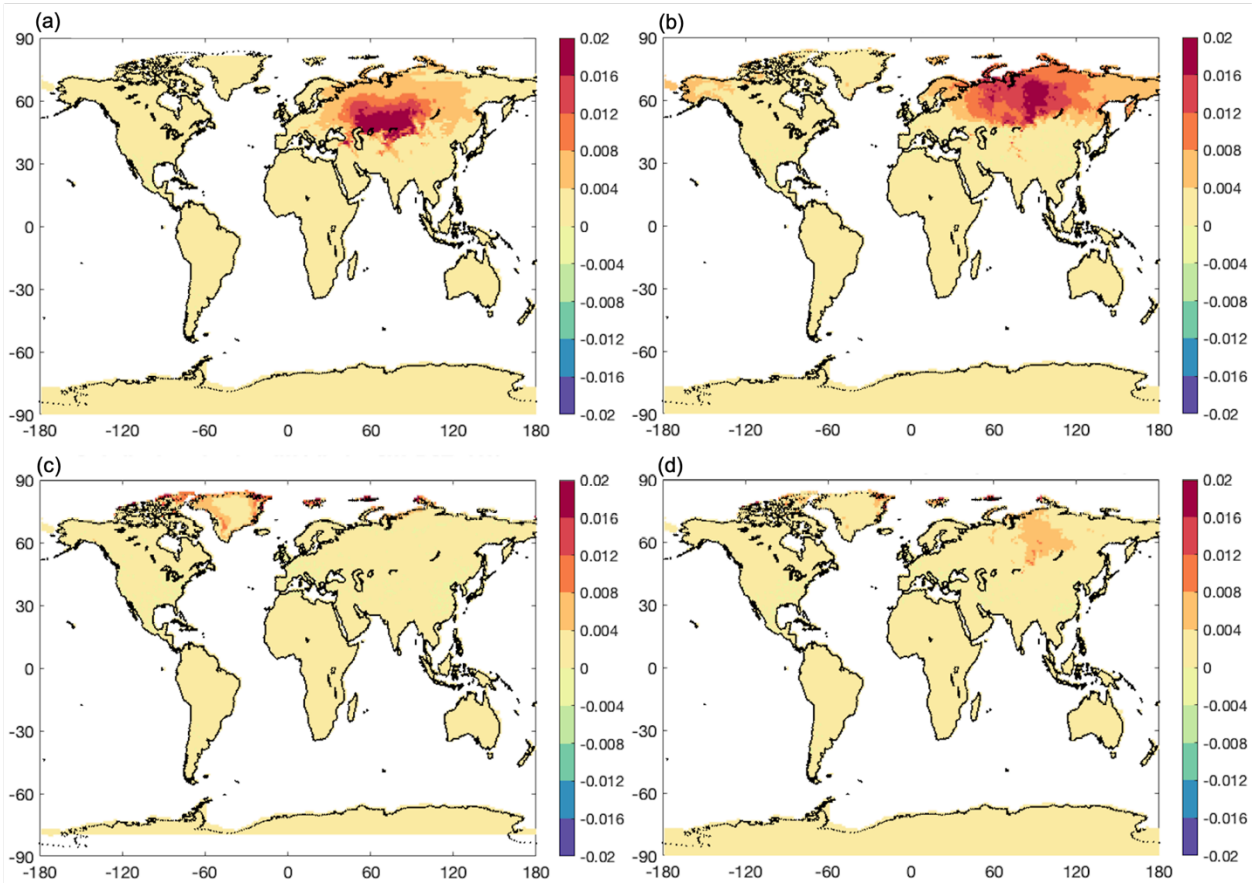

Figure S9. 5-year (2006-2010) all-sky annual mean effects of dust-snow internal mixing (i.e., differences between simulations using dust-snow internal mixing and external mixing) on dust-induced snow ground albedo reduction: (a) winter (December-January-February), (b) spring (March-April-May), (c) summer (June-July-August), (d) fall (September-October-November).

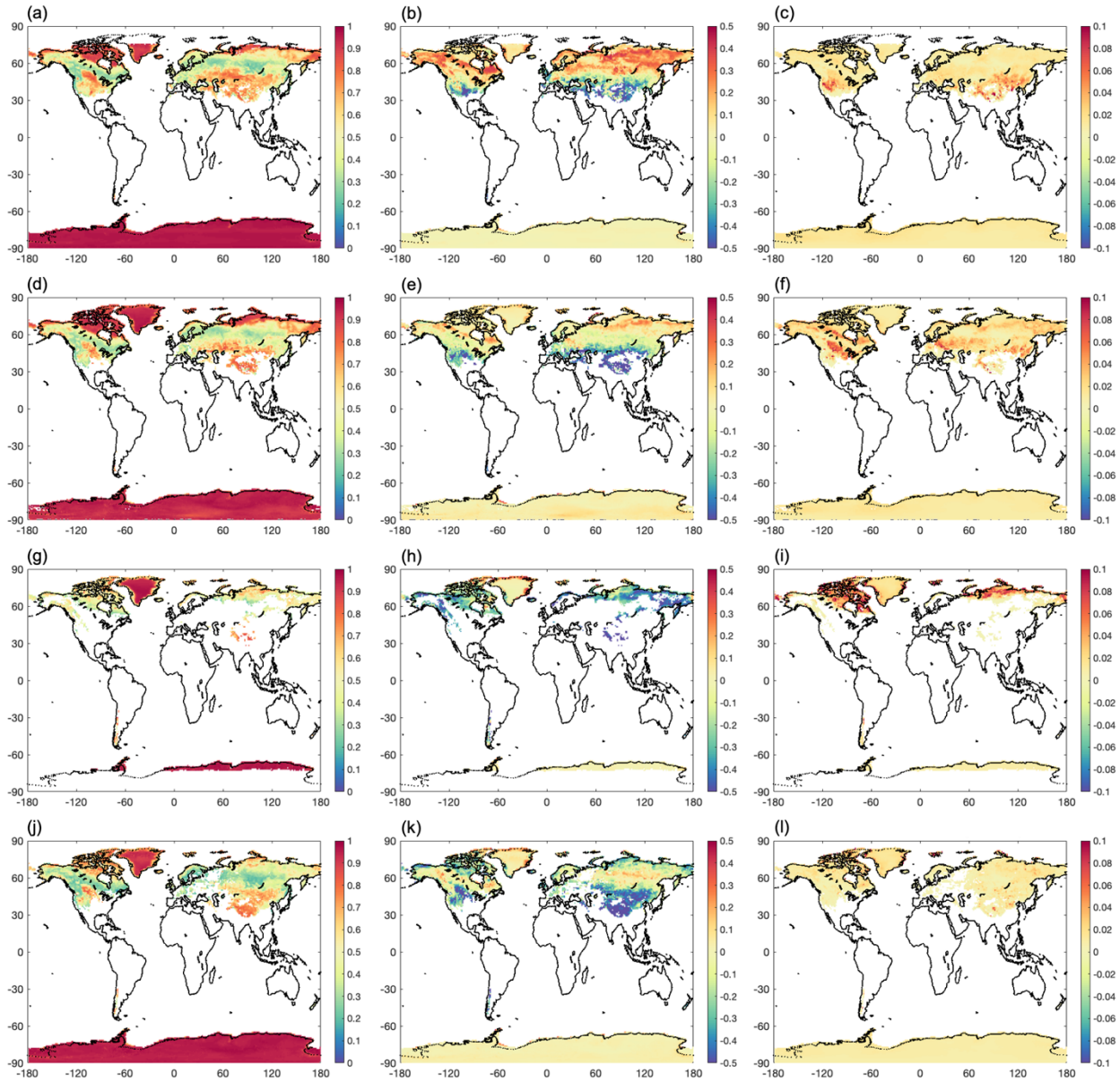

Figure S10. Comparison between MODIS and model simulations of 5-year (2006-2010) seasonal mean white-sky visible surface albedo for 100% snow cover pixels. First column: MODIS observations; second column: default CLM baseline bias; third column: difference between new and default CLM baseline simulations. First row: winter (December-January-February); second row: spring (March-April-May); third row: summer (June-July-August); fourth row: fall (September-October-November).

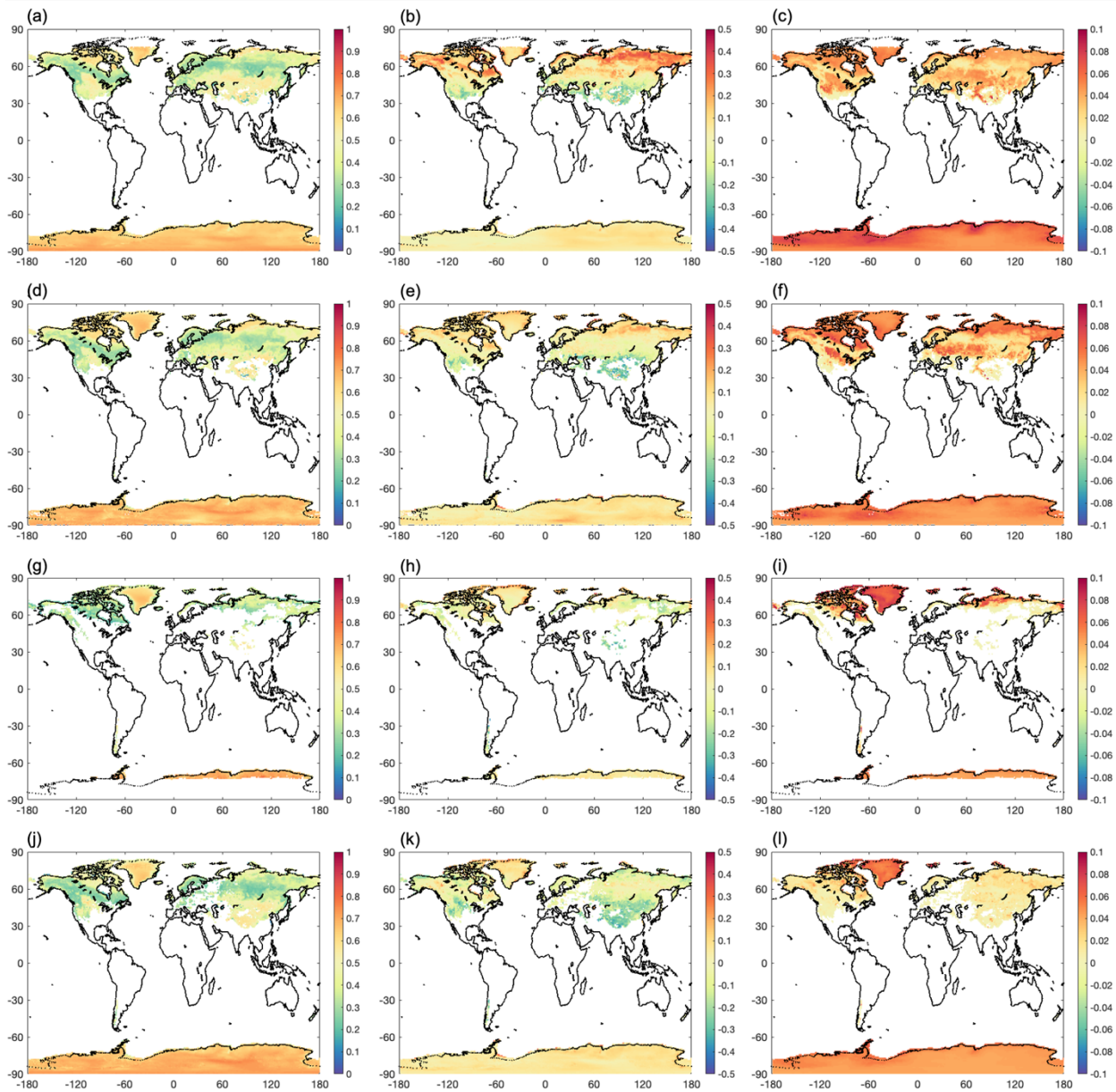

Figure S11. Same as Figure S10, but for the white-sky NIR band.

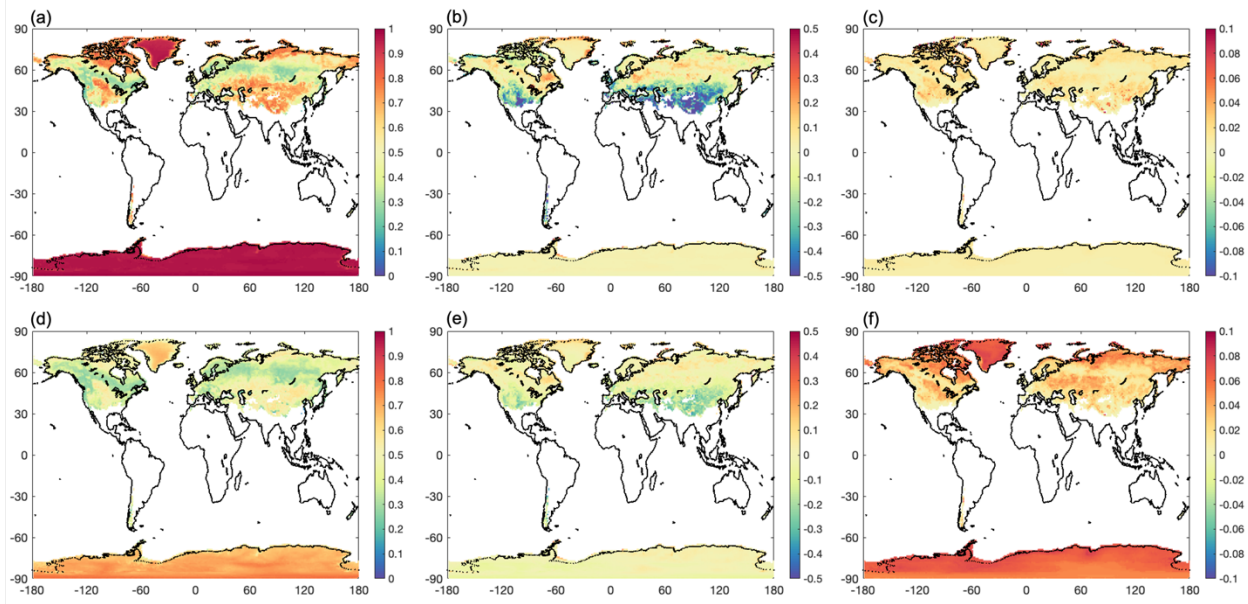

Figure S12. Comparison between MODIS and model simulations of 5-year (2006-2010) annual mean black-sky surface albedo for 100% snow cover pixels. First column (a, d): MODIS observations; second column (b, e): default CLM baseline bias; third column (c, f): difference between new and default CLM baseline simulations. First row (a, b, c): visible band; second row (d, e, f): NIR band.

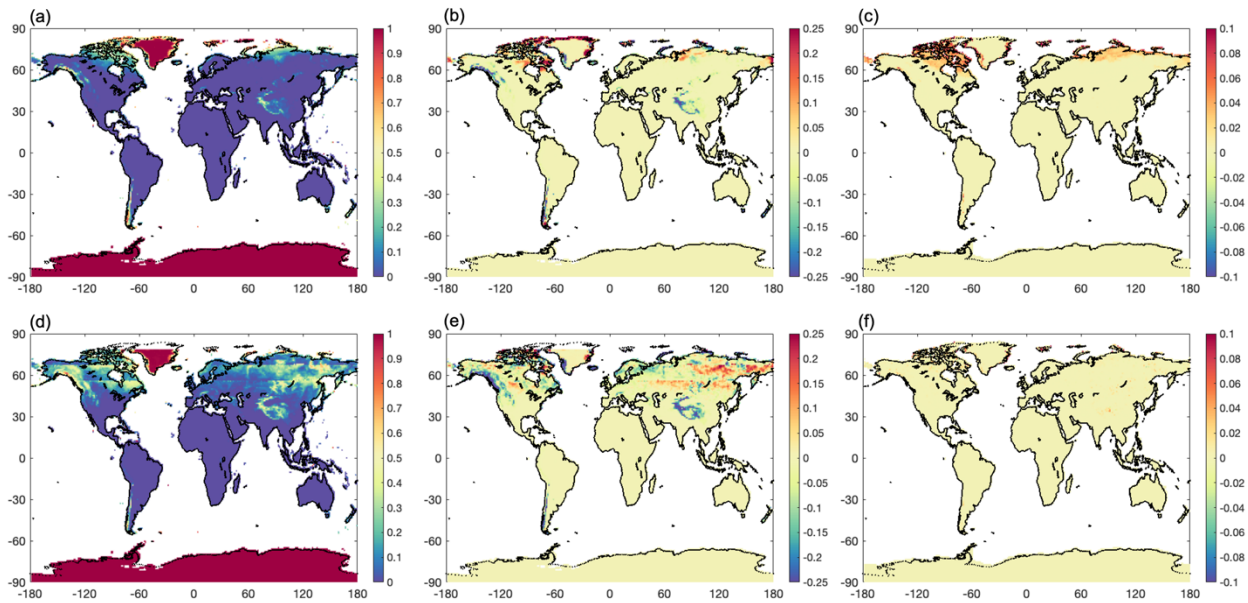

Figure S13. Comparison between MODIS and model simulations of 5-year (2006-2010) seasonal mean snow cover fraction. First column (a, d): MODIS observations; second column (b, e): default CLM baseline bias; third column (c, f): difference between new and default CLM baseline simulations. First row (a, b, c): summer (June-July-August); second row (d, e, f): fall (September-October-November).

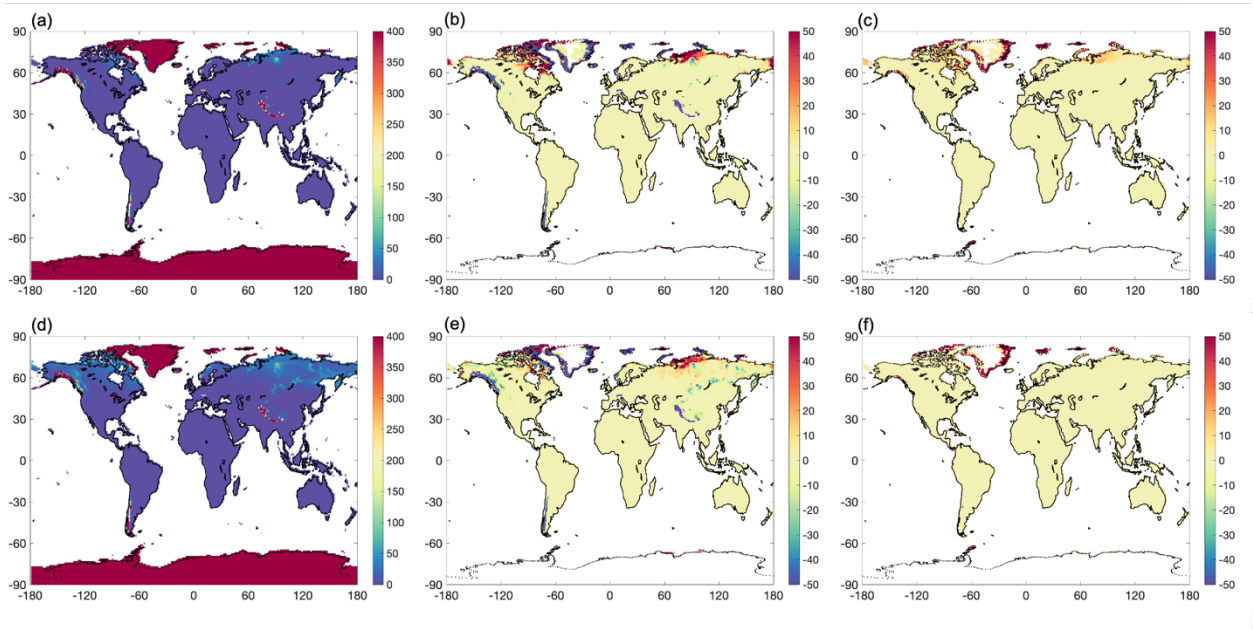

Figure S14. Comparison between ERA-5 and model simulations of 5-year (2006-2010) seasonal mean SWE (mm). First column (a, d): ERA-5 data; second column (b, e): default CLM baseline bias; third column (c, f): difference between new and default CLM baseline simulations. First row (a, b, c): summer (June-July-August); second row (d, e, f): fall (September-October-November).

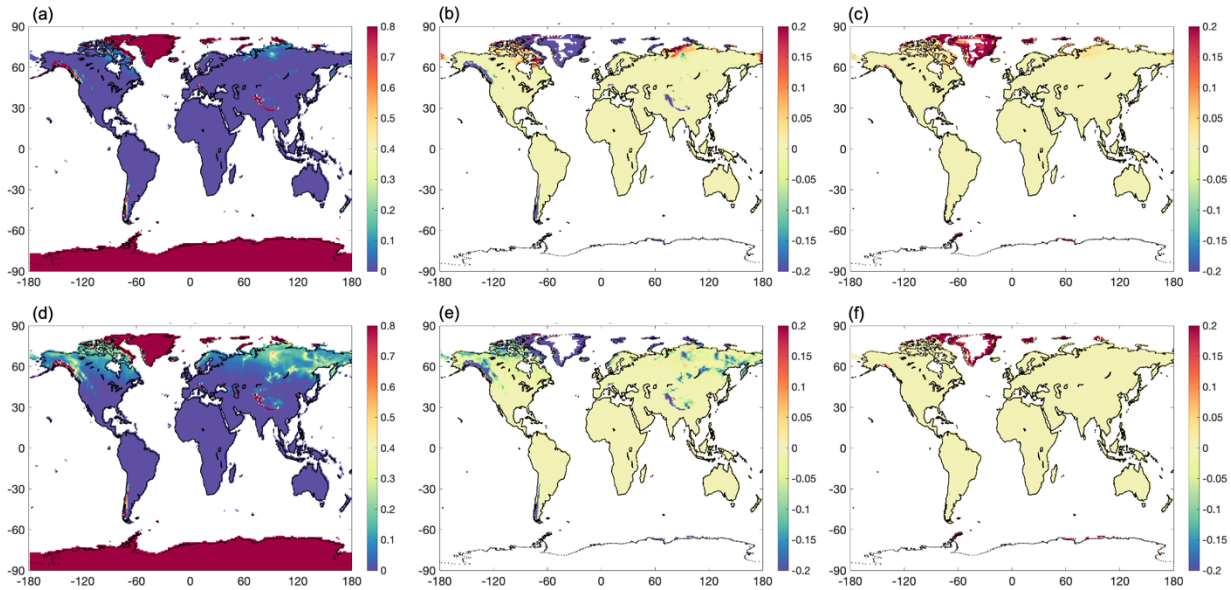

Figure S15. Same as Figure 14, but for snow depth (m) comparison between ERA-5 and model simulations.

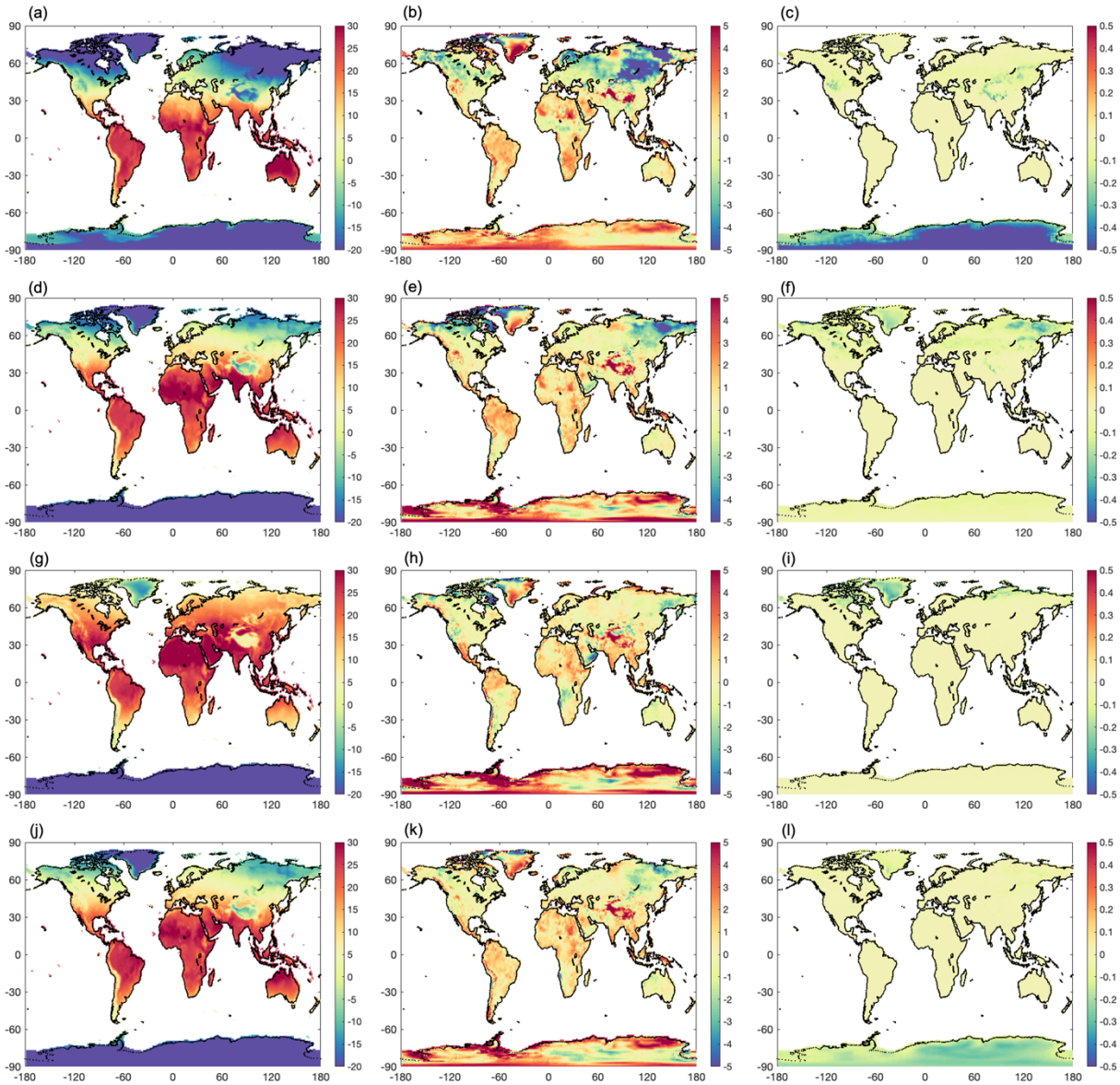

Figure S16. Comparison between ERA-5 and model simulations of 5-year (2006-2010) seasonal mean 2-m surface temperature (°C). First column (a, d, g, j): ERA-5 data; second column (b, e, h, k): default CLM baseline bias; third column (c, f, i, l): difference between new and default CLM baseline simulations. First row (a, b, c): winter (December-January-February); second row (d, e, f): spring (March-April-May); third row (g, h ,i): summer (June-July-August); fourth row (j, k, l): fall (September-October-November).